



**UNIVERSITÀ DELLA  
CALABRIA**

**UNIVERSITA' DELLA CALABRIA**

**Dipartimento di Farmacia e Scienze della Salute e della Nutrizione**

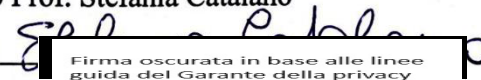
**Dottorato di Ricerca in  
Medicina Traslazionale**

**CICLO  
XXXV**

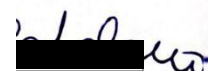
**Breast Tumor Microenvironment and Endocrine Resistance:  
Dissecting the Molecular Link**

**Settore Scientifico Disciplinare MED/05 PATOLOGIA CLINICA**

**Coordinatore:** Ch.mo Prof. Stefania Catalano

Firma  Firma oscurata in base alle linee guida del Garante della privacy

**Supervisore/Tutor:** Ch.mo Prof. Stefania Catalano/Sebastiano Andò

Firma  Firma oscurata in base alle linee guida del Garante della privacy 

**Dottorando:** Dott.ssa Amanda Caruso

Firma:  Firma oscurata in base alle linee guida del Garante della privacy

## Table of contents

<b>1. INTRODUCTION</b>	5
<b>2. MATERIALS AND METHODS</b>	15
Antibodies	15
Cell cultures	15
Lipid droplet visualization	17
Real-Time RT-PCR	18
RNA Library Preparation and Sequencing	19
Conditioned medium systems	19
Trypan-blue Cell Count Assay	20
Soft Agar Growth Assay	20
Boyden-chamber transmigration assays	20
Matrigel-based invasion assays	20
Wound-healing Assay	20
Immunoblot Analysis	21
Proteomic Analysis	21
Functional enrichment analysis	21
MetaCore Functional Analysis	22
MixOmics-MINT tool	22
Survival Kaplan– Meier analysis	23
Thioredoxin activity assay	23

Gene reporter assays	23
Gene overexpressing experiments	23
Metastatic BC fluid specimens	24
Patients derived organoid (PDOs) culture using primary MBC cells	24
PDOs growth assay	24
PDOs viability assay	24
“In vivo” experiments	25
Immunohistochemical Analysis	25
Statistical analysis	26
<b>3. RESULTS</b>	29
Characterization of epithelial MCF-7 CRISPR P and MCF-7 CRISPR Y537S BC cells and stromal normal fibroblasts (NFs) and cancer-associated fibroblasts (CAFs)	29
Impact of MCF-7 YS1 on proliferation, migration and invasiveness of fibroblasts	30
Impact of normal fibroblasts (NFs) and cancer-associated fibroblast (CAFs) on MCF-7 YS1 cell proliferation, migration and invasiveness compared to parental cells	33
Molecular mechanisms involved in ESR1m/tumor microenvironment crosstalk	37
IGF-1R as pontential target to overcome ESR1m/ fibroblasts	41
Impact of 3T3L1 mature adipocyte-derived conditioned medium on growth, motility, and invasion of MCF-7 and MCF-7 Tamoxifen-resistant (TR) breast cancer cells	48
3T3L1 mature adipocyte-derived conditioned medium impacts TXNIP expression and activity	50
TXNIP re-expression reverses 3T3L1A CM-mediated effects in MCF-7 and MCF-7 TR BC cells.	55

Role of IGF1/TXNIP axis in adipocyte-induced Tamoxifen resistance	57
IGF-1/TXNIP axis and adipocyte-induced Tamoxifen resistance in obesity experimental models	59
The involvement of IGF-1/TXNIP axis in AI-resistant BC cells	61
IGF-1/TXNIP axis and Patient-Derived Organoids (PDOs)	63
IGF-1/TXNIP signature and clinical outcomes in BC patients	64
<b>4. DISCUSSION</b>	<b>66</b>
<b>5. CONCLUSIONS</b>	<b>68</b>
<b>6. REFERENCES</b>	<b>69</b>

## 1. Introduction

Breast cancer (BC) represents the fifth leading cause of cancer-associated deaths worldwide, with 685,000 deaths [1]. The latest available data provided by GLOBOCAN 2020 database estimates 2.3 million new BC diagnoses in 2020, with a prospective increased incidence to 3.19 million in 2040. BC is characterized by different subtypes with different morphological and molecular characteristics and different sensitivity to therapy, probability of recurrence and overall survival. Histopathological classification to identify specific subgroups of different tumor types, by including the evaluation of hormone receptors, such as estrogen receptor alpha (ER $\alpha$ ) and progesterone receptor (PR), the epidermal growth factor receptor oncoprotein human 2 (HER2) and Ki-67 proliferation index, may provide prognostic and predictive value and may help to identify new potential therapeutic targets. Indeed, global gene expression profiling studies, according to the St. Gallen Consensus 2011, have allowed to classify BC into the following 4 intrinsic molecular subtypes by hierarchical clustering [2]: i) Luminal A (ER+/PR+/HER2-/lowKi-67), ii) Luminal B (ER+/PR+/HER2-/highKi-67 or ER+/PR+/HER2+/anyKi-67); iii) triple-negative:ER-/PR-/HER2-highKi-67 iv) HER2 positive (ER-/PR-/HER2+).

Luminal A is the most common subtype, accounting for 50-60% of the total breast neoplasia. It is characterized by the expression the ER-related genes that are expressed in the luminal epithelium lining the mammary ducts and it is also characterized by a low expression of cell proliferation-related genes. The immunohistochemical luminal A profile is characterized by ER-positivity (ER+;  $\geq 1\%$ ), high expression of PR, HER2 negativity (HER2-;  $\leq 10\%$ ), along with a low proliferation rate measured by Ki67 ( $<14\%$ ), and a low histological grade [2]. Patients with this cancer subtype have a good prognosis and less lymph node involvement. Furthermore, the relapse rate is lower compared to the other subtypes (27.8%), whereas the median durations of survival with distant metastases is longer (2.2 years) [3,4]. Particularly, these patients display a higher incidence of bone metastases (18.7%) compared to other localizations such as central nervous system, liver and lung which account for less than 10% [5].

Luminal B subtype accounts for 10%-20% of invasive BCs cases. This subtype is characterized by the ER and/or PgR positivity, by the expression or not of HER2 and a higher proliferation rate measured by Ki67. These characteristics confer to this subtype more

aggressive biological and clinical behavior. The relapse rate is different compared to luminal A, whereas although the bone is the major site of recurrence (30%), this subtype displays a high recurrence also in the liver (13.8%). Furthermore, the survival from the time of relapse is lower compared to luminal A (1.6 years) [4]. The overall frequency of luminal B subtype with positivity to HER2 is around 15-20%. The immunohistochemical profile was defined by a high expression of HER2 ( $> 10\%$ ), negativity for ER ( $< 1\%$ ) and PR ( $< 20\%$ ) and high expression of Ki-67 ( $> 20\%$ ). The positivity for HER2 is positively correlated with a higher histological tumor grade and proliferative index, along with high rate of local recurrence (21% vs 8% compared to luminal A phenotype) [6]. Particularly, this subtype has higher incidence to develop brain metastasis [7], along with liver and bone [4]. However, all these studies were obtained before the routine use of adjuvant trastuzumab therapy so its significance in clinical practice needs to be updated.

The immunohistochemical profile of triple-negative tumors, that generally overlap with basal-like, is characterized by negativity for ER ( $< 1\%$ ), PR ( $< 20\%$ ) and the oncoprotein HER2 ( $\leq 10\%$ ) and high Ki-67 ( $> 30\%$ ). However, staining for basal keratins shown to aid selection of true basal-like tumors. These tumors are associated with a higher tumor grade, larger tumor size at diagnosis, high rate of loco recurrence, and high frequency of visceral metastasis (lung, central nervous system, and lymph node) [8].

The immunohistochemical profile of HER2 positive (ER-/PR-/HER2+) is characterized by the ER and/or PgR negativity and HER2 positivity. This subtype is found in approximately 15% of breast cancers. HER2 positive tumors grow faster than those of the type luminal and are often associated with a worse prognosis [9].

Among all the type of BC described, hormone receptor-positive BC carcinoma (Luminal A and Luminal B) accounts for almost 70-80% of all cancer cases [10]. In this case, endocrine therapy is the most effective and widely used therapy in patients with ER+ BC and is the treatment of choice in ER+ metastatic BC. Classical endocrine treatments include (**Figure 1**): i) selective ER modulators (SERMs), such as Tamoxifen, competitive inhibitors of estradiol that bind to the ligand binding sites of ER thus counteracting the estrogen effect, ii) selective ER downregulators (SERDs), such as Fulvestrant, a competitive antagonist whose interaction with ER led to its proteasome-dependent degradation; iii) Aromatase Inhibitors (AIs), letrozole, anastrozole, and exemestane, aiming to reduce estrogen levels by inhibiting the enzyme aromatase [11,12]. In the clinical use, SERMs like Tamoxifen are generally used in

both premenopausal and postmenopausal women, while AIs should only be used in the postmenopausal situation or in premenopausal women after ovarian suppression.

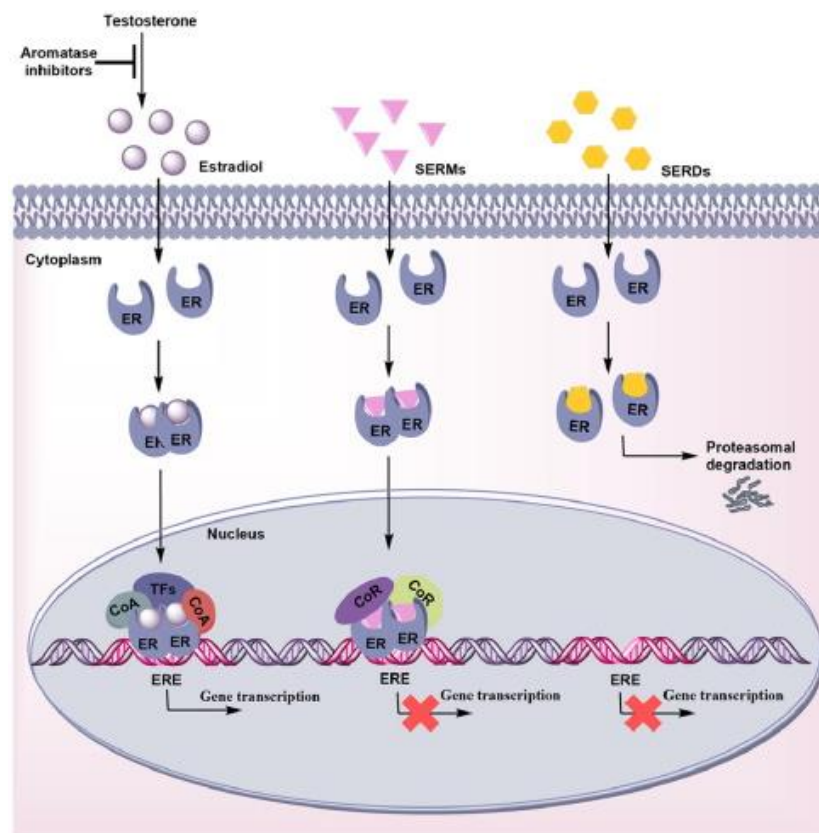


**Figure 1.** Mechanisms of action of AIs, SERMs, and SERDs [13]

The major concern about endocrine therapy is the incoming resistance. Indeed, the typical clinical scenarios of resistance to hormonal therapy are the following.

- 1) 'De novo' resistance in metastatic setting to all endocrine agents or recurrence after the start of adjuvant endocrine therapy;
- 2) 'De novo' resistance to some hormonal therapy;
- 3) Acquired resistance with some periods of response to hormonal therapy until the cancers become resistant to any endocrine treatment.

Particularly, it could be divided in primary or secondary endocrine resistance. Primary endocrine resistance is described as a recurrence that occurs within 2 years from adjuvant endocrine treatment or as tumor progression during the first 6 months of first-line endocrine therapy for advanced or metastatic breast cancer (MBC). Secondary resistance is defined as a recurrence after at least 2 years of hormonal therapy and during/within the first year of completing adjuvant hormonal therapy, or as tumor progression after more than 6 months of

hormonal therapy in advanced BC or MBC [14]. Endocrine resistance occurs through several mechanisms, among whom abnormalities in ER/PgR signalling (e.g. dysregulation of ER expression, co-activators and co-repressor), genomic and epigenomic changes at ESR1 gene, post-translational modification, altered receptor tyrosine kinase pathway, and aberrations in cell cycle regulation [15]. Furthermore, genetic and/or epigenetic aberrations may influence metabolism and responses to therapy. Indeed, several studies have demonstrated that receptor expression may change during tumor progression and approximately 10–20% of the cases may converse from ER+ to ER- BC. Moreover, it has been widely found somatic mutations in *AKT1*, *PI3KCA*, *PTE*, *TP53* and *ESR1* genes giving a genomic instability which generates somatic mutations and leads to clonal expansion [16]. Activating point mutations that clustered in ligand binding domain (LBD) of ESR1 gene harboring mainly at the residues D538G, Y537S, Y537N elicit ligand-independent constitutive activation of ER contributing to resistance to aromatase inhibitors and relative resistance to Tamoxifen and Fulvestrant [17]. ESR1 mutations (ESR1m), which encodes for estrogen receptor (ER), were identified in about 3.3-3.5% of primary tumors and were significantly enriched in 15-55% of metastatic tumors [18]. Zhang et al. were the first group which identified ESR1m in metastatic tumors, such as Y537N, which results in a tyrosine to arginine transition at residue 537, by using PCR and Sanger Sequencing [19]. Subsequently, many researchers have demonstrated the presence of ESR1 mutations in metastatic BC biopsy samples using different DNA sequencing methods (Sanger Sequencing, ddPCR) (reviewed in [20]). Retrospective analysis of the circulating tumor DNA (ctDNA) investigations in prospective clinical trials suggest that ESR1m, mainly detected in metastatic BC, due to the expansion of the resistant mutant clones, particularly after long-term treatment with endocrine therapy was associated with reduced progression-free survival and overall survival (reviewed in [20]). When it has been tried to translate these clinical evidence to the basic research, it was discovered that ESR1 mutations within the ligand binding domain of ER $\alpha$  can promote a ligand-independent tumor growth promotion and therapy resistance [20-24]. Expression of one of the most common mutations, Y537S, which is characterized by changes in protein structure, results in constitutive recruitment of co-activators in the absence of ligand [25], a ligand-independent activation of ER $\alpha$  [26], enhanced crosstalk with insulin growth factor receptor signaling (IGF-1R) [23,27], and enrichment of BC stem cells population (BCSCs) [23]. The conformational change caused by the mutation may lead to a dysregulation of the

phosphorylation-mediated regulatory controls, providing a selective oncogenic advantage during tumor progression, especially during treatment with hormonal therapies, such as Tamoxifen or Fulvestrant [19]. So far, there is a specific treatment guideline for ER+ MBC patients although many preclinical studies have demonstrated that ESR1 mutant cells respond to fulvestrant, but with less sensitivity. However, recent retrospective analyses of the PALOMA-2 clinical trial demonstrated that MBC treated with fulvestrant alone or in combination with palbociclib continued to grow concomitantly with the Y537S ESR1 mutation during treatment [28]. Indeed, the acquisition of these mutations was correlated with a longer time of treatment. These data suggest the expansion of the resistant cellular clones bearing such mutation upon treatment pressure, and not in the early treatment setting.

In addition to cell autonomous signals, it's now clear that phenotypic behavior of malignant cells resistant to endocrine therapy is also dependent on heterotypic signals coming from surrounding stromal cells, such as fibroblasts, macrophages and adipocytes, able to create a wide spectrum of complex and dynamics alterations in host tissue, leading to BC growth and progression (**Figure 2**).

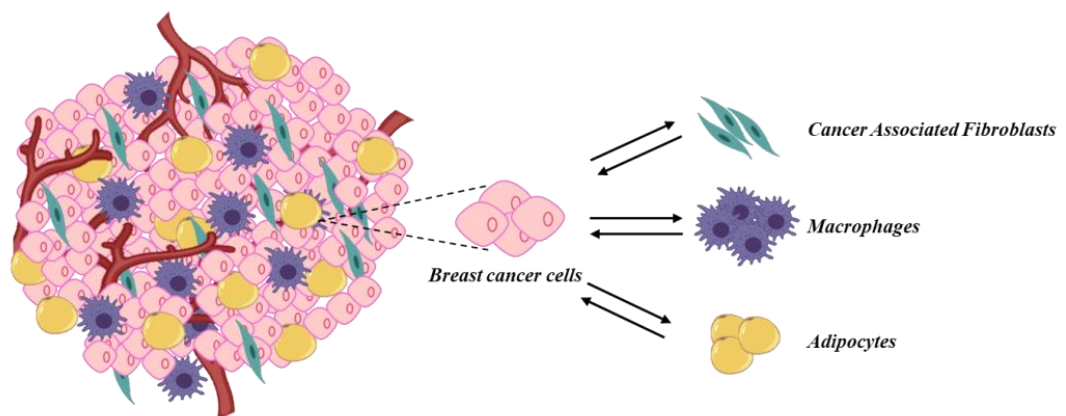


**Figure 2.** Bidirectional crosstalk between BC cells and surrounding microenvironment.

In some cancer types, such as BC, the tumour microenvironment (TME) develops an abundance of fibrous and/or connective tissue. Fibroblast populations found in primary and

metastatic cancers, named as cancer-associated fibroblasts (CAFs), have been widely investigated and are involved in tumorigenesis, tumor progression and metastasis (**Figure 3**) [29-31]. To date, CAFs are well known to be a heterogeneous mesenchymal cell line with diverse putative function, as demonstrated in different studies utilizing single-cell RNA sequencing (scRNA-seq) of several cancers [32-36]. Particularly, four subtype of CAFs have been identified: i) CAF-S1 which display high expression of fibroblast activation protein (FAP) and  $\alpha$ -smooth muscle actin ( $\alpha$ SMA), which contains 8 subclusters of CAFs and are enriched in TNBC; ii) CAF-S2 which display low expression of most detected markers; enriched in luminal A tumours; iii) CAF-S3 which display low expression of  $\alpha$ SMA, and positivity to FSP1 (fibroblast-specific protein 1) and PDGFR $\beta$  (platelet-derived growth factor receptor  $\beta$ ); iv) CAF-S4 which display high expression of  $\alpha$ SMA, integrine b1 (CD29) and low expression of FAP enriched in TNBC. CAFs are the major source of ECM component productions and several secreted factors [37]. CAF secretome can regulate directly or indirectly cancer progression and tumour immunity. For instance, CAF functions can be exerted through growth factors, chemokines and cytokines, such as CC-chemokine 2 (CCL2), CCL5, CXC-chemokine 5 (CXCL5), CXCL9, CXCL10, CXCL12, IGF-1, platelet derived growth factor (PDGF), connective tissue growth factor (CTGF), vascular endothelial growth factor (VEGF), hepatocyte growth factor (HGF), interleukin-1 (IL-1), IL-4, IL-6, IL-8, IL-10, transforming growth factor beta (TGF $\beta$ ) [29,31,38,39]. Interestingly, several studies have demonstrated an immunosuppressive effect of CAF-derived TGF $\beta$ , which may impact the functions of different immune cells, such as T cells, macrophages and neutrophils [40-42]. Interestingly, different studies demonstrated a key role of CAFs in resistance to therapy. Indeed, CAF-secreted factors are involved in protection against Tamoxifen-induced cell death through EGFR (epidermal growth factor receptor) and MMPs (matrix metalloproteinase) upstream of PI3K/AKT [43]. Moreover, a co-culture model of CAFs and BC cells evidenced a higher mitochondrial activity in epithelial cancer cells which drives Tamoxifen resistance [44]. Other molecules contained in the CAF secretome, including IGF-1, HGF, IL-6 have been shown to contribute to a signalling crosstalk between CAFs and BC cells that promote tumour growth and progression (reviewed in [45])

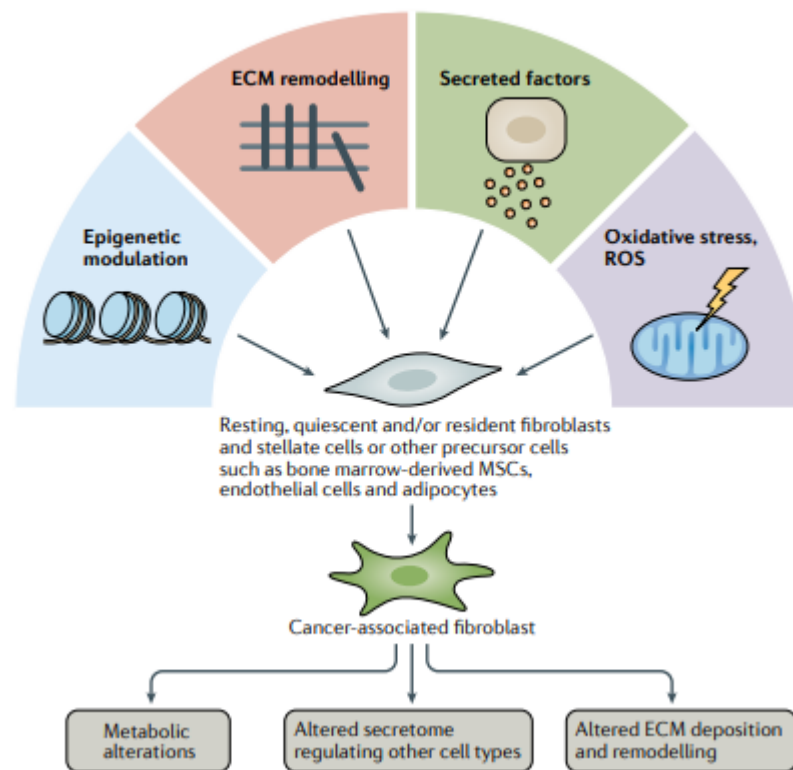


**Figure 3.** Several mechanisms concerning cancer-associated fibroblast (CAF) activation [45]

Another stromal component widely studied is represented by macrophage component, which is well known to be associated with a malignant phenotype and drug resistance in BC [46]. The resulting intratumoral macrophage can be classified into Tumor-associated macrophages (TAMs) with a “M1-like” phenotype or “M2-like” phenotype. M1-like display tumor-killing functions and are stimulated by the T helper cell (Th1) cytokines including interferon- $\gamma$  (IFN- $\gamma$ ) and tumor necrosis factor (TNF) (**Figure 4**). They display antitumor activity by releasing pro-inflammatory cytokines such as TNF IL-1b, IL-6, and IL-8, nitric oxide (NO) and reactive oxygen species (ROS) (reviewed in *Mantovani et al., 2022*). M2-like present protumor characteristics and are stimulated by T helper cell (Th2) cytokines such as IL-4, IL-10 and IL-13 (reviewed in [47,48]). In BC, TAMs may express in the same cells both M1-like and M2-like signature genes [49]. TAM subsets may display pro-angiogenic capabilities via the expression of pro-angiogenic factors and vascular promotion, or promote the pre-metastatic niches formation in BC [50]. Castellaro et al. demonstrated that TAMs induces Tamoxifen resistance in a model of ER+ BC cells [51]. Furthermore, it has been

reported that the CCL2 chemokine, secreted by TAMs, is able to activate the PI3K/Akt/mTOR pathway in BC cells and increase the resistance to Tamoxifen and the recruitment of TAMs, while Tamoxifen-resistant BC cells promote the polarization of TAMs to M2 phenotype, by secreting CCL2 and thus forming a positive feedback loop [52]. Due to the TAMs' role in BC growth and progression, therapeutical strategies aiming to target macrophages have entered clinical evaluation. Indeed, the approach which underwent clinical assessments include targeting recruitment and differentiation of macrophages as well as functional reprogramming by engaging activating or inhibitory (checkpoint) receptors (reviewed in [47]).

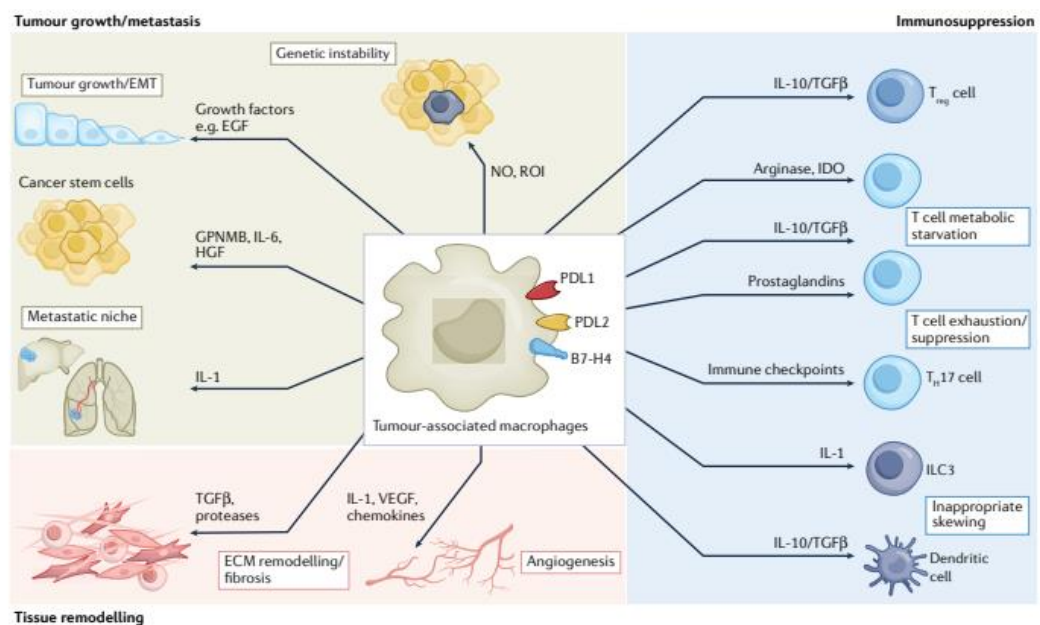


**Figure 4.** Pro-tumoral and immunosuppressive functions of tumor associated macrophages (TAMs) [47].

Finally, adipocyte components, as the most abundant component of TME, have been widely studied as well. Adipocytes are the major components of adipose tissue and play a key role in maintaining the energy balance. Dysfunctional adipose tissue can release excessive cholesterol, fatty acid, triglycerides, hormones, and adipokines which are correlated to metabolic dysfunction, insulin resistance, and worse outcome in cancer treatment [53,54]. Interestingly, it has been demonstrated that adipocytes in co-culture with fibroblasts, can counteract anti-cancer drug effects [55]. Moreover, adipocytes can also recruit other cell types including macrophages, mimicking the immune infiltrates of the tumor [56]. Fat mass and adipose-tissue mass are strongly correlated with obese condition and BC in post-menopausal

women. Different epidemiological evidences reported a tight relationship between obesity and BC, mainly demonstrating that the excess of adiposity profoundly increases the incidence and the mortality of BC patients (reviewed in [57]). The association between obesity and BC is also correlated to the menopausal status, specific life stages and disease subtypes. Particularly, Gershuni et al in 2017, enrolling 848 women divided in three different groups according to their BMI (normal, overweight and obese), demonstrated that overweight and obese status were associated with ER+ and HER2- BC (58.1%) and with more aggressive phenotype such as TNBC (14%); while normal weight women were mainly affected by HER2+ BC [58]. Growing evidence demonstrates that excessive adiposity strongly impacts on incidence, prognosis and progression of breast carcinomas, with relevant implications for clinical management of patients [57,59,60]. High body mass index (BMI) has been associated with larger tumor size, lymph node involvement, metastatic spread, and poorer survival outcomes [61-65]. Various meta-analyses have also indicated a 35-40% increased risk of recurrence or death in obese BC women compared with normal-weight patients [66-68]. Moreover, obesity has been correlated with a reduced response to several therapy such as chemotherapeutic agents and a risk of complications with surgery, radiation and chemotherapy (reviewed in [57]). Furthermore, a study on 19,000 patients with early stage BC, demonstrated that a greater reduced effect of adjuvant treatment with endocrine therapy (Tamoxifen or AIs) occurs in obese women rather than lean ones, independently from tumor size, nodal status, and known prognostic factors, such as hormone receptor expression [69]. Moreover, Wisse et al. reported that in a study of 1,640 patients with primary BC the BMI  $\geq 25$  kg/m<sup>2</sup> was correlated with a worse prognosis in women treated with Tamoxifen or AIs compared to lean patients [70].

From a molecular perspective, adipocytes are progressively taking center stage in explaining the obesity-cancer link. Indeed, important adipocyte-derived mediators (**Figure 5**), such as adipokines, insulin-like growth factors, inflammatory cytokines, and metabolites, which are all abnormally modified in women affected by obesity, may interact with intrinsic molecular characteristics of BC cells. This may result in the activation of several signaling pathways (e.g. MAPK and PI3K/Akt) and transcriptional factors (e.g. NF- $\kappa$ B and HIF-1 $\alpha$ ), thereby boosting BC progression and therapy resistance [57].

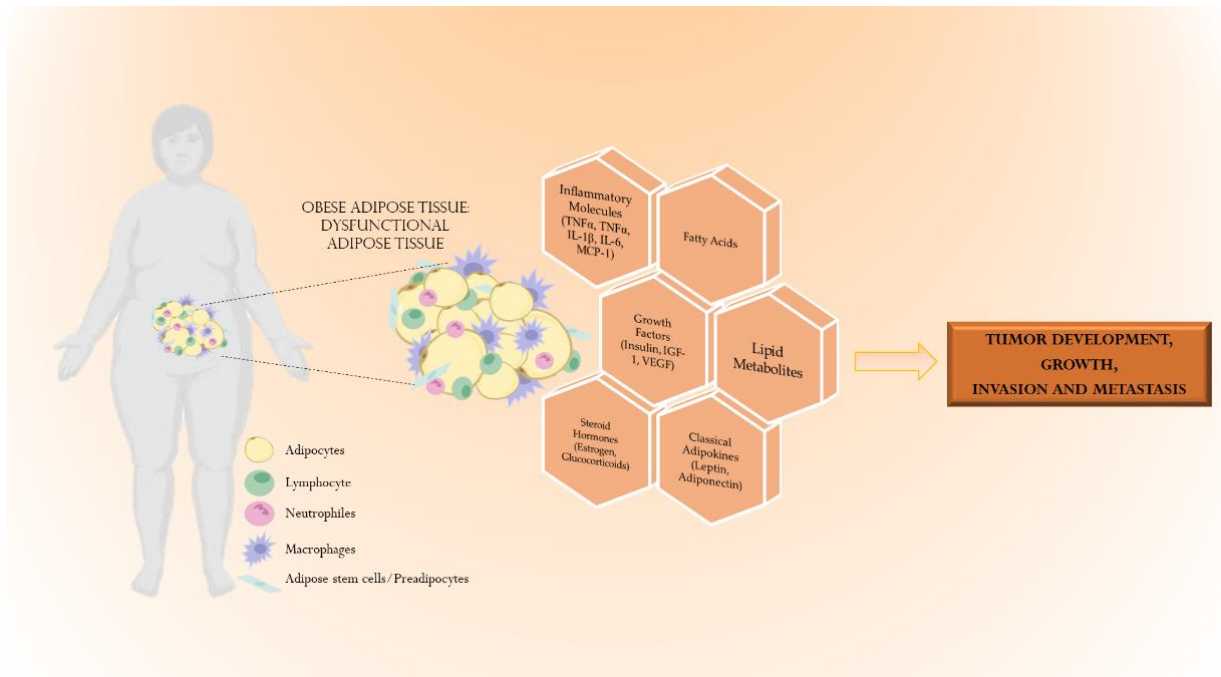


**Figure 5.** Mechanisms underlying the intricate relationship between obesity and cancers

However, despite major advances in understanding these molecular “hits”, the intricate panorama of networks and cascades tying up obesity and BC needs still to be fully elucidated.

On the basis of all these observations, the aims of our study were the following:

- 1) **to investigate the crosstalk between normal fibroblasts (NFs)/cancer-associated fibroblasts (CAFs) and ESR1m BC cells.** First, we explored how fibroblasts impact BC cell phenotype in relation to ESR1 mutation. Then, we evaluated whether ESR1 mutation may conversely reshape fibroblasts phenotype. Finally, the molecular mechanisms underlying this bidirectional crosstalk were investigated.
- 2) **to explore the molecular mechanisms underlying the BC cell/adipocyte crosstalk and Tamoxifen Resistance.** First, we evaluated the effects of adipocyte secretome in influencing Tamoxifen resistant (TR) BC cell phenotype. Then, we unravelled the molecular mechanisms involved in this event. Finally, clinical relevance of our findings was assessed using patient-derived organoids (PDOs) and retrospective survival analysis.

## 2. Materials and Methods

### Antibodies

The following antibodies were used: anti-GAPDH (6C5, sc-47724, Santa Cruz Biotechnology), anti- $\beta$ -actin (sc. 69879, Santa Cruz Biotechnology), anti-TXNIP (D5F3E, #14715S, Cell Signaling Technology), anti-pIGF-1R<sup>Tyr1131</sup> (80732S, cell signaling), anti-pAKT<sup>Ser473</sup> (9271S, Cell Signaling Technology), anti-pMAPK<sup>Thr202/Tyr204</sup> (9101S, Cell Signaling Technology), anti-ITB1 (ab52971, abcam), anti-FSP1 (ab53066, abcam), anti- $\alpha$ SMA (19245, Cell Signaling Technology).

### Cell Cultures

Human MCF-7 BC cell lines, murine 3T3-L1 pre-adipocytes were purchased from American Type Culture-Collection (Manassas, VA, USA) and cultured following supplier instruction. Human MCF-7 Tamoxifen resistance (TR) BC cell line was generated by treating human MCF-7 with Tamoxifen 1  $\mu$ M for more than six months [71]. Human MCF-7 Aro BC cell line stably expressing the aromatase enzyme was generated by treating human MCF-7 Aro with anastrozole 1  $\mu$ M for more than one year [72]. Human MCF-7 anastrozole-resistant (AnaR) BC cell line derived from MCF-7 Aro cells and were treated with anastrozole 1  $\mu$ M for more than one year. Long-term estrogen deprived (LTED) BC cell line was generated by depriving MCF-7 cells of estrogen for six months. Human MCF-7 Y537S BC cell lines were generated by using CRISPR-CAS9 knock-in in collaboration with Prof. Fuqua's lab as described [73]. 3T3L1-A mature adipocytes were obtained by culturing 3T3-L1 cells in pre-adipocyte growth medium for 72 h and then in differentiation medium which contains 1  $\mu$ g/ml bovine insulin (Sigma-Aldrich), 0,5 mM 3-Isobutyl-1-Methylxanthine (Sigma-Aldrich) and 1  $\mu$ M Dexamethasone (Sigma-Aldrich) for 48 h. Subsequently, adipocytes were maintained in growth medium with 10% FBS and 1  $\mu$ g/ml bovine insulin for 14 days. 3T3L1-A obese adipocytes were obtained by incubating fully differentiated adipocytes 3T3L1-A in mature adipocyte growth medium supplemented with 1 mM of a 1:2:1 palmitate (C16:0), oleate (C18:1), and linoleate (C18:2) (Sigma Aldrich, Castle Hill, NSW, Australia) for 24 h. Cancer associated fibroblasts (CAFs) were obtained as described (*Catalano et al., 2019*). Normal Fibroblasts (NFs) were supplied by Professor Michael Lisanti from the University of Salford, Manchester, UK. All cell lines used were cultured in the growth medium as described in

table 1. Cells were frozen following manufacturer's recommendations and used and authenticated by short tandem repeat analysis (AmpFLSTR Profiler Plus PCR Amplification Kit, Applied Biosystems, MB, Italy) at our Sequencing Core within 4 months after frozen aliquots recovery, and systematically tested for mycoplasma-negativity (MycoAlert, Lonza, Basilea, Switzerland).

**Table 1.** Cell lines and relative growth medium

Cell lines	Growth medium
MCF-7	DMEM:F12 (Gibco) 5% FBS (Sigma Aldrich) 1% L-glutamine (Sigma Aldrich) 1 mg/ml penicillin-streptomycin (Sigma Aldrich)
MCF-7 TR	DMEM:F12 10% FBS 1% L-glutamine 1 mg/ml penicillin-streptomycin 1 $\mu$ M Tamoxifen
MCF-7 Aro	MEM 10% FBS 1% L-glutamine 1% Eagle's nonessential amino acids 1 mg/mL penicillin/streptomycin zeocin 0.2 mg/mL
MCF-7 AnaR	MEM 10% FBS 1% L-glutamine 1% Eagle's nonessential amino acids 1 mg/mL penicillin/streptomycin zeocin 0.2 mg/mL anastrozole 1 $\mu$ M
LTED	DMEM 10% Dextran-Coated Charcoal (Sigma-Aldrich, Milano, Italy) 1% L-glutamine 1 mg/mL penicillin/streptomycin
MCF-7 P	MEM 10% FBS

	1% L-glutamine 1% Eagle's nonessential amino acids 1 mg/mL penicillin/streptomycin
MCF-7 YS1	MEM 10% FBS 1% L-glutamine 1% Eagle's nonessential amino acids 1 mg/mL penicillin/streptomycin
3T3L1	DMEM (ATCC, Manassas, Virginia, USA) 10% BCS 1 mg/ml penicillin-streptomycin
3T3L1A	DMEM (ATCC, Manassas, Virginia, USA) 10% FBS 1 mg/ml penicillin-streptomycin 1 µg/ml bovin insuline
3T3L1A obese	DMEM (ATCC, Manassas, Virginia, USA) 10% FBS 1 mg/ml penicillin-streptomycin 1 µg/ml bovin insuline
NFs	DMEM 10% FBS 1% L-glutamine 1 mg/ml penicillin-streptomycin
CAFs	DMEM:F12 and F12 1:1 15% FBS 1 mg/ml penicillin-streptomycin

### Lipid droplet visualization

Lipid droplets in adipocytes were detected by using Oil Red O. Adipocytes were fixed with 2% (v/v) formaldehyde for 30 min at 37 °C, 5% CO<sub>2</sub>. Then, the formaldehyde was discarded and the cells were washed with PBS two times and subsequently, the plates were air dried. The cells were incubated with Oil Red O solution (three parts of 0.5% Oil-Red O (w/v) in 60% isopropyl alcohol and two parts water) for 30 minutes. Thereafter, Oil Red O staining solution was withdrawn and the cells were rinsed with water and air-dried. Images of the stained lipid droplet were acquired by using Olympus microscope (Olympus, Tokyo, Japan). Aiming to measure the lipid content, the dye was extracted from the stained adipocytes by

using 60% isopropanol and then quantified by measuring the absorbance at 405 nm. Lipid content was shown as a fold, in comparison with the pre-adipocytes as 1-fold lipid formation.

### Real-Time RT-PCR

Total RNA from cells was extracted by using the TRIzol reagent (Thermo Fisher Scientific, Waltham, MA, USA). NanoDrop-1000 spectrophotometer was used to evaluate RNA quality, integrity, and concentration. Two micrograms of total RNA were reverse transcribed with the RETROscript Kit (Applied Biosystems, Monza, Italy) and gene expression was analyzed by real-time RT-PCR using SYBR Green Universal PCR Master Mix (Bio-Rad, Hercules, CA, USA) in an iCycler iQ Detection System (Bio-Rad). The relative gene expression levels were assessed and calculated as previously described [74]. Each sample was normalized on 18S mRNA expression. Primers are listed in Supplementary Table 2.

**Table 2.** Oligonucleotide primers used in this study

Gene symbol	Gene name	Primer Sequences
<b>TXNIP</b>	Thioredoxin Interacting Protein	For 5'-AAGACCAGCCAACAGGTGAG-3' Rev 5'-AGGAAGCTAAAGCCGAACT-3'
<b>IGF-1R</b>	Insulin Like Growth Factor 1 Receptor	For 5'-TGTCCAGGCCAAAACAGGAT-3' Rev 5'-CATTCCCCAGCCTGCTGTTA-3'
<b>PPAR<math>\gamma</math></b>	Peroxisome Proliferator-Activated Receptor gamma	For 5'-GAGTTCATGCTTGTCAAGGATGC- 3' Rev 5'-CGATATCACTGGAGATCTCGCC-3
<b>Ob</b>	Leptin	For 5'-ACTTCATTCTGGGCTTAC-3' Rev 5'-GATTCTCCAGGTCATTGGCT-3'
<b>AdipoQ</b>	Adiponectin	For 5'-TGACGACACCAAAGGGCTC-3' Rev 5'-CACAAGTTCCTTGGGTGGA-3'
<b>MMP9</b>	Matrix Metalloproteinase 9	For 5'-AAGGCAGCGTTAGCCAGAA-3' Rev 5'-GCGGTACAAGTATGCCTCT-3'
<b>FABP4</b>	Fatty Acid Binding Protein 4	For 5'-ATGTGTGATGCCTTTGT-3' Rev 5'-TTCCATCCCACTTCTG-3'
<b>FSP1</b>	Fibroblast-Specific Protein-1	For 5'-TCTTGGTCTGGTCTCAACGG-3' Rev 5'-TGTCACCCTCTTGCCTGAG-3'
<b>ACTA-2</b>	Alpha 2 Smooth Muscle	For 5'-AGCCATCTTTCATTGGGAT-3' Rev 5'-CATGGTGGTACCCCCTGACA-3'
<b>CD29</b>	Integrin beta 1	For 5'-

		AATGAATGCCAAATGGGACACGGG-3' Rev 5'-TTCAGTGTGTGGGATTTGCACGG-3'
18S	18s rRNA	For 5'-CCCACTCCTCCACCTTTGAC-3' Rev 5'-TGTTGCTGTAGCCAAATTCGTT-3'

### RNA Library Preparation and Sequencing

After RNA extraction, the quality was assessed with Agilent TapeStation4200 (Agilent, CA, USA). High quality RNA from three-independent purifications for each experimental point was used for library preparation. Indexed libraries were prepared from 1µg/ea of purified RNA with TruSeq Stranded mRNA Library Prep (Illumina, CA, USA) following suppliers. Libraries were quantified using the TapeStation 4200 and Qubit fluorometer (Thermo Fisher), then pooled such that each index-tagged sample was present in equimolar amounts. The pooled samples were subject to cluster generation and sequencing using an Illumina NovaSeq6000 (Illumina) in a 2x75 paired-end format. RNA sequencing data have been deposited in the EBI ArrayExpress database (<http://www.ebi.ac.uk/arrayexpress>) with Accession Number GSE223853.

### Conditioned Medium Systems

To produce conditioned medium (CM) from mature adipocytes (3T3L1A) or obese mature adipocytes (3T3L1A ob) cells were incubated in a culture medium of DMEM-F-12 containing 3% Charcoal-stripped Fetal Bovine Serum (CS, Sigma-Aldrich), 100 mg/mL of L-glutamate (Sigma Aldrich), and 1% pen/strep (Sigma Aldrich) for 36-48 h. Normal fibroblasts (NFs) cells were incubated in DMEM, 3% Charcoal-stripped Fetal Bovine Serum (CS, Gibco), 1 mg/ml penicillin-streptomycin, 1% L-glutamine for 24h. Cancer associated fibroblasts (CAFs) cells were incubated in DMEM:F12, 3% Charcoal-stripped Fetal Bovine Serum (CS, Sigma-Aldrich), 1 mg/ml penicillin streptomycin for 24 h. MCF-7 and MCF-7 YS1 were incubated in MEM 10% CS, 1% L-glutamine, 1% Eagle's nonessential amino acids, 1 mg/mL penicillin/streptomycin for 24h. Then, CM was collected, centrifuged to remove cellular debris, and used in respective experiments.

### Trypan-blue Cell Count Assay

Cells were seeded at a confluence of 50,000 cells/well in 24 well plates and treated for 48 h as indicated. Cells were harvested by trypsinization and incubated in a 0.5% trypan blue solution, for 10 min at room temperature. Trypan blue negative cells were counted through a Countess® II Automated Cell Counter (Thermo Fisher) at day 0 and after 48h of treatment.

### **Soft Agar Growth Assay**

Cells (20,000 cells/well) were plated in 2 ml of 0,35 % agarose in charcoal-stripped, on top of 1 % of agarose base layer in 12-well plates. One day after plating, media containing vehicle or treatments as indicated were added to the top layer, and replaced every two days. After 14 days colonies 50  $\mu$ m in diameter were counted. Each condition was performed at least in triplicate.

### **Boyden-chamber transmigration Assay**

Cells were seeded at a confluence of 20,000 cells/well in the upper compartments of Boyden Chamber (8  $\mu$ m membranes, Corning Costar, Corning, NY, USA) and regular growth medium was used in the lower chambers. After 5-24 h, migrated cells were DAPI-stained, images were acquired by Olympus microscope (Olympus, Tokyo, Japan) and quantified by Image J software (NIH, MI, USA).

### **Matrigel-based invasion Assay**

The matrigel-based invasion assay was performed in chambers (8  $\mu$ m-membranes, Corning Costar) coated with Matrigel (BD Biosciences, 2 mg/mL) in 24-well plates. Cells were seeded (20.000 cells/well) into top transwell-chambers and regular growth medium was used in the lower chambers. After 5-24 h, invaded cells were DAPI-stained, images were acquired by Olympus microscope (Olympus, Tokyo, Japan) and quantified by Image J software.

### **Wound-healing assay**

Cells were seeded in 6-well plates and grown to complete or near 100% confluence. Subsequently, the resultant cell monolayers were scraped with a sterile pipet tip and exposed to the different experimental conditions. Wound closure was monitored over 12-24h hours and then fixed and stained with Coomassie Brilliant Blue. Pictures represent one of three independent experiments.

### **Immunoblot Analysis**

Cells were lysed in RIPA Buffer supplemented with protease inhibitors as previously described [75]. Equal quantities of protein were resolved by SDS-PAGE and transferred to nitrocellulose membranes by using trans-blot turbo transfer system (Bio-Rad). Nitrocellulose membranes were blocked with 5% milk in TBST, followed by incubation with primary and fluorescence-labeled secondary antibodies. Odyssey FC and Image Studio Lite software (Licor, Lincoln, NE, USA) were employed to, respectively, acquire and quantify the band of interest.

### **Proteomic Analysis**

Cell pellets were dissolved in 4% SDS buffer containing 100 mM Tris pH 8.0 and were sonicated for three times. Then, proteins were reduced with the addition of 10  $\mu$ L of DTT 500 mM and denatured at 95 °C for 10 min and completed by using the Filter-Aided Sample Preparation (FASP) method using the filter membrane Microcon (10 kDa, Millipore, MA, USA). 60  $\mu$ L of 50 mM TEAB buffer and 200 ng of trypsin “proteomics grade” (Merk Life Science, MI, Italy) were added to each sample for digestion at 37 °C overnight. The next day, 140  $\mu$ L of H<sub>2</sub>O was added and the samples were centrifuged at 14,000g for 20 min to collect 200  $\mu$ L of digest.  $\mu$ L of each sample were then purified by StageTip SCX. The digested samples were acidified by adding 80% acetonitrile-0.5% formic acid (Wash B, 200  $\mu$ L) and loaded into pipette tip with a layer of SCX resin (Millipore extraction disks) previously conditioned with Wash A (0.5% FA and 20% ACN). After two washes with Wash B and A peptides have been eluted with 10  $\mu$ L of 500 mM ammonium acetate (AA) and 20% of ACN. All peptide fractions were fully dried and reconstituted in 10  $\mu$ L of 2% ACN/0.1% FA (v/v). One  $\mu$ L of purified digest have been used for Nano Liquid Chromatography-Tandem Mass Spectrometry (Nano-LC-MS/MS). Finally, samples were examined by performing an LC-MS/MS system consisting of an EASY-LC-1000 chromatograph and a Q-Exactive mass spectrometer (Thermo Fisher) and analyzed by performing data-dependent acquisition. Raw MS data were analyzed using MaxQuant software using the Andromeda search engine. The MS/MS spectra were searched against a Homo sapiens reference proteome. Perseus software was used for statistical analysis of MaxQuant. Finally, for all the data sets, two-sample t test was used to assess statistical significance of protein abundances.

### **Functional enrichment analysis**

De-regulated proteins identified in MCF-7 cells were subjected to Gene Ontology (GO) and biological pathway enrichment analysis using FunRich tool (<http://www.funrich.org>) against human FunRich background database. A  $p$ -value  $< 0.05$  was regarded as statistically significant and the GO results were ranked by  $p$ -value. The top ten significant pathways in the de-regulated proteins were exhibited as bar charts.

### **MetaCore Functional Analysis**

The differentially expressed transcriptome and protein datasets were functionally processed by applying the MetaCore™ integrated software suite for functional analysis of experimental data (Clarivate Analytics, London). Differentially expressed genes or proteins were also investigated via the MetaCore Network Building tool and by applying the direct interaction algorithm. This functionally crosslinks gene transcripts under processing by building networks of corresponding proteins (and non-coding RNA) that directly interact with each other, according to the manually curated MetaCore in-house database of physiological and pathological protein–protein and protein–nucleic acid interactions, signaling and metabolic pathways, from scientific literature. Resulting direct interaction networks (DIN) represent the interactomic core of the investigated process and are prioritized according to their statistical significance. Nets are then graphically visualized as nodes (proteins) and edges (interconnections among proteins) and named in relation to their five most significant factors, i.e. central hubs. Since they establish the highest number of interactions with the other components of the net, central hubs acquire crucial roles in defining the biochemical and molecular properties of the investigated systems. In fact, they are usually recognised as highly significant biomarkers for understanding the physiological and pathological studied states as well as for drug design and pharmacological attempts, as we previously widely proved [76-79].

### **MixOmics-MINT tool**

All the common (~17400) genes between the MCF-7 and MCF-7 TR Datasets were analysed by MixOmics-MINT tool on R environment (Version 6.22.0, Le Cao KA et al., 2016), a multivariate integrative approach to identify reproducible signatures of conditioned medium across the two experiments. The appropriate number of components and variables was optimized by a preliminary model according the Balance Error Rate of misclassification.

Through Sparse Partial Least Squares - Discriminant Analysis (sPLS-DA) the samples were finally supervised classified and the common variables between the two datasets were selected according their contribution discriminating between conditioned and control media. The selected genes of the model were represented by heatmap of correlation clustering distances and tree- clusterized according Ward's method.

### **Survival Kaplan– Meier analysis**

Kaplan-Meier plots were generated using the Kaplan-Meier plotter online tool (<https://kmplot.com/analysis/>) by using patient datasets. Kaplan–Meier survival graph, hazard ratio (HR) with 95% confidence intervals (CI) and log-rank p-value were calculated and plotted in R using Bio-conductor packages as indicated [80].

### **Thioredoxin activity assay**

Thioredoxin (TRX) activity assay was performed by using the Thioredoxin Reductase Assay Kit #CS0170 (Sigma-Aldrich) and following the manufacturer's recommendations.

### **Gene reporter assays**

Cells were plated in regular growth medium into 24 well plates and transfected as described (Panza et al., 2021). After 12h, treatments were added as indicated, and cells were incubated for 24h. Luciferase activity was detected using the Dual Luciferase Kit (Promega, Milan, Italy) in accordance to the manufacturer's instruction. The activity of firefly luciferase was normalized to Renilla luciferase activity, which represents internal transfection control.

### **Gene overexpressing assay**

MCF-7 TXNIP-overexpressing cells were generated by stable transfection using the lentiviral approach. The cells have been transfected according to the Origen protocol, with the lentiviral vector overexpressing TXNIP (RC210804L3V) containing an expression tag (c-myc-DDK) which will allow us to visualize the expression of the ORF as a c-myc-DDK-tagged protein; or with the empty vector (PS100092V). All vectors contain the resistance gene Puromycin, whereby, in order to select the cells that have been successfully transfected, stable clones are selected by adding Puromycin 2 µg/ml.

**Metastatic BC fluid specimens**

Metastatic BC fluid specimens derived from pleural effusions and ascites fluid were collected from MBC patients, who underwent drains for their palliative care. Fluid specimens were collected via the Manchester Cancer Research Centre Biobank (Ethical Approval Study Ref: 05-Q1402-25 and 12-ROCL-01) prior patients' informed consent. To collect BC metastatic cells, ascites or pleural effusions were centrifuged for 10 mins at 1000g and then resuspended in PBS. If there is any red blood cell contamination, red blood cell lysis buffer (ACK lysis buffer) was used to remove them. The cells were then plated for organoids or frozen.

**Organoid culture using primary MBC cells**

BC cells derived from metastatic fluid samples were plated in a 24-well plate by resuspending them in Matrigel (Corning). The matrigel was set in the wells for 30 minutes at 37°C in the form of domes. Organoids were cultured at 37°C in 5% CO<sub>2</sub> using the BC organoid media containing DMEM F-12, 1% pen/strep, 10 µg/mL insulin, 1 µg/mL hydrocortisone, 10 ng/mL epidermal growth factor (EGF) and 10 µM ROCK inhibitor Y-27632. The media was changed every 3 days and made fresh every 10 days. To passages the organoids, the matrigel was mechanically disaggregated and centrifuged at 500g for 10 minutes. The bottom was then resuspended in Dispase for 1h at 37°C. Then, the organoids were centrifuged for 10 minutes at 500g and resuspended in 500ul of Accutase and incubated for 5 minutes at 37°C to degrade cellular junctions of the organoids. Finally, organoids were washed in PBS and centrifuged for 10 minutes at 500g and then resuspended in matrigel at lower density than the previous passage.

**Patients derived organoid (PDOs) growth assay**

Organoids derived from metastatic patient samples were plated at 50,000 cells per well in 50µl of Matrigel (Corning) on 24-well plate and then cultured in corresponding growth medium and treated with different conditions. Organoid growth was measured after 10 days using an EVOS XL CORE (Thermo Fisher). The measurements were made by averaging the count of the number of organoids per 100x microscope field. Three fields were counted around the edge of the matrix dome.

**Patients derived organoids (PDOs) viability assay**

Organoids derived from metastatic patient samples were plated at 4,000 cells per well in 10 $\mu$ L of Matrigel on 96-well plates and then cultured in growth media. Growth media was refreshed every 3 days. After 9 days, CellTiter-Glo<sup>®</sup> 3D Cell Viability Assay (Promega) was used to measure the cell viability. 30 minutes before the start of the assay the plates were cooled at room temperature for 30 minutes and then 3D Cell Titre Glo substrate was added to each well. The plates were shaken vigorously for 5 minutes and then incubated at room temperature for other 25 minutes. The luminescence was measured by using the Varioskan Lux (Thermo Fisher) for 1000ms per well.

### **In vivo experiments**

The 'in vivo' experiments were performed in 5-6-week-old female athymic nude mice (HsdCpb:NMRI-Foxn1nu; ENVIGO RMS, Udine, Italy) maintained in a 12 h LD (L–light; D–dark) cycle and at constant temperature. MCF-7 P and MCF-7 Y537S (5.0  $\times$  10<sup>6</sup> cells per mouse) and in combination with CAFs (ratio 3:1 tumor cells/CAFs) were resuspended in 100  $\mu$ L and injected subcutaneously in 100  $\mu$ L of Matrigel (Corning Costar) of each mouse (n = 5 for group). When the mean tumor size reached an average volume of 100-150 mm<sup>3</sup>, the mice were randomly divided, and the treatments with 30 mg/kg/day GSK1838705A were started and delivered orally. Tumor length and width were measured by caliper measurements one time per week and the volume was calculated conforming to the following formula:  $V = (\text{length} \times \text{width}^2)/2$ . At the end of the experiment, animals were euthanized and sacrificed and tumors xenografts were dissected, fixed in 4% formalin or frozen in nitrogen, and stored at -80 °C for further analyses. All experiments involving animals and their care were approved by the Ministry of Health (protocol No 533/2019-PR) and were in accordance with the ethics committee of the University of Calabria, Italy.

### **Immunohistochemical Analysis**

Paraffin-embedded tumor masses of 5  $\mu$ m of thicknesses were mounted on poly-lysine slides, were deparaffinized and dehydrated with decreasing steps of ethanol. Immunohistochemical experiments were performed after heat-mediated antigen retrieval in Citrate Buffer, using Ki-67 (Agilent Dako, clone MIB-1, M7240), Cytocheratin 18 (Agilent Dako, clone DC 10, M7010) and  $\alpha$ -SMA (Agilent Dako, clone 1A4, M0851) primary antibodies in MCF-7 WT and Y537S, with and without the presence of CAFs, with and without GSK1838705A treatment samples, at 4°C overnight. Sections were incubated with a

biotinylated secondary antibody for 1h at room temperature, followed by the avidin biotin horseradish peroxidase complex (Vectastain ABC Kit, Vector Laboratories, Inc). Immunoreactivity was visualized using the diaminobenzidine chromogen (DAB Substrate Kit, Peroxidase, Vector Laboratories, Inc). Haematoxylin (Sigma-Aldrich) staining was performed to bring out the unstained nuclei. The specificity of the primary antibodies was verified by using normal serum in negative control sections. Slides of tumor samples were visualized using Aperio LV1 and images have been acquired with Image Scope.

### **Statistical Analysis**

Data were analysed for statistical significance using two-tailed Student's t test, performed by GraphPad-Prism7 software program (GraphPad Inc., San Diego, CA, USA). P values less than 0.05 were considered significant. All data are shown as mean  $\pm$  standard deviations (SD) or standard error meaning (SEM). For RNA sequencing bioinformatics analysis, Fastq underwent to Quality Control using FastQC tool (<http://www.bioinformatics.babraham.ac.uk/projects/fastqc/>). The tool cutadapt (version 2.5) was used to remove the adapter sequence and the very short reads (reads length < 20). The mapping of paired-end reads was performed using STAR (version 2.7.5c) with the standard parameters for paired reads, on reference genome assembly hg38 obtained from GenCode (Release 37 (GRCh38.p13)). The quantification of transcripts expressed for each sample was performed using FeatureCount (version 2.0) [81] algorithm. DESeq2 [82] was used to perform the normalization matrix and differentially expressed gene of all samples considered. For transcriptome values of genes, the genes presenting a BH-FDR  $\leq$  0.01 and an absolute log<sub>2</sub>FC higher than 2 respectively were selected for further functional analyses and heatmap images. In particular, DEGs were clustered according to Ward's method of the scaled Euclidean distances in the heatmap.



AIM 1:

**to investigate the crosstalk between normal fibroblasts  
(NFs)/cancer-associated fibroblasts (CAFs) and ESR1m BC  
cells**

## Results

### Characterization of epithelial MCF-7 CRISPR P and MCF-7 CRISPR Y537S BC cells and stromal normal fibroblasts (NFs) and cancer-associated fibroblasts (CAFs)

When we compared MCF-7 CRISPR parental (P) and MCF-7 CRISPR Y537S (YS1) we observed that mutant cells display a significant increase of growth rate evaluated in anchorage dependent (**Figure 1 A**) and anchorage independent growth (**Figure 1 B**) and higher cell migration and invasiveness (**Figure 1 C, D**).

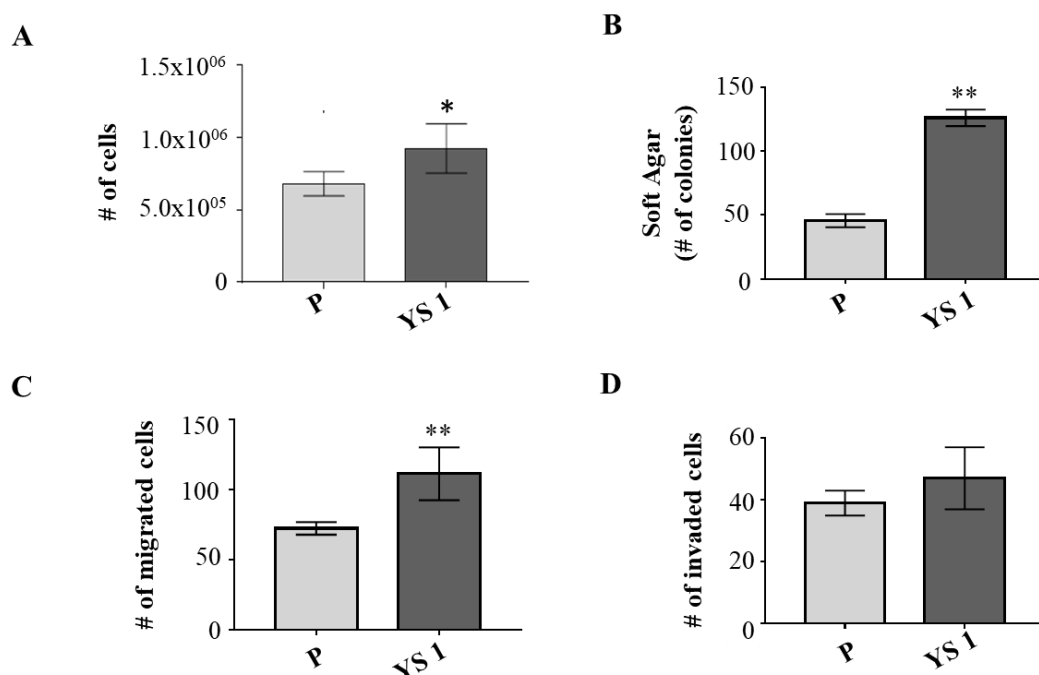


**Figure 1. Characterization of MCF-7 CRISPR Y537S (YS1) compared to MCF-7 CRISPR parental (P).** (A) Viability assay in MCF-7 CRISPR P and MCF-7 CRISPR YS1 cells. Live cells were counted after 5 days of treatments. (B) Soft agar growth assays in MCF-7 CRISPR P and MCF-7 CRISPR YS1 cells. After 14 days of growth, colonies  $\geq 50 \mu\text{m}$  were counted. Transmigration assays (C) and Invasion Assay (D) in MCF-7 CRISPR P and MCF-7 CRISPR YS1 cells. The migrated/invaded cells were DAPI-stained, counted and images were captured at 10 $\times$  magnification. The values represent the mean  $\pm$  SD of three different experiments, each performed in triplicate. \*p<0.05 \*\*p<0.01

Then, to evaluate whether MCF-7 CRISPR P and MCF-7 CRISPR YS1 could influence the proliferative, migratory and invasive capabilities of fibroblasts we create in vitro conditions that can mimic the complex in vivo microenvironment through co-culture experiments. We employed fibroblasts extracted from human mammary ductal carcinoma displaying the basic

fibroblast characteristics with long and spindle shaped morphology (**Figure 2 A**) and expressing specific markers such as Integrin Subunit Beta 1 (ITB1), Fibroblast-Specific Protein-1 (FSP1), Alpha Smooth Muscle Actin ( $\alpha$ -sma) at both mRNA (**Figure 2 B**) and protein (**Figure 2 C**) levels.

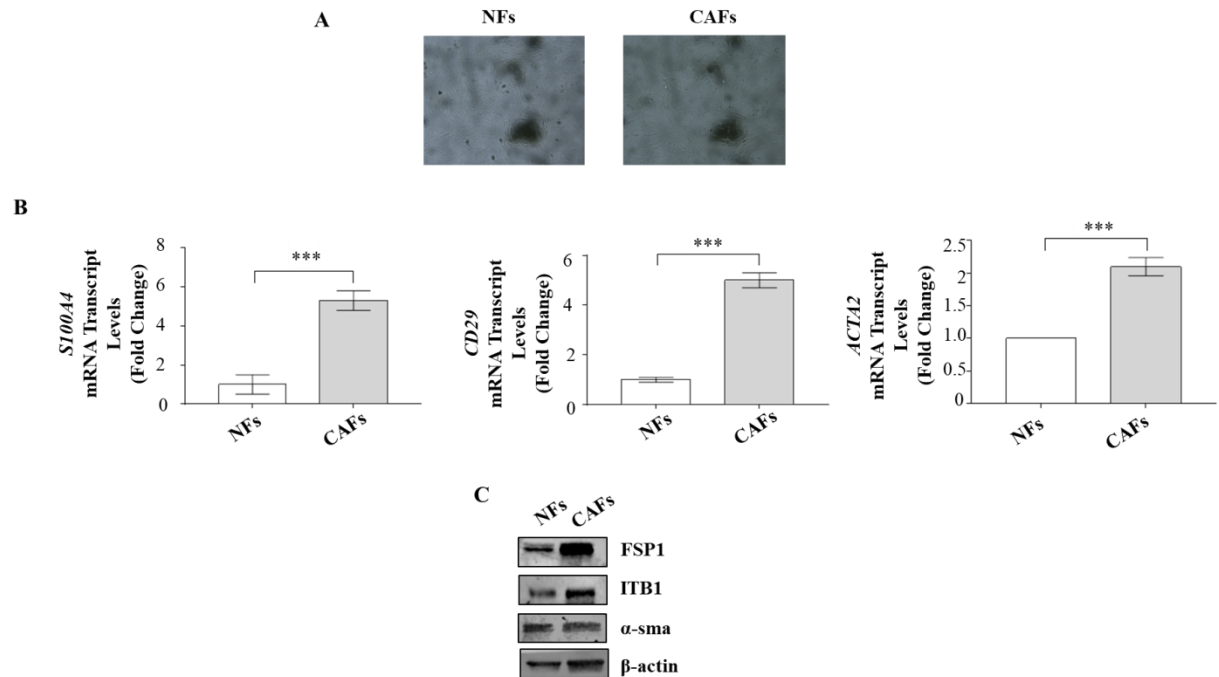


**Figure 2. Morphology of monolayer normal fibroblasts (NFs) and cancer-associated fibroblasts (CAFs) and expression of CAF specific markers.** Morphology of monolayer normal fibroblasts (NFs) (**A, left panel**) and cancer-associated fibroblasts (CAFs) (**A, right panel**) by using phase contrast microscopy. (**B**) Real time RT-PCR for *CD29* encoding for *integrin beta 1 (ITB1)*, *S100A4* encoding for *Fibroblast-Specific Protein-1 (FSP1)*, and *ACTA2* encoding for *Alpha Smooth Muscle Actin ( $\alpha$ -sma)*. NFs were used as controls. (**C**) Immunoblotting showing Fibroblast-Specific Protein-1 (FSP1) and Integrin beta 1 (ITB1) protein expression in NFs and CAFs cell.  $\beta$ -actin was used as a control for equal loading and transfer. The values represent the mean  $\pm$  S.D. of three different experiments, each performed in triplicate. \*\*\* $p < 0.001$

### Impact of MCF-7 CRISPR YS1 on proliferation, migration and invasiveness of fibroblasts

Primarily, we collected the conditioned media (CM) derived from MCF-7 CRISPR P and MCF-7 CRISPR YS1 BC cells and then we employed it in co-culture experiment with NFs/CAFs. The exposure to conditioned medium of mutant cells (MCF-7 CRISPR YS1 CM) compared to parental one (MCF-7 CRISPR P CM) induced an increase of proliferated (**Figure 3 A**) and migrated cells (**Figure 3 B**) in NFs. Moreover, NFs treated with MCF-7 CRISPR YS1

CM and MCF-7 CRISPR P CM showed the same expression levels of Fibroblast-Specific Protein-1 (*S100A4*) at mRNA (**Figure 3 C**) and protein (**Figure 3 D**) level compared to not treated cells. In contrast, integrin beta 1 (*CD29*) expression is higher in NFs cells treated with MCF-7 CRISPR YS1 CM and MCF-7 CRISPR P CM at mRNA levels (**Figure 3 C**), but not at protein levels (**Figure 3 D**). Alpha Smooth Muscle Actin ( *$\alpha$ -sma*) expression is higher in cells treated with MCF-7 CRISPR YS1 CM and MCF-7 CRISPR P CM at mRNA levels (**Figure 3 C**) and protein levels (**Figure 3 D**). Furthermore, MCF-7 CRISPR YS1 CM treatment induced an enhanced proliferation (**Figure 3 E**) and migration (**Figure 3 F**) in CAFs compared to MCF-7 CRISPR P CM. Moreover, MCF-7 CRISPR YS1 CM induced a highly Integrin beta 1 (*ITB1*) Fibroblast-Specific Protein-1 (*FSP1*) and Alpha Smooth Muscle Actin ( *$\alpha$ -sma*) at mRNA (**Figure 3 G**) and protein level (**Figure 3 H**) in CAFs compared to MCF-7 CRISPR P CM.

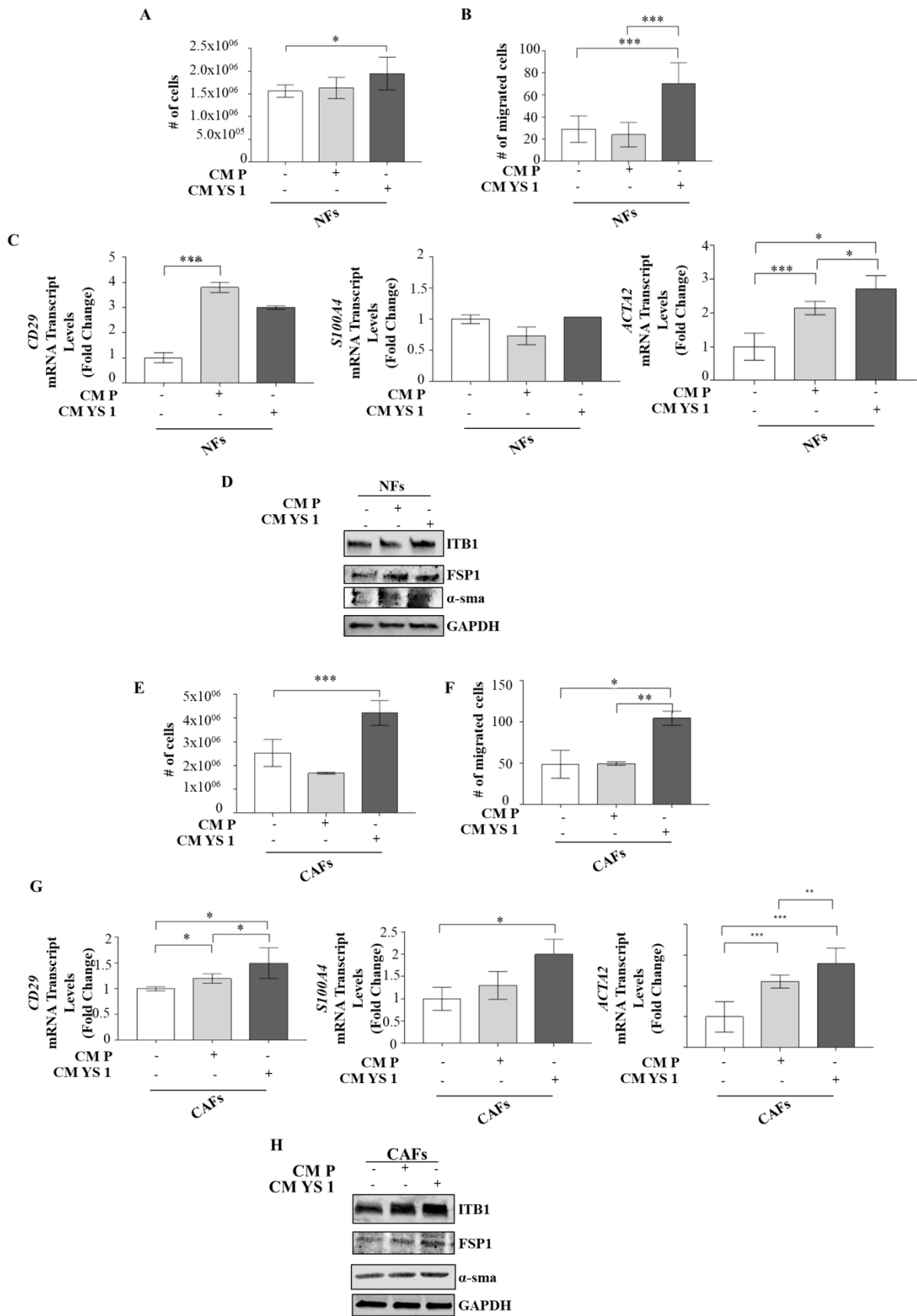
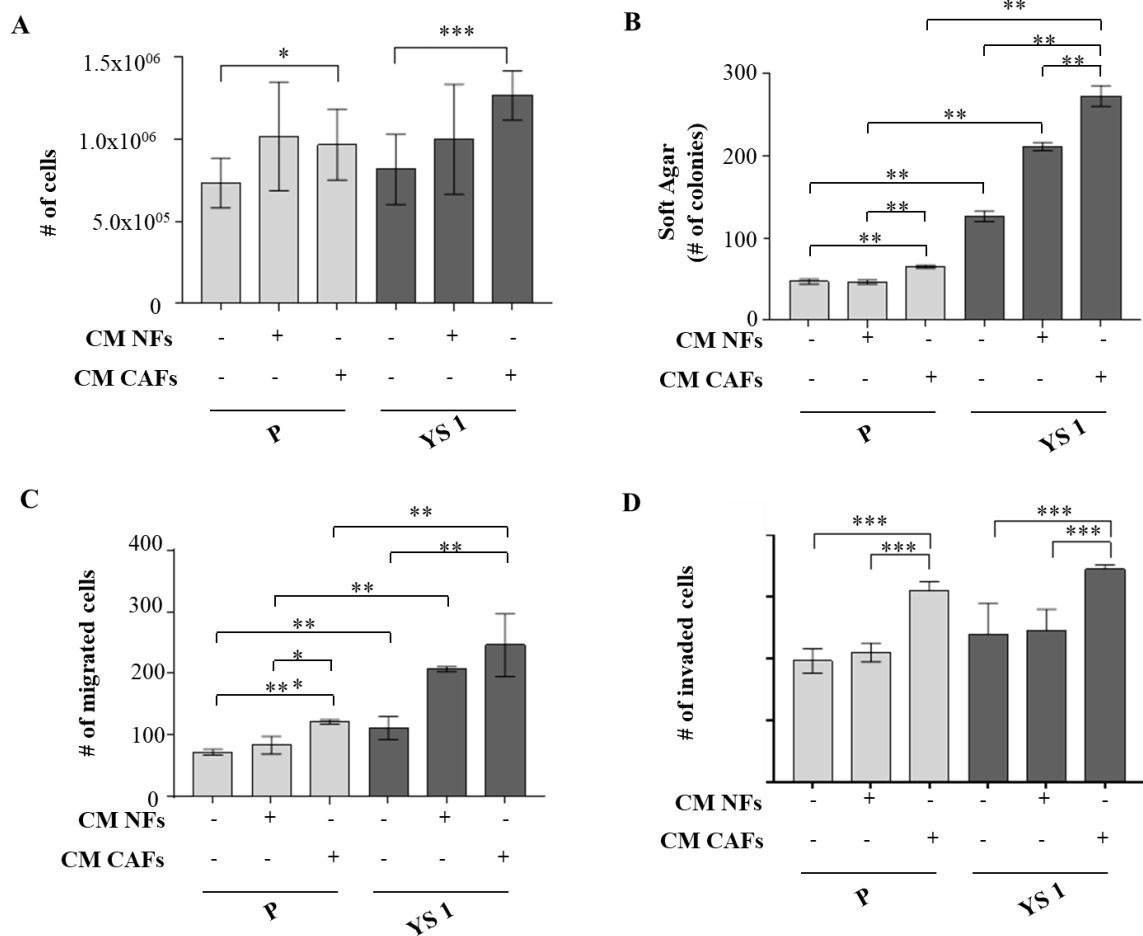


Figure 3. Biological effects of MCF-7 CRISPR P and MCF-7 CRISPR YS1 conditioned medium (CM) on NFs and CAFs. (A) Viability assay in NFs cells treated (+) or not (-) with and MCF-7 CRISPR P and MCF-7 CRISPR

YS1 CM. Live cells were counted after 5 days of treatments. **(B)** Transmigration assays in NFs treated (+) or not (-) with MCF-7 CRISPR P and MCF-7 CRISPR YS1 CM. The migrated cells were DAPI-stained, counted and images were captured at 10× magnification. **(C)** Real time RT-PCR for *CD29* encoding for *integrin beta 1 (ITB1)*, *S100A4* encoding for *Fibroblast-Specific Protein-1 (FSP1)*, and *ACTA2* encoding for *Alpha Smooth Muscle Actin ( $\alpha$ -sma)* mRNA expression in NFs treated (+) or not (-) with MCF-7 CRISPR P and MCF-7 CRISPR YS1 CM. **(D)** Immunoblotting showing FSP1 and ITB1 protein expression in NFs cells treated (+) or not (-) with MCF-7 CRISPR P and MCF-7 CRISPR YS1 CM. GAPDH was used as a control for equal loading and transfer. **(E)** Viability assay in CAFs cells treated (+) or not (-) with MCF-7 CRISPR P and MCF-7 CRISPR YS1 CM. Live cells were counted after 5 days of treatments. **(F)** Transmigration assays in CAFs treated (+) or not (-) with MCF-7 CRISPR P and MCF-7 CRISPR YS1. The migrated cells were DAPI-stained, counted and images were captured at 10× magnification. **(G)** Real time RT-PCR for *CD29* encoding for *integrin beta 1 (ITB1)*, *S100A4* encoding for *Fibroblast-Specific Protein-1 (FSP1)*, and *ACTA2* encoding for *Alpha Smooth Muscle Actin ( $\alpha$ -sma)* mRNA expression in CAFs treated (+) or not (-) with MCF-7 CRISPR P and MCF-7 CRISPR YS1 CM. **(H)** Immunoblotting showing FSP1 and ITB1 protein expression in CAFs cells treated (+) or not (-) with MCF-7 CRISPR P and MCF-7 CRISPR YS1. GAPDH was used as a control for equal loading and transfer. The values represent the mean  $\pm$  SD of three different experiments, each performed in triplicate. \* $p < 0.05$ ; \*\* $p < 0.01$ ; \*\*\* $p < 0.001$ .

### **Impact of normal fibroblasts (NFs) and cancer-associated fibroblast (CAFs) on MCF-7 CRISPR YS1 cell proliferation, migration and invasiveness compared to parental cells**

Then, to evaluate whether fibroblasts as the main component of the tumor microenvironment could influence the proliferative, migratory and invasive capabilities of the mutated cells compared to parental ones we repurpose the same experimental co-culture condition previously described. Thus, BC cells were incubated with regular media and conditioned media derived by NFs and CAFs and then we evaluated the proliferation, migration and invasion of the cells. The mutant cells MCF-7 CRISPR YS1 displayed a significantly higher growth rate evaluated in anchorage dependent (**Figure 4 A**) and anchorage independent (**Figure 4 B**) condition with respect to parental cells when exposed to conditioned media of normal fibroblasts (NFs) but in a significant higher extent when compared to conditioned media of cancer-associated fibroblasts (CAFs). Moreover, our results revealed that CAFs-derived CM increased the number of migrated and invaded compared to NFs-derived CM in both cell lines but again in higher extent in mutant cells (**Figure 4 C, D**). These data address a potential role of CAFs in influencing mutant cell phenotype.



**Figure 4. Biological effects of CAFs and NFs-derived CM on MCF-7 YS1 proliferation, migration and invasiveness.** (A) Viability assay in MCF-7 CRISPR P and MCF-7 CRISPR YS1 cells in the presence (+) or not (-) with NFs and CAFs CM. Live cells were counted after 5 days of treatment. (B) Soft agar growth assays in MCF-7 CRISPR P and MCF-7 CRISPR YS1 cells in the presence or not (-) of NFs and CAFs CM. After 14 days of growth, colonies  $\geq 50 \mu\text{m}$  were counted. (C) Transmigration assays and Invasion Assay (D) in MCF-7 CRISPR P and MCF-7 CRISPR YS1 cells in the presence or not (-) of NFs and CAFs CM. The migrated/invaded cells were DAPI-stained, counted and images were captured at 10 $\times$  magnification. The values represent the mean  $\pm$  SD of three different experiments, each performed in triplicate. \* $p < 0.05$ ; \*\* $p < 0.01$ ; \*\*\* $p < 0.001$

Our previous microarray analysis of mutant BC cells displayed an enhanced molecular signature of different cellular pathways when compared to the parental one [73]. Among them, the IGF-1R signaling pathway appears to be highly expressed in mutant cells (Table 1). This has given the rationale of the present study to investigate how this pathway may be involved in the functional interaction previously described to occur between tumor cells and fibroblasts.

Table 1. Gene expression profile between MCF-7 P and MCF-7 YS1

Gene Name	Gene Symbol	Parametric P	Fold Change in Y537S-ERα
insulin-like growth factor 1 receptor	<i>IGF1R</i>	5.33E-14	3.12772
tumor necrosis factor receptor superfamily, member 10b	<i>TNFRSF10B</i>	3.87123E-07	2.68271
chemokine (C-X-C motif) receptor 7	<i>CXCR7</i>	1.08E-08	2.59737
platelet-derived growth factor receptor-like	<i>PDGFRL</i>	8.30E-08	2.31586
insulin-like growth factor 2 receptor	<i>IGF2R</i>	1.20E-06	2.21082
interleukin 1 receptor antagonist	<i>IL1RN</i>	1.27E-07	2.18389
tumor necrosis factor receptor superfamily, member 21	<i>TNFRSF21</i>	4.80718E-05	2.07411
interleukin 6 receptor	<i>IL6R</i>	0.0001453	1.95623
chemokine (C-X-C motif) receptor 4	<i>CXCR4</i>	0.0004334	1.76009
tumor necrosis factor receptor superfamily, member 10a	<i>TNFRSF10A</i>	0.00110594	1.71354
interleukin 2 receptor, beta	<i>IL2RB</i>	6.06E-05	1.6687
interleukin 13 receptor, alpha 1	<i>IL13RA1</i>	0.0042014	1.45153
tumor necrosis factor receptor superfamily, member 11a, NFKB activator	<i>TNFRSF11A</i>	0.00121687	1.36303
leptin receptor	<i>LEPR</i>	0.0059497	1.33203
insulin receptor	<i>INSR</i>	0.0204404	1.31315

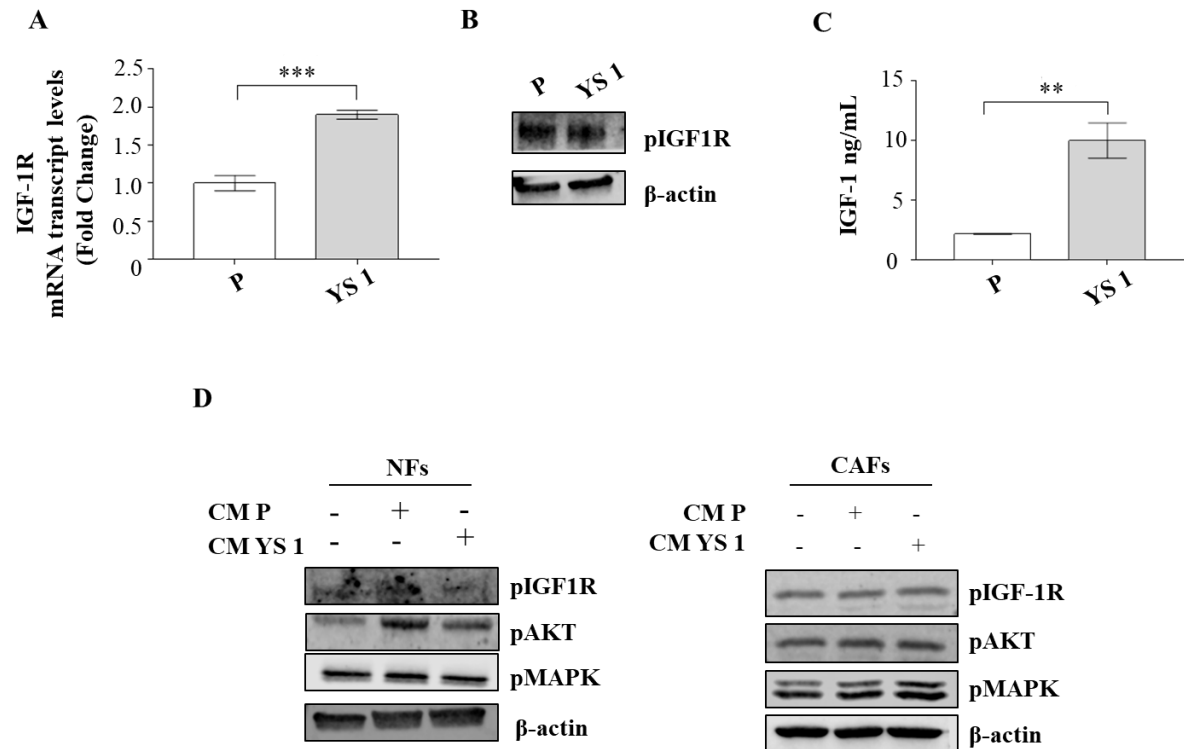
  

Gene Name	Gene Symbol	Parametric P	Fold Change in Y537S-ERα
signal transducer and activator of transcription 1, 91kDa	<i>STAT1</i>	6.28E-16	19.600
growth factor receptor-bound protein 10	<i>GRB10</i>	6.83837E-09	4.60134
Janus kinase 2	<i>JAK2</i>	3.92E-11	4.3500
Janus kinase 1	<i>JAK1</i>	1.90E-14	2.5000
signal transducer and activator of transcription 2, 113kDa	<i>STAT2</i>	5.52E-13	2.3500
signal transducer and activator of transcription 3 c (acute-phase response factor)	<i>STAT3</i>	9.49E-09	1.9700
insulin receptor substrate 1	<i>IRS1</i>	4.5046E-07	1.47789
growth factor receptor-bound protein 10	<i>GRB10</i>	0.00346207	1.37784
growth factor receptor-bound protein 14	<i>GRB14</i>	0.0192734	1.33102

Gene Name	Gene Symbol	Parametric P	Fold Change in Y537S-ERα
chemokine (C-C motif) ligand 5	<i>CCL5</i>	5.88784E-18	23.5854
growth differentiation factor 15	<i>GDF15</i>	1.52394E-15	19.8623
amphiregulin	<i>AREG</i>	1.72403E-13	14.184
interleukin 8	<i>IL8</i>	5.90176E-09	6.77423
vascular endothelial growth factor A	<i>VEGFA</i>	1.77452E-16	6.68475
tumor necrosis factor, alpha-induced protein 3	<i>TNFAIP3</i>	1.38887E-09	5.55703
transforming growth factor, alpha	<i>TGFA</i>	3.49704E-13	5.06524
tumor necrosis factor receptor superfamily, member 12A	<i>TNFRSF12A</i>	6.91309E-15	4.19699
tumor necrosis factor, alpha-induced protein 3	<i>TNFAIP3</i>	4.46592E-08	3.19933
interleukin 29 (interferon, lambda 1)	<i>IL29</i>	5.54907E-06	2.69319
IGF-like family member 1	<i>IGFL1</i>	9.1278E-07	2.53037
interleukin-1 receptor-associated kinase 1 binding protein 1	<i>IRAK1BP1</i>	9.23105E-08	2.43718
insulin-like growth factor binding protein 4	<i>IGFBP4</i>	3.05135E-07	2.09977
chemokine (C-X-C motif) ligand 12	<i>CXCL12</i>	4.49558E-06	1.92702
interleukin 28A (interferon, lambda 2)	<i>IL28A</i>	0.000292439	1.84051
interleukin 15	<i>IL15</i>	6.42523E-07	1.833
chemokine-like factor	<i>CKLF</i>	6.77319E-08	1.78912
chemokine (C-X-C motif) ligand 3	<i>CXCL3</i>	0.00146937	1.69364
TGFβ-induced factor homeobox 1	<i>TGIF1</i>	0.000335814	1.67469
cytokine inducible SH2-containing protein	<i>CISH</i>	0.000155763	1.66924
chemokine (C-X-C motif) ligand 10	<i>CXCL10</i>	0.000358225	1.64099
fibroblast growth factor binding protein 3	<i>FGFBP3</i>	0.00107342	1.6382
fibroblast growth factor 18	<i>FGF18</i>	0.000357465	1.54182
interleukin 23, alpha subunit p19	<i>IL23A</i>	0.00428665	1.53072
tumor necrosis factor (ligand) superfamily, member 13	<i>TNFRSF13</i>	6.53362E-06	1.49261
tumor necrosis factor receptor superfamily, member 21	<i>TNFRSF21</i>	0.00107731	1.46684
chemokine (C-X-C motif) ligand 11	<i>CXCL11</i>	0.000137068	1.44488
insulin-like growth factor binding protein 3	<i>IGFBP3</i>	0.00408461	1.43366
epidermal growth factor receptor pathway substrate 15-like 1	<i>EPS15L1</i>	0.0113674	1.35099
fibroblast growth factor 12	<i>FGF12</i>	0.0399874	1.31409

As expected, MCF-7 CRISPR YS1 cells displayed high IGF-1R mRNA level (**Figure 5A**) and highly phosphorylated IGF-1R (pIGF-1R) protein expression (**Figure 5B**) compared to parental one. Interestingly, ELISA assay showed a markedly higher amount of IGF-1 in MCF-7 CRISPR YS1 CM with respect to the parental counterpart (**Figure 5C**). Consequently, we found that MCF-7 CRISPR YS1 CM sustains a major activation of IGF-1 pathway in NFs (**Figure 5D, left panel**) and CAFs (**Figure 5D, right panel**) detected by a higher phosphorylated status of IGF-1R and downstream effectors AKT and MAPK compared to MCF-7 P CM.



**Figure 5. Effects of MCF-7 CRISPR P and MCF-7 CRISPR YS1-derived CM in activating IGF-1/IGF-1R pathway in fibroblasts.** (A) Real time RT-PCR for IGF-1R mRNA expression in MCF-7 CRISPR P and MCF-7 CRISPR YS1 cells. (B) Immunoblotting showing pIGF-1R protein expression in MCF-7 CRISPR P and MCF-7 CRISPR YS1 cells.  $\beta$ -actin was used as a control for equal loading and transfer. (C) E-linked immunosorbent assay (ELISA) for IGF-1 secretion in MCF-7 CRISPR P and MCF-7 CRISPR YS1 cells. (D) Immunoblotting showing pIGF-1R, pAKT and pMAPK protein expression in NFs and CAFs treated (+) or not (-) with MCF-7 CRISPR P and MCF-7 CRISPR YS1 CM (**left panel**), and pIGF-1R, pAKT and pMAPK protein expression in MCF-7 CRISPR P and MCF-7 CRISPR YS1 cells treated (+) or not (-) with NFs and CAFs CM (**right panel**).  $\beta$ -actin was used as a control for equal loading and transfer. The values represent the mean  $\pm$  SD of three different experiments, each performed in triplicate. \*\* $p < 0.01$ ; \*\*\* $p < 0.001$

On the other side, we noticed that NFs and CAFs exhibited similar levels of the IGF-1R mRNA expression (**Figure 6A**), while interestingly CAFs showed an enhanced phosphorylated status of IGF-1R (**Figure 6B**). Although IGF-1 secretion were similar between the two employed fibroblast cell lines (**Figure 6C**) the exposure to CM of both fibroblasts type induce a major activation of IGF-1R in mutant clones (**Figure 6D**).

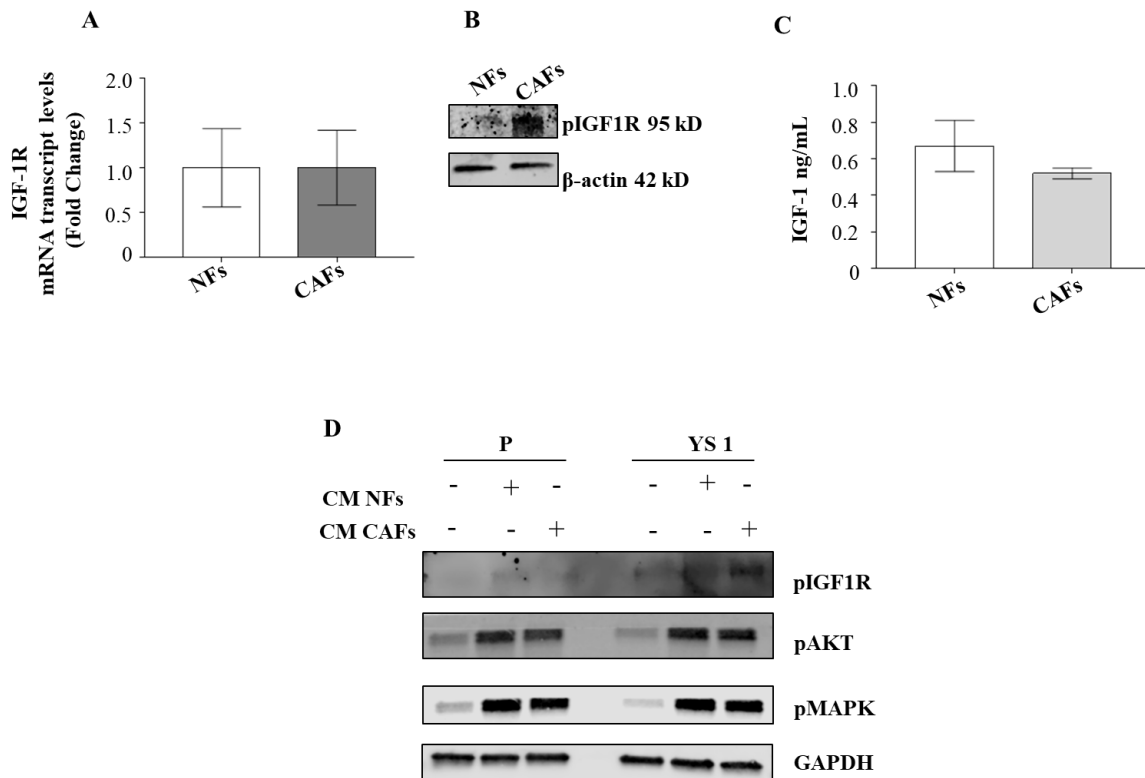


**Figure 6.** Effects of NFs and CAFs-derived CM in activating IGF-1/IGF-1R pathway in MCF-7 CRISPR P and MCF-7 CRISPR YS1. (A) Real time RT-PCR for IGF-1R mRNA expression in NF and CAF cells. (B) Immunoblotting showing pIGF-1R protein expression in NF and CAF cells.  $\beta$ -actin was used as a control for equal loading and transfer. (C) E-linked immunosorbent assay (ELISA) for IGF-1 secretion in NF and CAF cells. (D) Immunoblotting showing pIGF-1R, pAKT and pMAPK protein expression in MCF-7 CRISPR P and MCF-7 CRISPR YS1 cells treated (+) or not (-) with NFs and CAFs CM. GAPDH was used as a control for equal loading and transfer. The values represent the mean  $\pm$  SD of three different experiments, each performed in triplicate.

### Molecular mechanisms involved in ESR1m/tumor microenvironment crosstalk

To gain more insight into the molecular background sustaining the altered pattern of tumor cell proliferation, migration and invasiveness of mutant cells with respect to parental one we performed a proteomic analysis. By employing label-free liquid chromatography-tandem mass spectrometry (LC-MS/MS) and by using the data independent acquisition method we identified 3827 proteins depicted in ranked protein graph aiming to show the protein coverage (**Figure 7A**). The protein abundance differential-analysis, performed between MCF-7 CRISPR P and MCF-7 CRISPR YS1, showed a consistent profile changes in MCF-7 CRISPR YS1 compared to MCF-7 CRISPR, as reported in the principal component analysis (PCA) plot. Particularly, the proteomics was performed by using three independent experiments (MCF-7 P 1/2/3 and MCF-7 YS 1/2/3) and the graph clearly showed that the two cell line

(MCF-7 CRISPR depicted through red dots and MCF-7 CRISPR YS1 depicted through green dots) are well clustered in the plot as a function of the variance (**Figure 7B**).

The proteomic analysis allowed us to identify 571 significant proteins modulated in MCF-7 CRISPR YS1 compared to MCF-7 CRISPR P. Of these, the heatmap clearly evidenced 324 up-regulated proteins (red dots) and 247 down-regulated proteins (blue dots) in MCF-7 CRISPR YS1 compared to MCF-7 CRISPR P (**Figure 7C**).

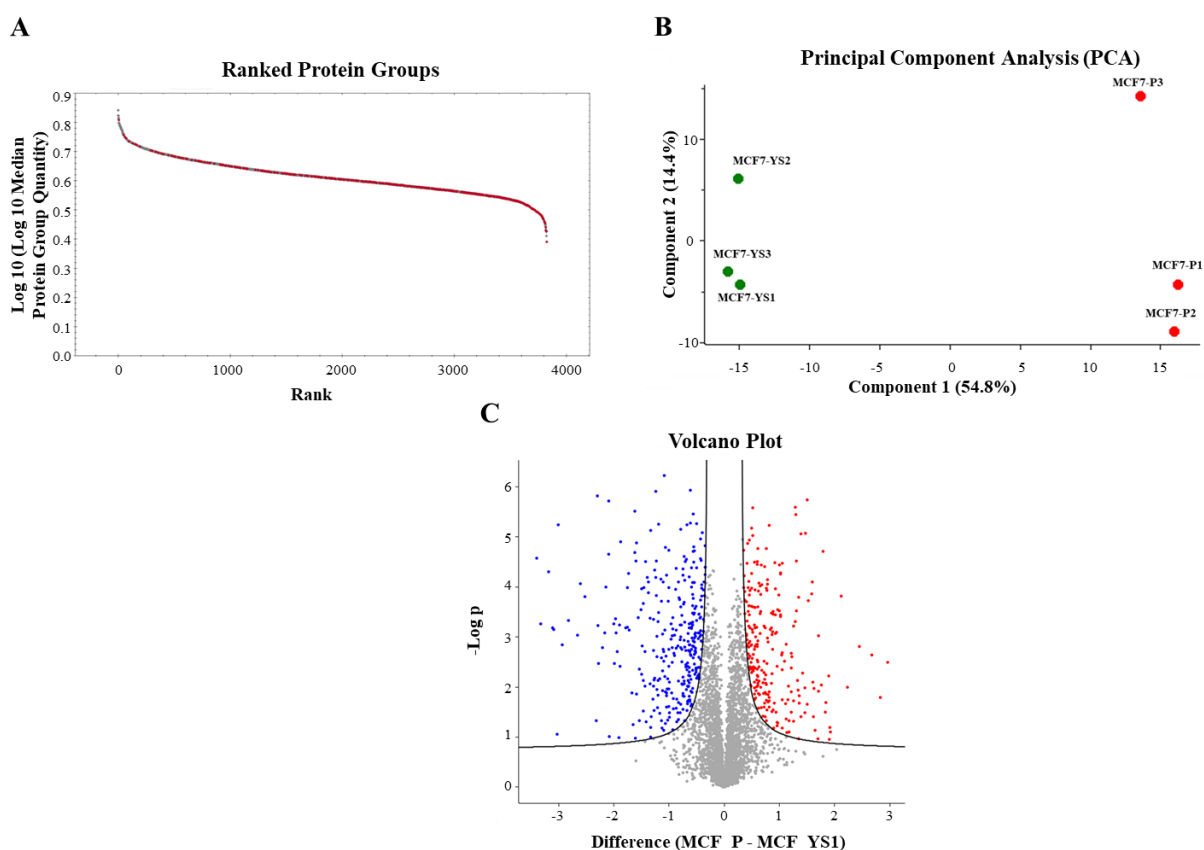


**Figure 7. Proteomic pattern differences between MCF-7 CRISPR P and MCF-7 CRISPR YS1 BC cells.** Proteomic was performed using three replicate samples of MCF-7 CRISPR P and MCF-7 CRISPR YS1 cells. **(A)** Rank-intensity plot for MCF-7 CRISPR P and MCF-7 CRISPR YS1 are shown. The mean of LFQ intensities for each protein in each group has been calculated. Proteins were subsequently ranked from highest to lowest based on the LFQ intensity **(B)** Scatter plot of principal component axis (PCA) of MCF-7 YS1 cells compared with MCF-7 CRISPR. Each condition was performed in triplicates and groups clearly cluster. **(C)** Volcano plots showing the most significant differentially expressed proteins. Red color shows the upregulated proteins and blue color shows the downregulated proteins.

Since transcriptomic profiles generally can not perfectly match with the corresponding proteomic ones, we examined how many up-regulated genes in MCF-7 CRISPR YS1 cells previously detected in microarray [73] were in common with the up-regulated proteins identified in proteomic analysis by using a cut off of 1.3 fold. **Figure 8A** showed a Venn diagram (<https://bioinfogp.cnb.csic.es/tools/venny/>) with the gene/protein distribution of MCF-7 CRISPR YS1 and MCF-7 CRISPR P. Our results revealed that 145 genes/proteins were found commonly up-regulated by matching proteomic and microarray data (**Figure 8A**).

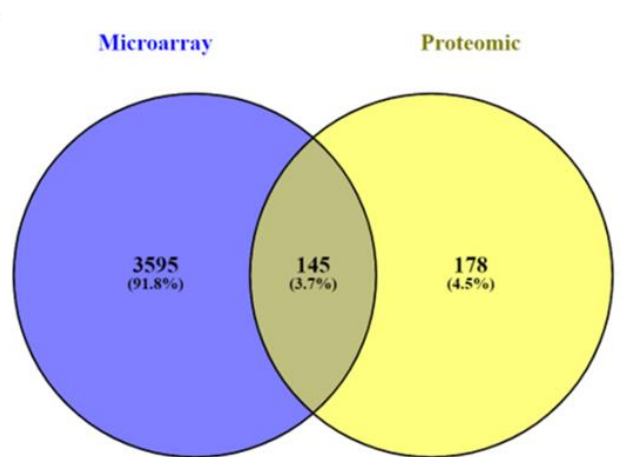


**Figure 8. Common genes/proteins between the transcript and protein pattern analysis in MCF-7 CRISPR P and MCF-7 CRISPR YS1.** (A) Venn diagram comparing differentially upregulated genes identified from microarray and proteomic data (FC 1,3) in MCF-7 CRISPR YS1 cells compared to MCF-7 CRISPR P.

To deeply investigate the biological processes and pathways in which the common 145 genes/proteins are involved we performed FunRich (<http://www.funrich.org>) analyses to obtain Gene Ontology (GO) enrichments. Indeed, in the context of biological process the significantly up-regulated proteins were clustered in “immune response” (11.7%) (**Figure 9A left panel**). Among the biological pathway the significantly investigated proteins were clustered in “interferon alpha/beta signaling” (15.4%), “interferon signaling” (16.7%), “antigen presentation: folding, assembly, and peptide loading of class I MHC” (9%), “cytokine signaling in immune system” (19.2%), “immune system” (29.5%), and “interferon gamma signaling” (10.3%) (**Figure 9A right panel**).

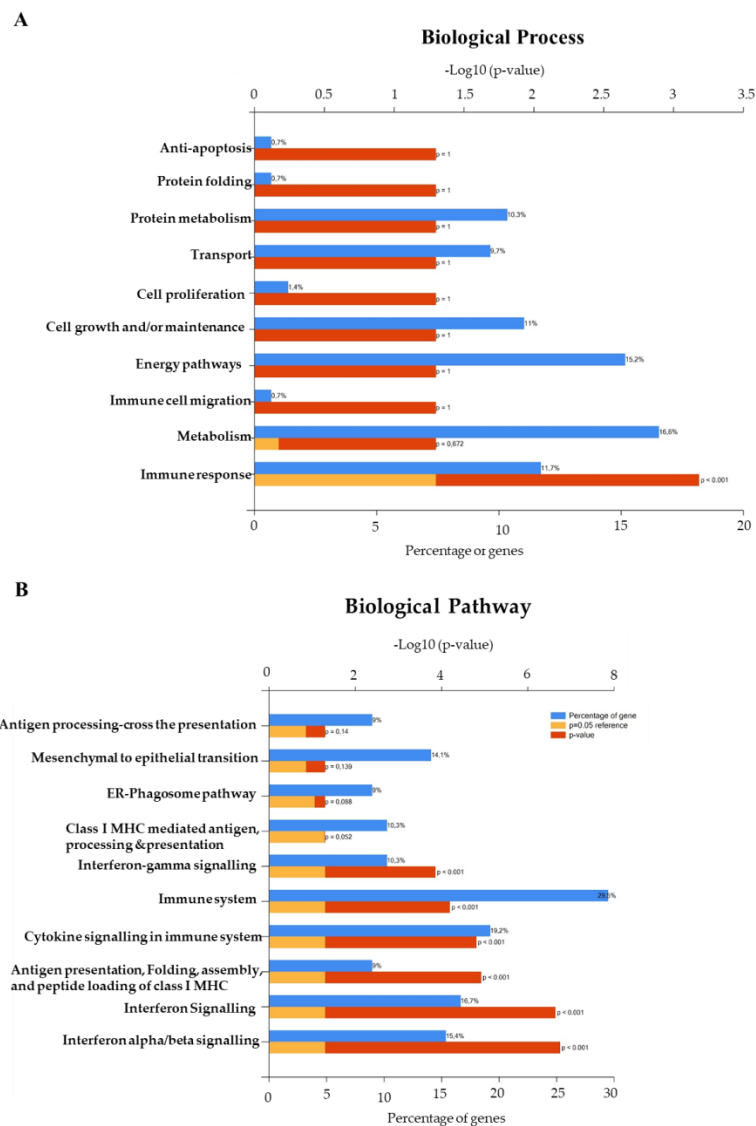


**Figure 9. Functional enrichment analysis of the identified de-regulated proteins in MCF-7 CRISPR P and MCF-7 CRISPR YS1.** The top ten pathways in which the 145 common up-regulated genes/proteins were significantly involved are shown (ranked by p-value using the FunRich software). A p-value <0.05 was considered significant. Gene Ontology-based Biological Process (A) and Gene Ontology-based Biological Pathway (B) abundant in MCF-7 CRISPR YS1 compared to MCF-7 CRISPR P are displayed.

To explore the direct interaction network (DIN) in which the 145 genes are involved we selected the direct interaction algorithm by using Metacore network building tool. The resulting DIN revealed STAT1, STAT3, NF-kB1, NF-kB and IRF9 as the main hubs (**Figure 10**).

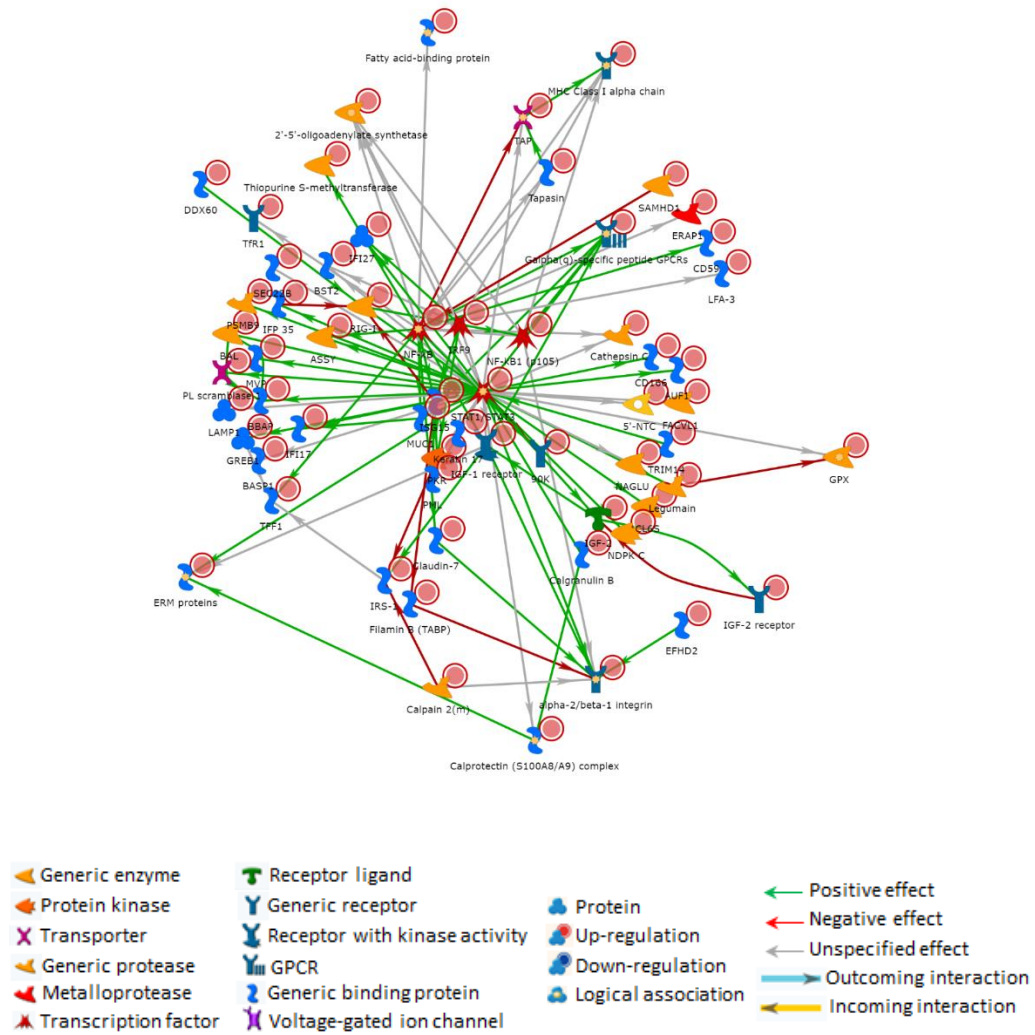


**Figure 10. Direct interaction network (DIN) built by processing genes/proteins upregulated in MCF-7 CRISPR YS1 compared to MCF-7 CRISPR P.** Experimental DIN genes/proteins marked by red spot are upregulated. Functions of different network items are identified by different symbols.

### IGF-1R as potential target to overcome ESR1m/fibroblasts interaction

Within the DIN, conducted in the 145 common upregulated genes/proteins derived from microarray and proteomic analysis in MCF-7 CRISPR YS1 compared to parental, Metacore give relevance to 5 potential therapeutic target, surrounded in **Figure 11** with a blue circle: Bone Marrow Stromal Cell Antigen 2 (*BST2*), Nuclear factor kappaB (*NF-kB*), Mucin 1 (*MUC1*), and insulin like growth factor 1 receptor (*IGF-1R*).

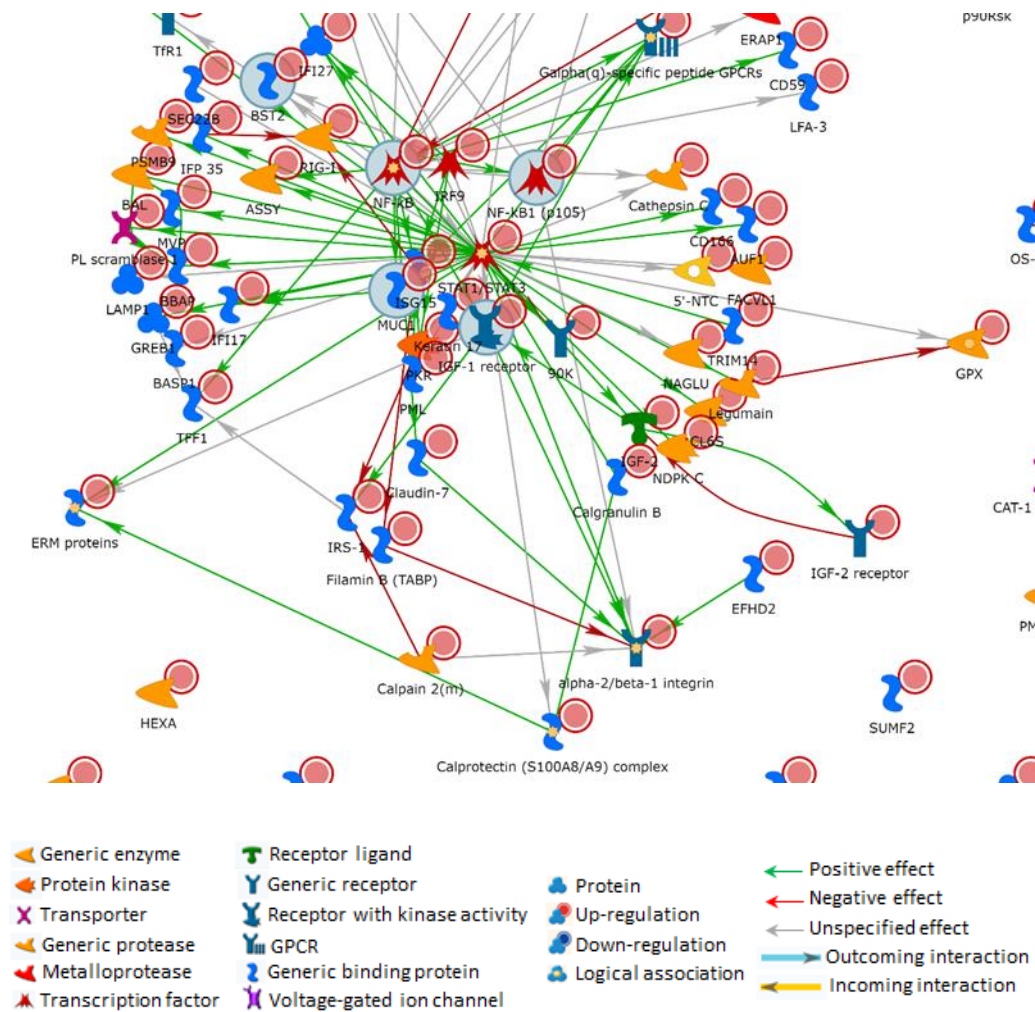


**Figure 11. Direct interaction network (DIN) representing the potential therapeutic target built by processing genes/proteins upregulated in MCF-7 CRISPR YS1 compared to MCF-7 CRISPR P.** Experimental DIN genes/proteins marked by red spot are upregulated in MCF-7 CRISPR YS1 compared to MCF-7 CRISPR P. Functions of different network items are identified by different symbols. The blue circles around the Bone Marrow Stromal Cell Antigen 2 (BST2), Nuclear factor kappaB (NF-kB), Mucin 1 (MUC1), and insulin like growth factor 1 receptor (IGF-1R) identify the potential therapeutic targets.

Among the five 5 pontential therapeutic target, IGF-1R, already found to be markedly upregulated in microarray, resulted again to be central in the analysis conducted through Metacore regarding the therapeutic target. On the other hand, this reinforces previous findings that well documented the role of IGF-1R signaling in interfering with endocrine responsiveness [22]. Thus, on the basis of the latter findings, it was reasonable to explore how an inhibitor of IGF-1R, GSK1838705A, may interfere with IGF-1/IGF-1R autocrine loop in tumor cells as well as in paracrine interaction between BC cells and CAFs wherein IGF-1R signaling resulted upregulated. Our data demonstrated that IGF-1R inhibition markedly

reduced proliferation and migration of mutant cells compared to parental (**Figure 12 A,B**). It has been also showed that the use of GSK1838705A reduced the induced effect of NFs and CAFs CM in both BC cells but markedly in mutant clones (**Figure 12 A,B**). The exposure to the CM of MCF-7 CRISPR YS1 induced a slight increase of NF proliferation evidencing not noticeable effects upon GSK1838705A (**Figure 12 C**). On the contrary, we observed a strong upregulation of NF migration after treatment with MCF-7 CRISPR YS1 CM which was markedly reversed by GSK1838705A (**Figure 12 D**). On the other hand, CAF proliferation was significantly increased upon MCF-7 CRISPR YS1 CM. The latter effect was reversed by GSK1838705A (**Figure 12 E**). A similar pattern was also noticed for CAF migration (**Figure 12 F**).

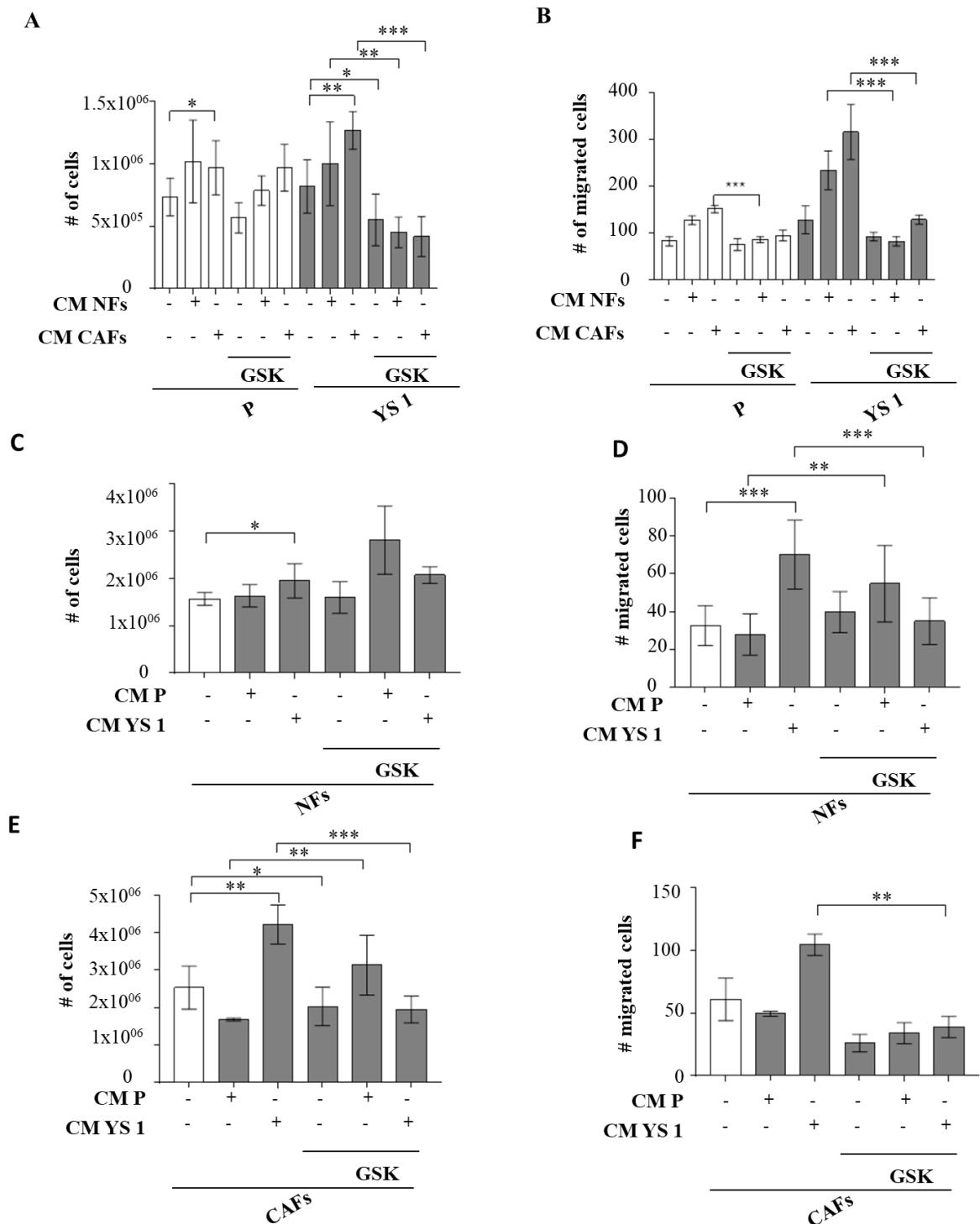


**Figure 12. Impact of IGF-1R inhibition by using GSK1838705A treatment in stromal and epithelial cell proliferation and migration. (A)** Viability assay in MCF-7 CRISPR P and MCF-7 CRISPR YS1 cells in the presence (+) or not (-) with NFs and CAFs conditioned medium (CM) and/or 1  $\mu$ M GSK1838705A. Live cells were counted after 5 days of treatment. **(B)** Transmigration assays in MCF-7 CRISPR P and MCF-7 CRISPR YS1 cells in the presence or not (-) of NFs and CAFs CM and/or 1  $\mu$ M GSK1838705A. The migrated cells were DAPI-stained, counted and images were captured at 10 $\times$  magnification. **(C)** Viability assay in NFs in the presence (+) or not (-) of MCF-7 CRISPR P and MCF-7 CRISPR YS1 cells CM and/or 1  $\mu$ M GSK1838705A. Live cells were counted after 5

days of treatment. **(D)** Transmigration assays in NFs in the presence (+) or not (-) of MCF-7 CRISPR P and MCF-7 CRISPR YS1 cells CM and/or 1  $\mu$ M GSK1838705A. The migrated cells were DAPI-stained, counted and images were captured at 10 $\times$  magnification. **(E)** Viability assay in CAFs in the presence (+) or not (-) of MCF-7 CRISPR P and MCF-7 CRISPR YS1 cells CM and/or 1  $\mu$ M GSK1838705A. Live cells were counted after 5 days of treatment. **(F)** Transmigration assays in CAFs in the presence (+) or not (-) of MCF-7 CRISPR P and MCF-7 CRISPR YS1 cells CM and/or 1  $\mu$ M GSK1838705A. The migrated cells were DAPI-stained, counted and images were captured at 10 $\times$  magnification. The values represent the mean  $\pm$  SD of three different experiments, each performed in triplicate. \* $p$ <0.05; \*\* $p$ <0.01; \*\*\* $p$ <0.001

Based on these results showing that IGF1-R inhibition may counteract tumor-fostering ability of CAFs and may reduce the proliferative and migratory effects of ESR1m cells “in vitro”, we better evaluated the role of GSK1838705A in affecting ESR1m BC growth “in vivo”. To reproduce the complex interaction between ESR1m BC cells and CAFs within a tumor microenvironment, MCF-7 CRISPR P or MCF-7 CRISPR YS1 cells were co-implanted with CAFs into the mouse orthotopic region and tumor growth was observed after the treatment with vehicle or 30 mg/kg/day GSK1838705A. First of all, we didn’t observe any modifications in body mass, food/water ingestion, and motor function aiming that the administration was well accepted. Moreover, we didn’t notice any changes in terms of weight and the histology features of the main organs (i.e., liver, lung, spleen, and kidney) between vehicle- and GSK1838705A-treated mice, excluding a toxic effects of the dose used. Our data demonstrated how MCF-7 CRISPR P BC cells when co-injected with CAFs (MCF-7 CRISPR P/CAF) displayed a significant increase of relative tumor volume in the first and third week of monitoring (**Figure 13 A left panel**). While, MCF-7 CRISPR YS1 BC cells when co-injected with CAFs (MCF-7 CRISPR YS1/CAF) showed an increase of relative tumor volume along the entire period of monitoring (**Figure 13 A right panel**). Interestingly, GSK1838705A treatment was able to induce a significant regression in tumor growth of both MCF-7 CRISPR P/CAF and MCF-7 CRISPR YS1/CAF (**Figure 13 B left and right panel respectively**). To differentiate epithelial and connective components, MCF-7 CRISPR P and MCF-7 CRISPR YS1/CAF samples were stained with hematoxylin and eosin or Azan trichrome stain (**Figure 13 C**). Cytokeratin 18 and  $\alpha$ -SMA human antibody were used to validate the human epithelial and connective origin in examined tissues. Interestingly, GSK1838705A treatment evidences a reduced immunoreactivity of cytokeratin 18,  $\alpha$ -sma, Ki67 in MCF-7 CRISPR P and MCF-7 CRISPR YS1 BC cells either in the presence or not of CAFs. The latter inhibitory event appear much more marked into MCF-7 CRISPR YS1

(Figure 13 C). All these results how GSK1838705A treatment may be engaged in antagonize the crosstalk between BC cells/stroma sustaining tumor growth and progression.

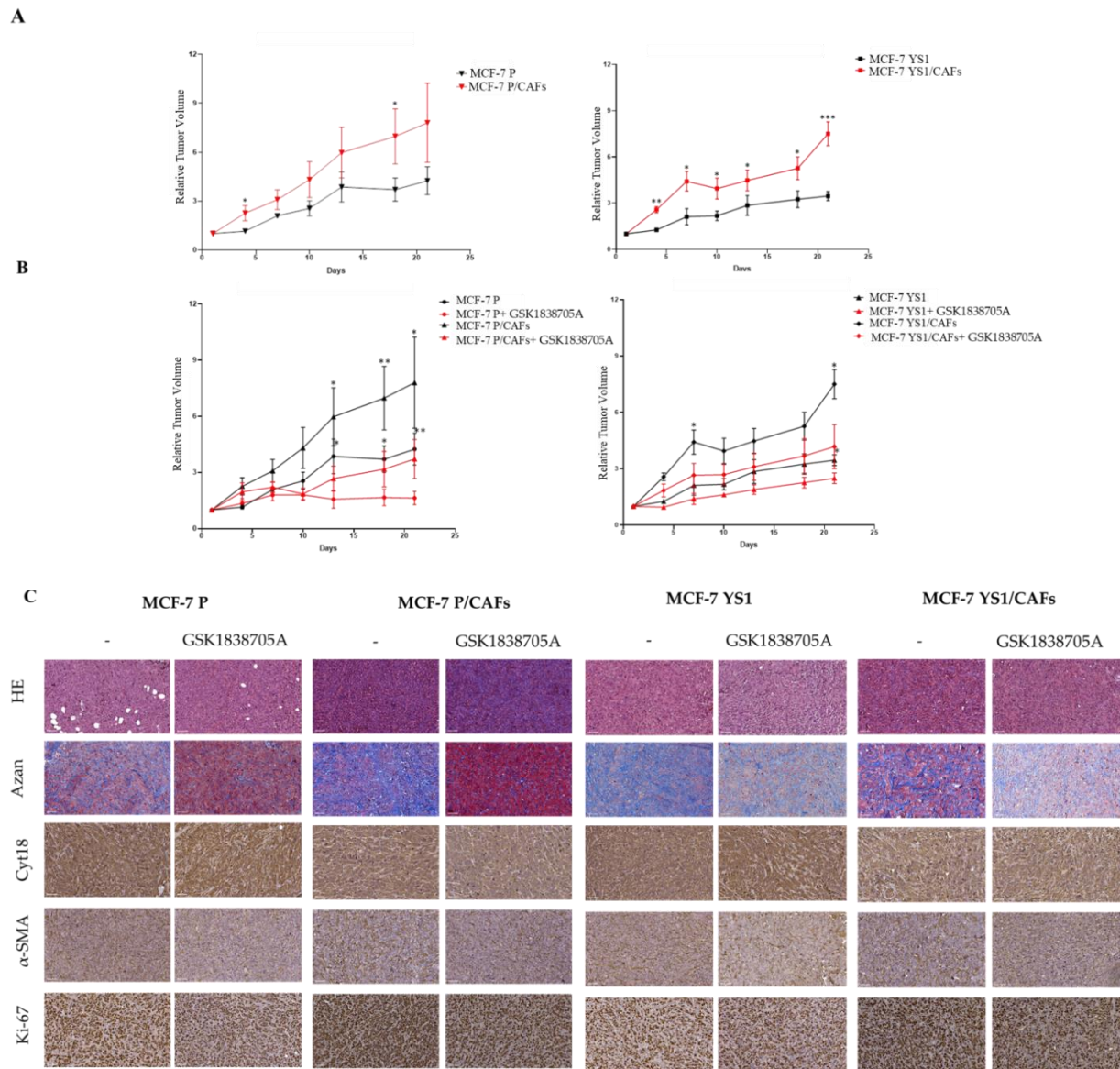


**Figure 13.** Impact of GSK1838705A treatment on relative tumor volume of MCF-7 CRISPR P/CAF and MCF-7 CRISPR YS1/CAF xenografts. MCF-7 CRISPR P cells and MCF-7 CRISPR YS1 were co-injected with CAFs subcutaneously into nude mice (4 mice/each group) (A). Vehicle (-) and GSK1838705A treatment (30 mg/kg/day) were started when tumor size reached 150 mm<sup>3</sup> (day 0) and delivered daily to the animals via oral-administration (B). Relative tumor volume mean  $\pm$  SEM is shown. (C) Representative images of hematoxylin and eosin (H&E), azan, human cytokeratin 18 (CK18),  $\alpha$ -SMA, and Ki-67 of MCF-7 CRISPR P, MCF-7 CRISPR P/CAF, MCF-7 CRISPR YS1, MCF-7 CRISPR YS1/CAF immunohistochemical staining. Scale bar = 70  $\mu$ m. \*  $p < 0.05$ ; \*\*  $p < 0.002$  \*\*\*  $p < 0.0002$ .

AIM 2:

**to explore the molecular mechanisms underlying the BC cell/adipocyte crosstalk and Tamoxifen Resistance.**

## Impact of 3T3L1 mature adipocyte-derived conditioned medium on growth, motility, and invasion of MCF-7 and MCF-7 Tamoxifen-resistant (TR) BC cells

In order to assess the role of adipocytes in the mechanism of Tamoxifen resistance, we used fully differentiated 3T3L1A, a widely used "in vitro" model of white adipocytes. The mature adipocytes, obtained from the differentiation of 3T3-L1 preadipocytes using a specific media containing adipogenesis inducers, were characterized by: i) phase contrast microscopy, showing the transition from the elongated shape (typical of preadipocyte 3T3L1) to the typical spherical one of mature adipocytes (3T3L1A), and the presence of lipid droplets in the cytoplasm (**Figure 1A**); ii) neutral lipid content (**Figure 1B**); iii) expression of specific adipocyte markers (**Figure 1C**).

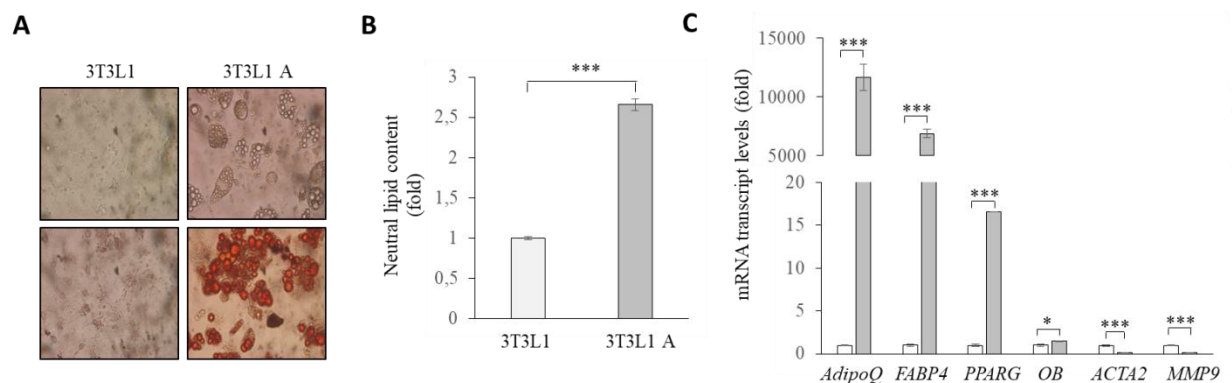


**Figure 1. Characterization of 3T3L1 mature adipocytes.** (A) The representative phase contrast (*upper panel*) and oil red O staining (*lower panel*) images of 3T3L1 cells at the preadipocyte (3T3L1) and adipocyte (3T3L1A) stages (40X); (B) Neutral lipid content of oil red O staining of 3T3L1 and 3T3L1A were quantified eluting red O dye with isopropanol and then measuring optical density (OD) at 490 nm using a spectrophotometer; (C) Real-time RT-PCR for different adipocyte markers such as *AdipoQ* (*Adiponectin C1Q*), *FABP4* (*Fatty Acid Binding Protein 4*), *PPARG* (*Peroxisome Proliferator-Activated Receptor gamma*), *OB* (*Leptin*) and pre-adipocyte markers such as *ACTA2* (*Alpha Smooth Muscle Actin*) and *MMP9* (*Matrix Metalloproteinase 9*). Mean  $\pm$  S.E.M., n = 6. \*p<0.05; \*\*p<0.005.

Conditioned medium (CM) was collected from 3T3L1A mature adipocytes, and used in the co-culture experiments with MCF-7 BC cells in the presence or absence of the antiestrogen Tamoxifen (Tam). The MCF-7 BC cell line resistant to Tamoxifen (MCF-7 TR) was chosen as a further experimental model to evaluate the growth of TR cells in the presence or absence of the 3T3L1A CM. First, anchorage-dependent (**Figure 2A**) and -independent (**Figure 2B**)

growth assays were performed. As expected, Tam significantly reduced the proliferation of MCF-7 cells, while 3T3L1A CM increased cell growth in both assays. Interestingly, incubation of MCF-7 cells with 3T3L1A CM counteracted the inhibitory effects of Tamoxifen and TR cell growth was amplified by 3T3L1A CM. We then examined the ability of 3T3L1A CM with/without Tamoxifen to influence cell movement in wound-healing assays (**Figure 2C**). 3T3L1A CM promoted net movement of MCF-7 cells and Tamoxifen was not able to reduce cell motility. As shown for proliferation assays, CM-treated MCF-7 TR cells moved at higher rate to close the gap in the cell bed compared to CM-treated MCF-7 cells. The capacity of cells to migrate across uncoated membrane in transmigration assays or invade an artificial basement membrane Matrigel in invasion assays was also tested in our experimental conditions (**Figure 2D**, and **Figure 2E**, respectively). Our data clearly showed that 3T3L1A CM reduced the sensitivity on MCF-7 cells to the inhibitory effects of Tamoxifen on motility and invasion. It is worth to mention that the motile and invasive behaviour of TR cells was dramatically increased in the presence of 3T3L1A CM, further suggesting a supportive role of adipocyte secretome in the development and progression of endocrine-resistant phenotypes.

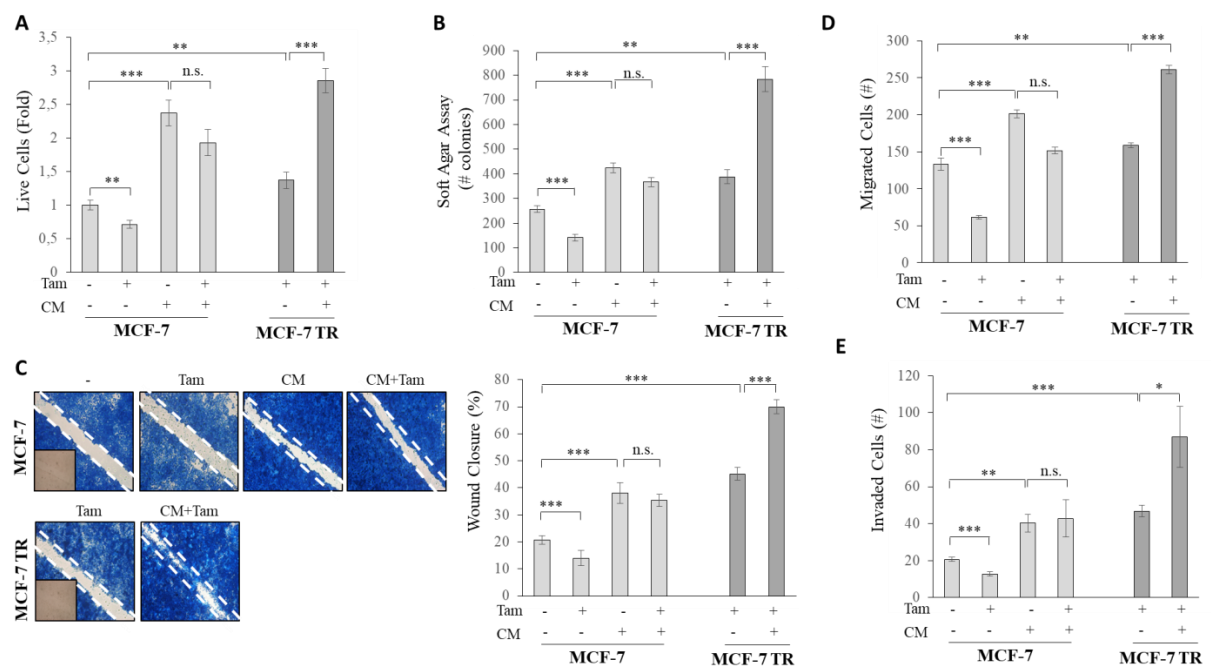


**Figure 2. Effects of 3T3L1A CM on growth, motility, and invasion of MCF-7 and MCF-7 TR BC cells. (A)** Viability assay in MCF-7 and MCF-7 TR cells treated (+) or not (-) with Tam and/or mature adipocyte conditioned medium (CM). Live cells were counted after 48h of treatment. Results are the mean of the live cells  $\pm$  SEM of three

separate experiments. **(B)** Soft agar growth assays in MCF-7 and MCF-7 TR cells treated as indicated. After 14 days of growth, colonies  $\geq 50 \mu\text{m}$  were counted. **(C)** Wound healing assay in MCF-7 and MCF-7 TR cells treated as indicated for 24h. Inset, time 0. Pictures are representative of wound closure in three independent experiments (*left panel*), the histograms represent the relative percentage of wound closure calculated by image analysis using Scion Image software (*right panel*). Boyden chamber transmigration **(D)** and invasion **(E)** assays in MCF-7 and MCF-7 TR cells treated as indicated for 5h. The migrated/invaded cells were DAPI-stained, counted, and images were captured at 10 $\times$  magnification. The bar charts represent the mean of the migrated and invaded cells  $\pm$  SEM. n.s., non significant; \* $p < 0.05$ ; \*\* $p < 0.005$ ; \*\*\* $p < 0.0005$ .

### **3T3L1 mature adipocyte-derived conditioned medium impacts TXNIP expression and activity**

To gain insights into the molecular mechanisms underlying the phenotypic modulations induced by 3T3L1A CM in endocrine therapy resistance in BC cells, RNA-sequencing analysis in MCF-7 and MCF-7 TR cells treated with CM was performed. The transcript abundance differential-analysis unravelled a consistent transcriptional modulation. All the common (~17400) genes between MCF-7 and MCF-7 TR cell datasets were analyzed through MixOmics-MINT tool to identify reproducible signatures of 3T3L1A CM effect on recipient cells and to characterize functions of 3T3L1A CM. MixOmics analysis detected 27 genes commonly modulated by 3T3L1A CM between MCF-7 and MCF-7 TR cells. The supervised hierarchical clustering analysis of the 27 genes is shown in **Figure 3A** along with the horizontal bar plot visualizing the mean value of contribution in criterion assesses of each gene (**Figure 3B**).

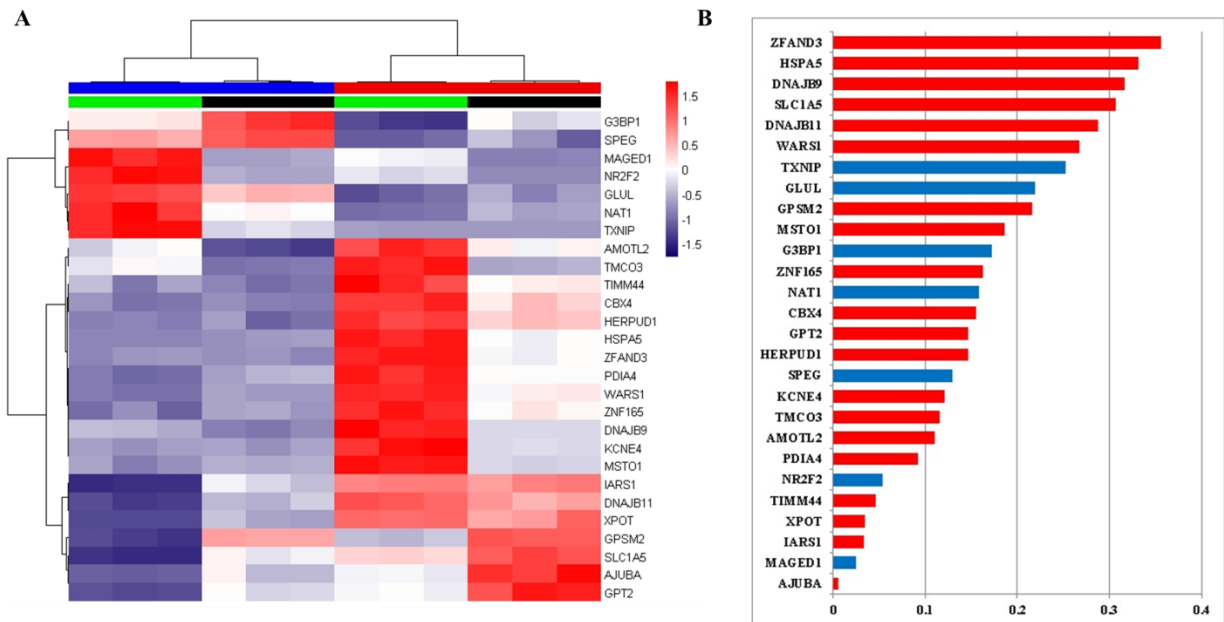


**Figure 3. (A)** Correlation heatmap of 27 selected genes of integrative MixOmics model. Tree-clustering was obtained according Ward's method. Conditioned (3T3L1A CM) and Control media (C) were shown in column annotation as red and blue, respectively. Similarly, the MCF-7 and MCF-7 TR cells were reported as green and black, respectively. **(B)** Horizontal bar plot visualizing the mean value of contribution in criterion assesses of each gene selected by discriminant analysis. The red and blue loadings represent the contribution of 3T3L1A CM and C, respectively, as final outcome of interest.

Gene ontology analysis identified “negative regulation of IRE1-mediated unfolded protein response” and “PERK-mediated unfolded protein response” as the first enriched ontology (Figure 4).

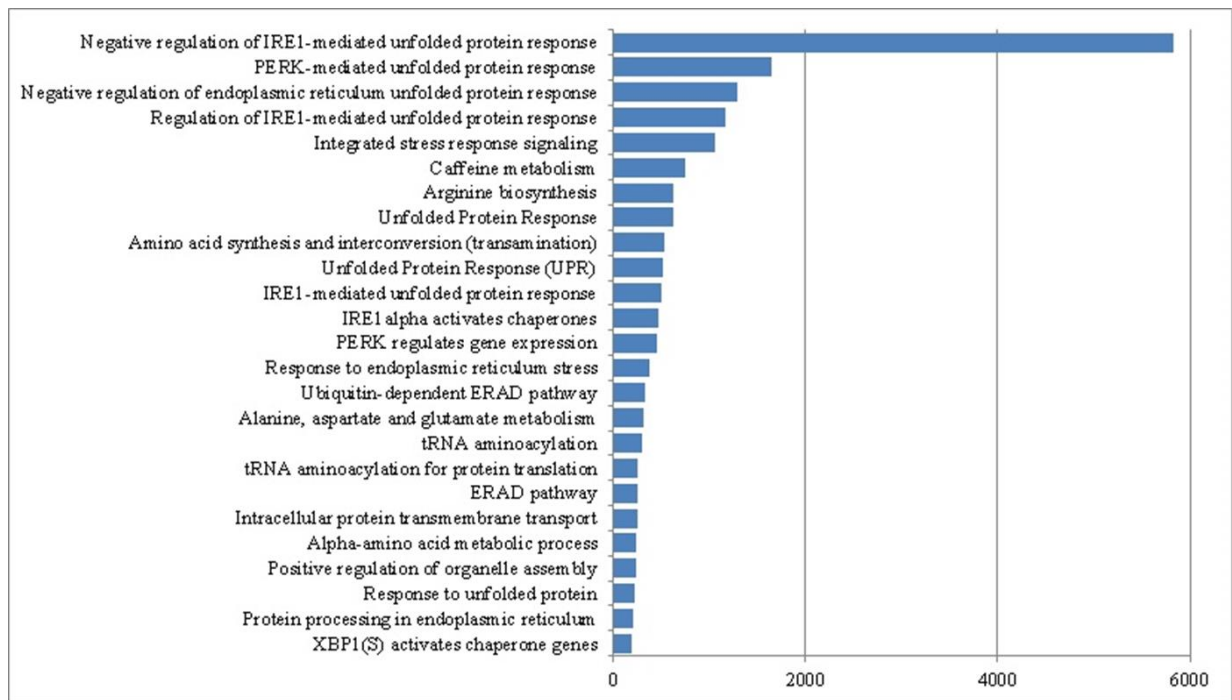


**Figure 4.** Gene ontology of 27 selected genes in common between MCF-7 and MCF-7 TR cells.

Finally, predictive functional analysis through Metacore allow us to generate a network, utilizing “shortest path” in which 100% of experimental factors were included. Network central hub were COUP-TFII, GRP78, CBX4, TXNIP and Ajuba, as evidenced in **Figure 5**.

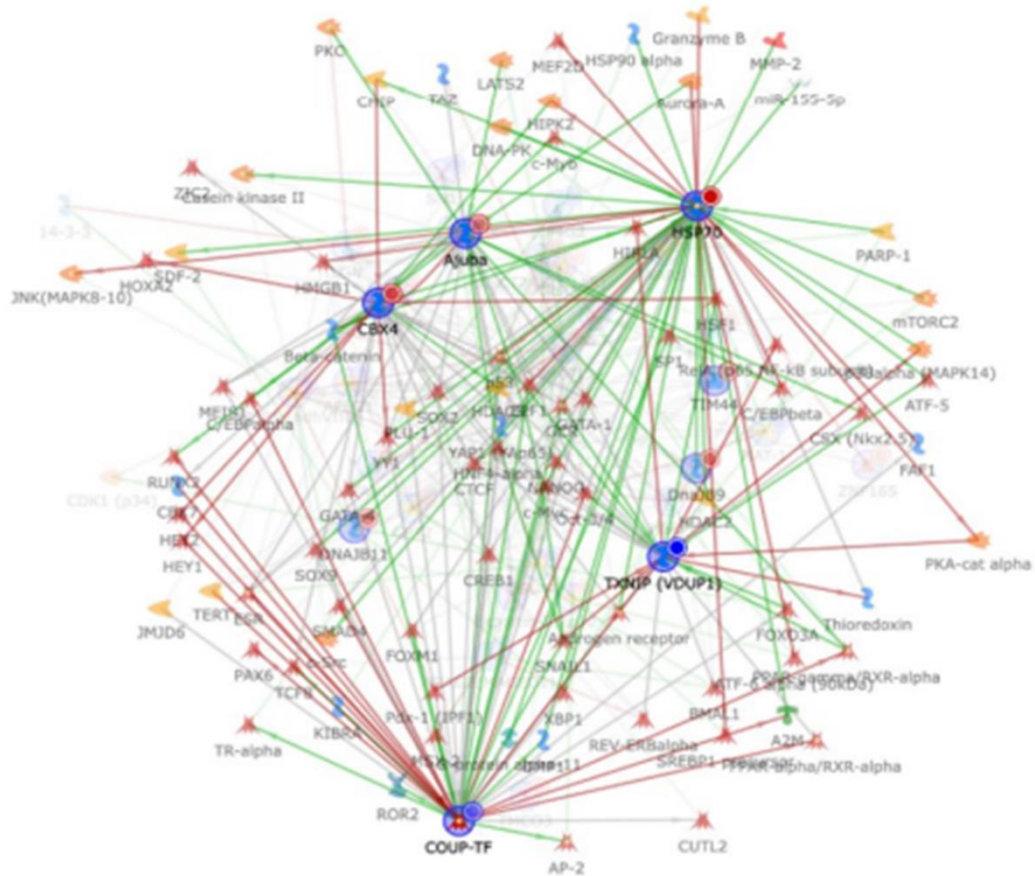


**Figure 5.** Direct interaction network (DIN) of 27 selected genes differentially expressed between MCF-7 and MCF-7 TR cells. The type and the direction of protein interconnection are indicated by edge color and arrowheads.

Interestingly, among these 27 genes, the most commonly gene down-regulated after exposure to 3T3L1A CM in both MCF-7 and MCF-7 TR cells was the Thioredoxin-interacting protein (TXNIP) (Table 3), a tumor suppressor gene participating in the metabolic reprogramming and oxidative stress in various solid cancers, particularly inhibiting or by limiting the bioavailability of the thioredoxin (TRX, TXN) system [83,84]. Furthermore, it was found that TXNIP is induced by ER stress through IRE-1 and PERK [85,86], the most enriched ontology found in our gene ontology analysis.

**Table 3.** Gene expression profile of the 27 selected genes.

Gene name	Gene symbol	Fold Change (FC) WT CM/WT	Padj WT CM/WT	Fold Change (FC) TR CM/TR	padj TR CM/TR
Thioredoxin-interacting protein	TXNIP	-21.20	6.69E-44	-5.13	1.78E-54
Ajuba LIM Protein	Ajuba	3.37	1.50E-81	2.38	2.26E-09
Chromobox 4	CBX4	2.55	5.84E-84	1.7	4.94E-08
DnaJ Heat Shock Protein Family (Hsp40) Member B11	DNAJB11	3.5	5.84E-98	1.5	2.10E-05
DnaJ Heat Shock Protein Family (Hsp40) Member B9	DNAJB9	2.96	4.22E-78	1.79	7.88E-07
G3BP Stress Granule Assembly Factor 1	G3BP1	-1.4	2.37E-20	-1.27	9.40E-03
Glutamate-Ammonia Ligase	GLUL	-1.99	5.59E-74	-1.38	5.24E-04
G Protein Signaling Modulator 2	GPSM2	2.3	3.52E-34	1.16	1.34E-01
Glutamic--Pyruvic Transaminase 2	GPT2	3.2	1.29E-112	1.99	4.92E-11
Homocysteine Inducible ER Protein With Ubiquitin Like Domain 1	HERPUD1	3.18	1.23E-177	2.23	8.59E-10
Heat Shock Protein Family A (Hsp70) Member 5	HSPA5	6.59	0.00E+00	2.16	2.52E-15
Isoleucyl-tRNA Synthetase 1	IARS1	3.13	2.54E-258	1.43	2.47E-04
Potassium Voltage-Gated Channel Subfamily E Regulatory Subunit 4	KCNE4	15.8	2.17E-62	3.12	1.13E-05
MAGE Family Member D1	MAGED1	-2.08	3.29E-54	-1.2	7.04E-02
Misato Mitochondrial Distribution And Morphology Regulator 1	MSTO1	3.46	1.90E-55	1.14	2.63E-01
N-Acetyltransferase 1 Nuclear Receptor Subfamily 2 Group F Member 2	NAT1	-2.88	1.40E-16	-1.19	1.92E-01
Protein Disulfide Isomerase Family A Member 4	NR2F2	-2.04	5.42E-79	-1.12	2.44E-01
Solute Carrier Family 1 Member 5	PDIA4	3.16	1.10E-209	1.3	6.28E-03
Striated Muscle Enriched Protein Kinase Translocase Of Inner Mitochondrial Membrane 44	SLC1A5	2.27	3.62E-138	1.43	6.31E-05
Transmembrane And Coiled-Coil Domains 3	SPEG	-2.20	6.05E-07	-2.05	2.35E-04
Tryptophanyl-tRNA Synthetase 1	TIMM44	2.05	5.38E-26	1.52	1.57E-04
Exportin For TRNA	TMCO3	1.74	1.03E-28	1.22	6.87E-02
Zinc Finger AN1-Type Containing 3	WARS1	5.48	0.00E+00	1.88	9.31E-12
Zinc Finger Protein 165	XPOT	4.12	0.00E+00	1.89	9.26E-10
Tryptophanyl-tRNA Synthetase 1	ZFAND3	1.7	4.09E-41	1.18	8.36E-02
	ZNF165	3.7	1.74E-24	1.47	2.35E-02
	WARS1	5.48	0.00E+00	1.88	9.31E-12

Thus, to validate the TXNIP gene expression identified by RNAseq, we first performed qRT-PCR in both cell lines after 3T3L1A CM exposure (**Figure 6A**). Our results demonstrated lower TXNIP mRNA levels in MCF-7 TR compared to MCF-7 cells. In addition, BC cells treated with CM exhibited a significant reduction of TXNIP expression, especially in MCF-7 TR cells. In line with these results, a decreased TXNIP transcriptional activity was observed in cells treated with 3T3L1A CM, as evidenced by luciferase reporter gene assays (**Figure 6B**). TXNIP protein expression has also been found to be down-regulated after exposure to 3T3L1A CM in both cell lines (**Figure 6C**). Moreover, TRX activity, which is negatively regulated by TXNIP, was increased by CM in MCF-7 cells and at a higher rate in MCF-7 TR cells (**Figure 6D**). Collectively, our data strongly suggest that 3T3L1A CM may impact

transcriptional machinery as well as protein pattern and activity of TXNIP, particularly in endocrine resistance setting.

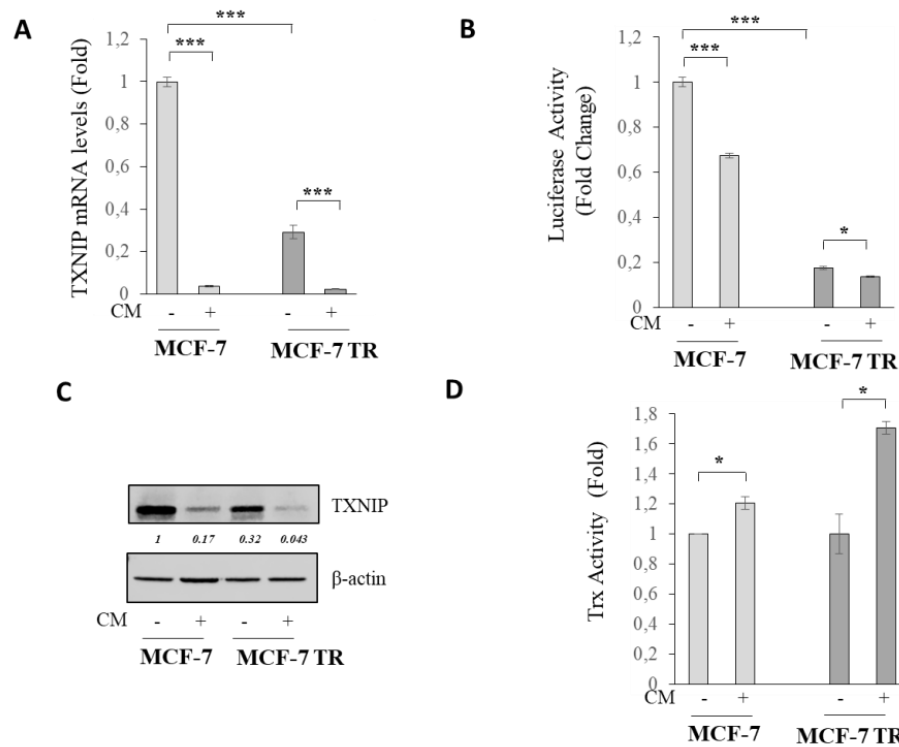


**Figure 6.** 3T3L1A CM reduces the expression and activity of TXNIP in MCF-7 and MCF-7 TR cells. **(A)** Real-time RT-PCR for TXNIP in MCF-7 and MCF-7 TR cells treated (+) or not (-) for 48h with 3T3L1A CM. **(B)** Transiently transfection with pGL3B-1081-Luc reporter constructs in MCF-7 and MCF-7 TR cells. After transfection, cells were treated as indicated for 24h. **(C)** Immunoblotting showing TXNIP protein expression in MCF-7 and MCF-7 TR cells treated as indicated for 48h.  $\beta$ -actin was used as a control for equal loading and transfer. **(D)** TRX activity in cells treated as indicated for 48h. The histograms represent the means  $\pm$  SEM of three separate experiments. \* $p < 0.05$ ; \*\*\* $p < 0.0005$ .

### TXNIP re-expression reverses 3T3L1A CM-mediated effects in MCF-7 and MCF-7 TR BC cells.

In order to assess the role of TXNIP expression in tumor cell/adipocyte interaction, we evaluate whether restoring TXNIP expression by pharmacological and genetic approaches may reverse adipocyte-induced effects. Thus, we used the following drugs that were shown to re-express TXNIP in BC cells (*Zhou et al., 2013*): i) Suberoylanilide hydroxamic acid (Saha,

Vorinostat), an inhibitor of class I and II of histone deacetylases (HDI) approved by food and drug administration (FDA) for the treatment of cutaneous T-cell lymphoma, and ii) 3-Deazaneplanocin A (DZNep), a histone methyltransferase EZH2, approved by FDA in hematological malignancies. As shown in **Figure 7A**, SAHA and DZNep were able to abrogate CM-mediated reduction of TXNIP expression in MCF-7 and MCF-7 TR cells in a dose-dependent manner. Concomitantly with TXNIP re-expression, SAHA and DZNep significantly reversed the effects of CM on anchorage-independent proliferation (**Figure 7B**) and migration (**Figure 7C**) in both cell lines. We then stably overexpressed TXNIP in MCF-7 and MCF-7 TR cells using lentivirus vector system with c-myc expression tag. To confirm the correct overexpression, we evaluated TXNIP protein expression in empty vector (c) and in MCF-7 and MCF-7 TR cells overexpressing TXNIP (o.e.). The *upper panel* of **Figure 7D** showed an endogenous TXNIP band (~43,7 kDa), and the exogenous TXNIP (myc-tagged, ~60 kDa). Overexpression was further confirmed by using myc antibody in protein extracts from TXNIP-o.e. cells (**Figure 7D**, *lower panel*). We then used these experimental models to corroborate the specific role of TXNIP in MCF-7 and MCF-7 TR cells before and after exposure to 3T3L1A CM. In line with the well-known role of TXNIP as a tumor suppressor gene (*Chen et al., 2020*), the lentivirus overexpression of TXNIP reduced the number of colonies and the number of migrated cells. Importantly, TXNIP o.e. prevented the 3T3L1A CM-induced proliferation and migration in both cell lines (**Figure 7E,F**). It's worth observing that these effects were amplified in MCF-7 TR TXNIP o.e. cells. These results may suggest that TXNIP activity is required for controlling proliferation and migration process induced by mature adipocyte secretoma in malignant cells, particularly in Tamoxifen-resistant cells.

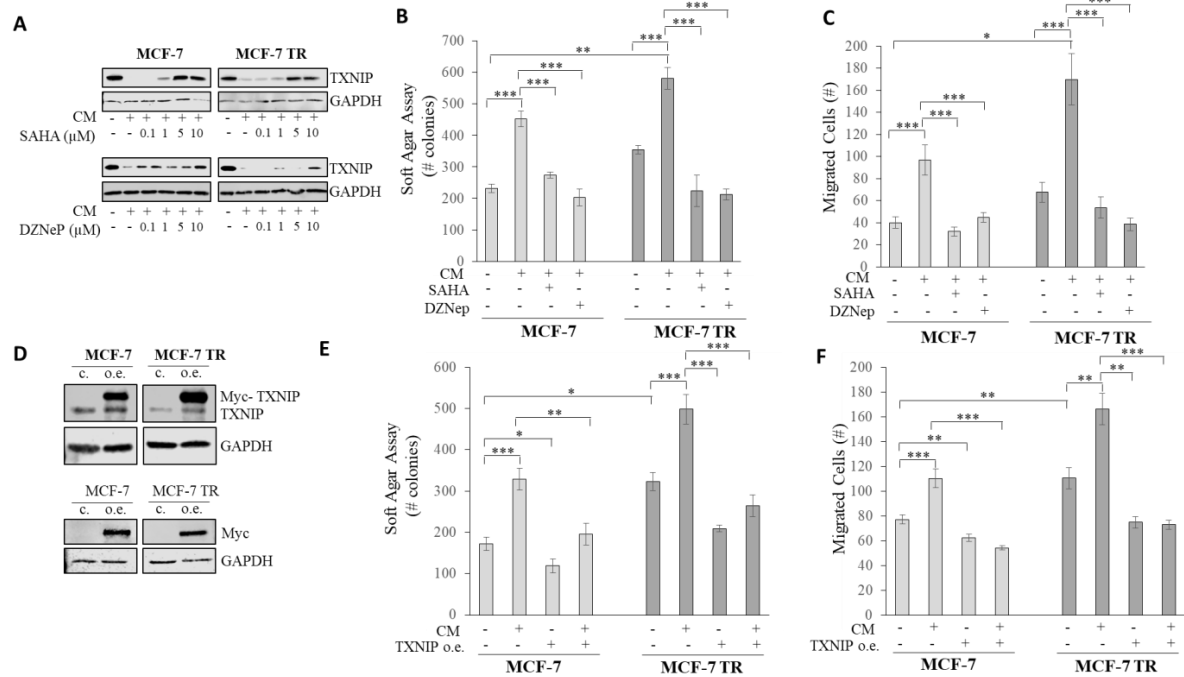


**Figure 7. Restoring TXNIP expression reverses 3T3L1A CM effects on MCF-7 and MCF-7 TR BC cells.** Immunoblotting showing TXNIP protein expression in MCF-7 and MCF-7 TR cells treated (+) or not (-) with 3T3L1A CM and 0.1, 1, 5, 10 μM Saha and DZNeP for 48h. GAPDH was used as a control for equal loading and transfer. **(B)** Soft agar growth assays in MCF-7 and MCF-7 TR cells treated (+) or not (-) with CM alone or in combination with 5 μM SAHA or 10 μM DZNeP. After 14 days of growth, colonies  $\geq 50$  μm were counted. The bar charts represent the mean  $\pm$  SEM of three separate experiments. **(C)** Boyden chamber transmigration in cells treated as indicated for 5h. The migrated/invaded cells were DAPI-stained, counted, and images were captured at 10 $\times$  magnification. The bar charts represent the mean of the migrated and invaded cells  $\pm$  SEM. **(D)** Immunoblotting showing TXNIP protein expression (*upper panel*) and Myc (*lower panel*) in MCF-7 and MCF-7 TR cells transduced with lenti ORF particles, Txnip (Myc-DDK-tagged) (o.e.) or empty vector (c.). GAPDH was used as a control for equal loading and transfer. **(E)** Soft agar growth assays in c. and TXNIP o.e. cells treated (+) or not (-) with CM. After 14 days of growth, colonies  $\geq 50$  μm were counted. The bar charts represent the mean  $\pm$  SEM of three separate experiments. **(F)** Boyden chamber transmigration in c. and TXNIP o.e. cells treated as indicated for 5h. The migrated cells were DAPI-stained, counted, and images were captured at 10 $\times$  magnification. The bar charts represent the mean of the migrated cells  $\pm$  SEM. \* $p < 0.05$ ; \*\* $p < 0.005$ ; \*\*\* $p < 0.001$ .

## Role of IGF1/TXNIP axis in adipocyte-induced Tamoxifen resistance

Recently, it has been demonstrated that TXNIP gene expression is negatively regulated by IGF-1 [87]. On the other hand, IGF-1 is widely secreted by adipocytes and is it has been widely shown to contribute to obesity-associated BC progression and endocrine resistance (*review in Barone et al., 2022*). Thus, we investigated whether IGF1/TXNIP axis may have a

role in CM-mediated described results. To this aim, co-culture experiments between MCF-7 or MCF-7 TR cells and 3T3L1A CM in the presence or not of IGF-1R inhibitor (GSK1838705A) and the IGF-1R downstream inhibitor (mTOR inhibitor Everolimus) were performed. First, we evaluated the effects of GSK1838705A and Everolimus alone and in combination on TXNIP expression and found that both drugs were able to reverse the reduction of TXNIP expression induced by CM expression (**Figure 8A**). Combined treatments were more effecting in restoring TXNIP expression. As a positive control, we used the IGF-1 treatment, and as previously demonstrated in other cell lines (*Nagaraja et al., 2018*), an important decrease of TXNIP expression was observed in MCF-7 or MCF-7 TR cells. Moreover, the already established increase in anchorage-independent growth and migration induced by 3T3L1A CM was reduced in the presence of GSK1838705A and Everolimus. The combined treatment reversed CM-mediated proliferation (**Figure 8B**) and migration (**Figure 8C**) at a higher extent. These data suggest a key role of IGF-1R/TXNIP axis in adipocyte-derived CM effects, highlighting how targeting this signaling could be the avenues to harness in endocrine-resistant settings under obesity conditions.

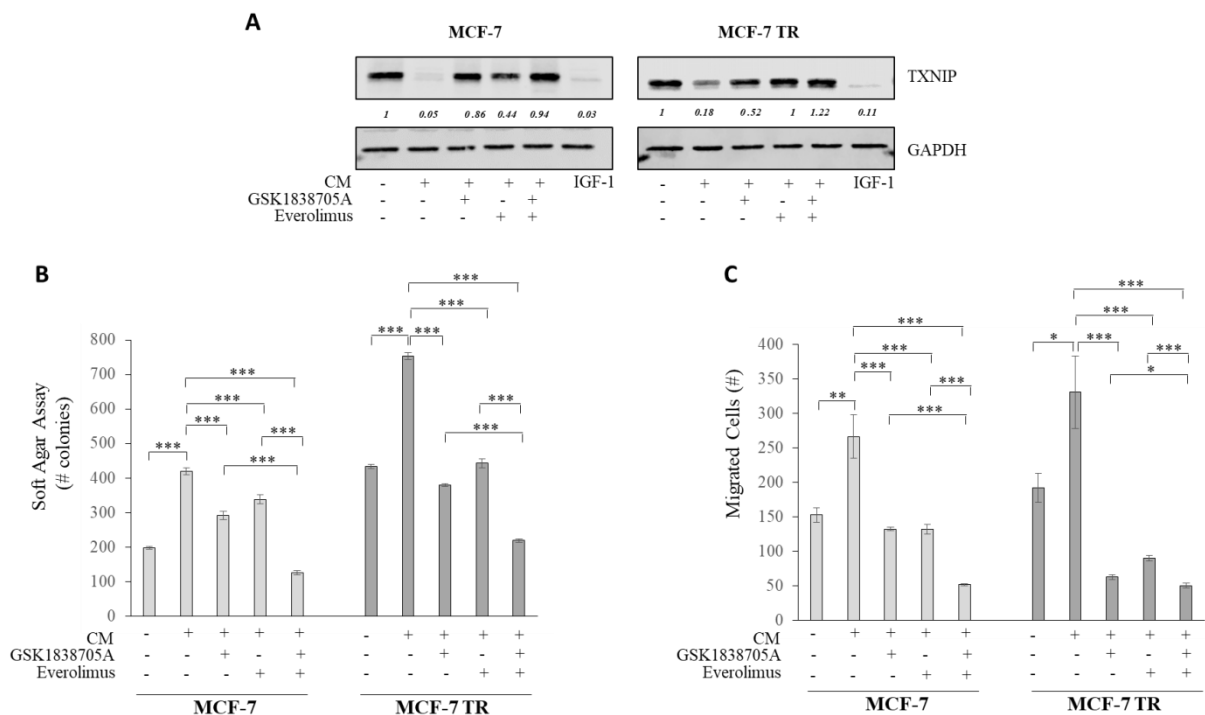


**Figure 8. IGF-1R signaling inhibitors reverses 3T3L1A CM effects on TXNIP expression, anchorage-independent growth and migration of MCF-7 and MCF-7 TR BC cells. (A)** Immunoblotting showing TXNIP protein expression in MCF-7 and MCF-7 TR cells treated (+) or not (-) with IGF-1 and CM alone or in combination

with 1  $\mu$ M of GSK1838705A or 1 nM Everolimus for 48h. GAPDH was used as a control for equal loading and transfer. **(B)** Soft agar growth assays in MCF-7 and MCF-7 TR cells treated as indicated. After 14 days of growth, colonies  $\geq 50$   $\mu$ m were counted. The bar charts represent the mean  $\pm$  SEM of three separate experiments. **(C)** Boyden chamber transmigration in cells treated as indicated for 5h. The migrated cells were DAPI-stained, counted, and images were captured at 10 $\times$  magnification. The bar charts represent the mean of the migrated cells  $\pm$  SEM. \* $p < 0.05$ ; \*\* $p < 0.005$ ; \*\*\* $p < 0.0005$ .

## IGF-1/TXNIP axis and adipocyte-induced Tamoxifen resistance in obesity experimental models

Based on these results, we wondered if the obese setting may reasonably give major emphasis to the important role of stromal adipocytes on endocrine therapy resistant BC cells. To this aim, we used an *in vitro* model of obese adipocyte (Ob) obtained from mature adipocytes (3T3L1A) maintained with basal medium supplemented with 1 mM of a 1:2:1 palmitate (C16:0), oleate (C18:1), and linoleate (C18:2) for 24 h. Obese adipocytes (3T3L1A Ob), characterized by phase contrast microscopy (**Figure 9A – upper panel**), and Red Oil O (**Figure 9A – lower panel**), displayed an hypertrophic and hyperplastic phenotype compared to 3T3L1A indicated as “N”. The higher amount of neutral lipids in obese adipocytes (3T3L1A Ob) compared to normal (3T3L1A N) were confirmed by Red Oil dye elution and measurement (**Figure 9B**). Real time RT-PCR analysis also evidenced an up-regulation of specific adipocyte markers, such as *AdipoQ*, *OB*, *FABP4*, and *PPARG* in 3T3L1A Ob compared to 3T3L1A N (**Figure 9C**).

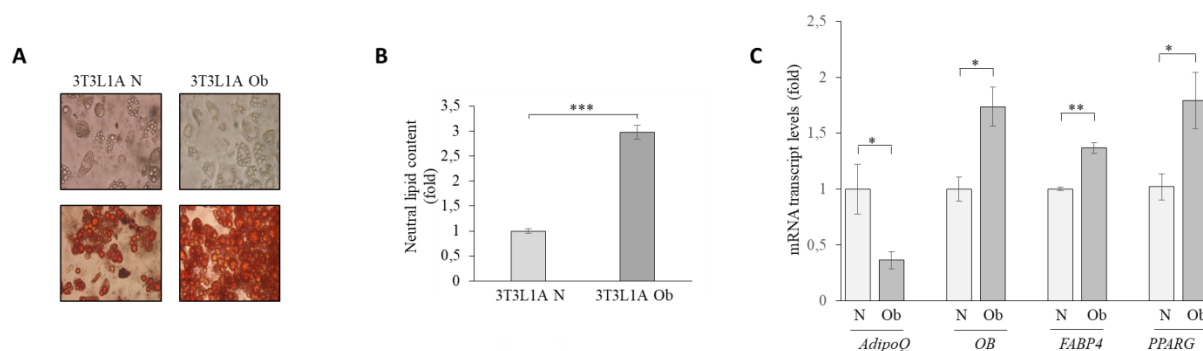


**Figure 9. Characterization of 3T3L1 obese mature adipocyte (3T3L1A Ob).** **(A)** The representative phase contrast (*upper panel*) and oil red O staining (*lower panel*) images of 3T3L1 cells at the normal adipocyte (3T3L1A N) and obese adipocyte (3T3L1A Ob) stages (40X); **(B)** Neutral lipid lipid content of oil red O staining of 3T3L1A N and 3T3L1A Ob were quantified eluting red O dye with isopropanol and then measuring optical density (OD) at 490 nm using a spectrophotometer; **(C)** Real time RT-PCR for different adipocyte markers such as *AdipoQ*

(Adiponectin C1Q), OB (Leptin), FABP4 (Fatty Acid Binding Protein 4), PPAR $\gamma$  (Peroxisome Proliferator-Activated Receptor gamma), Ob (Leptin). Mean  $\pm$  SEM.

We used this experimental model to set up co-cultures with MCF-7 TR cells and to evaluate whether targeting TXNIP/IGF-1 may be useful to counteract obesity impact on BC hormone resistance. We found that TXNIP mRNA levels (**Figure 10A**) and protein expression (**Figure 10B**) were reduced in higher extent in MCF-7 TR treated with 3T3L1A Ob CM compared to MCF-7 TR cells treated with 3T3L1A N CM. Moreover, the increase in the number of colonies (**Figure 10C**) and migrated cells (**Figure 10D**) was more evident upon exposure to 3T3L1A Ob CM compared to 3T3L1A N CM. The treatment with SAHA or the IGF-1R inhibitor GSK1838705A significantly reduced the Ob-CM induced proliferation and migration in MCF-7 TR cells. This reduction was amplified upon combined drug treatment (**Figure 10C,D**). In line with these data, lentiviral overexpression of TXNIP significantly counteracted Ob-CM induced proliferation (**Figure 10E**) and migration (**Figure 10F**), further highlighting the role of TXNIP in adipocyte-induced Tamoxifen resistance.

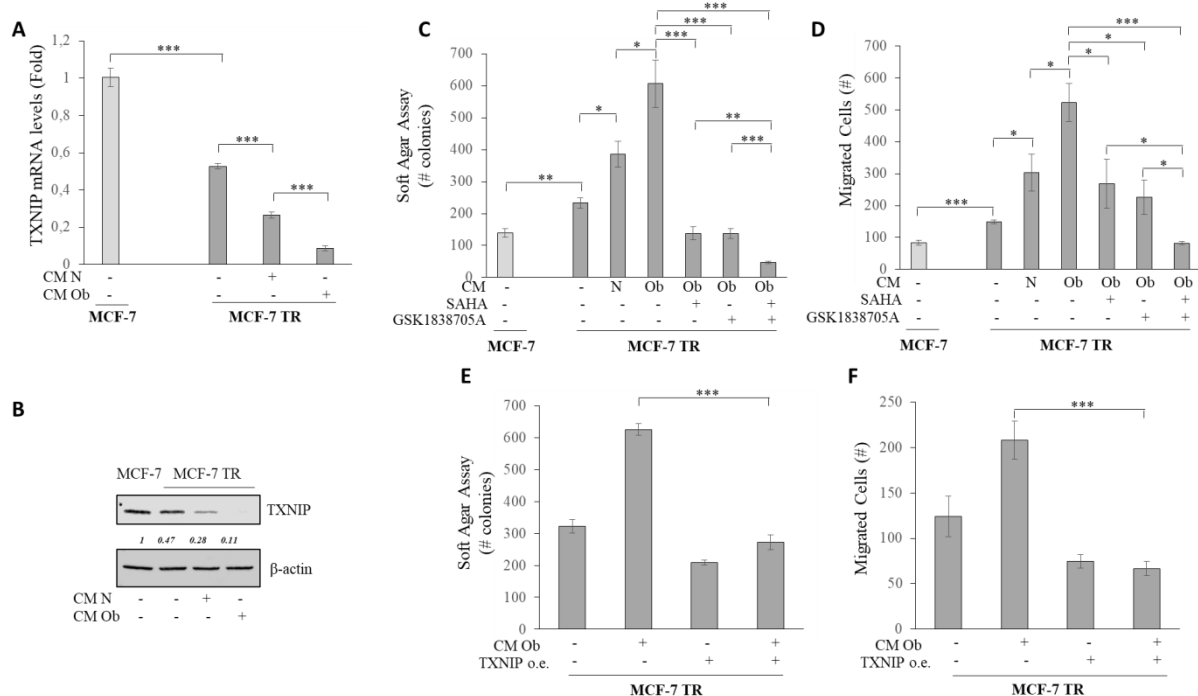


**Figure 10. Targeting IGF-1/TXNIP axis may counteract obesity-induced Tamoxifen resistance.** Real-time RT-PCR for TXNIP in MCF-7 and MCF-7 TR cells treated (+) or not (-) with 3T3L1A N CM and 3T3L1A Ob CM for 48h. The histograms represent the means  $\pm$  SEM of three separate experiments. **(B)** Immunoblotting showing

TXNIP protein expression in MCF-7 and MCF-7 TR cells treated as indicated for 48h.  $\beta$ -actin was used as a control for equal loading and transfer. **(C)** Soft agar growth assays in MCF-7 and MCF-7 TR cells treated with CM N and CM Ob alone or in combination with 5  $\mu$ M SAHA and/or 1  $\mu$ M GSK1838705A. After 14 days of growth, colonies  $\geq 50$   $\mu$ m were counted. The bar charts represent the mean  $\pm$  SEM of three separate experiments. **(D)** Boyden chamber transmigration in MCF-7 and MCF-7 TR cells treated as indicated for 5h. The migrated were DAPI-stained, counted, and images were captured at 10 $\times$  magnification. The bar charts represent the mean of the migrated cells  $\pm$  SEM. **(E)** Soft agar growth assays in MCF-7 treated (+) or not (+) with CM Ob and infected (+) or not (-) with lentiviral ORF particles overexpressing TXNIP (TXNIP o.e.). After 14 days of growth, colonies  $\geq 50$   $\mu$ m were counted. The bar charts represent the mean  $\pm$  SEM of three separate experiments. **(F)** Boyden chamber transmigration in cells treated as indicated for 5h. The migrated/invaded cells were DAPI-stained, counted, and images were captured at 10 $\times$  magnification. The bar charts represent the mean of the migrated and invaded cells  $\pm$  SEM. \* $p < 0.05$ ; \*\* $p < 0.005$ ; \*\*\* $p < 0.0005$ .

### **The involvement of IGF-1/TXNIP axis in AI-resistant BC cells**

To extend this results, 3T3L1A Ob CM was used in co-culture experiments with two additional models of endocrine therapy resistance: i) long-term estrogen deprived (LTED) BC cells; ii) Anastrozole-resistant (AnaR) BC cells. As expected, LTED and AnaR cells displayed lower TXNIP mRNA levels (**Figure 11A,E**) and protein expression (**Figure 11B,F**) compared parental sensitive BC cells. As observed in MCF-7 TR cells, 3T3L1A L CM was able to reduce TXNIP expression and this reduction was amplified after exposure to 3T3L1A Ob CM in both LTED (**Figure 11A,B**) and AnaR (**Figure 11E,F**) BC cells. To evaluate the role of IGF-1/TXNIP axis, soft agar and migration assays were assessed in LTED and AnaR cells treated with 3T3L1A L CM, 3T3L1A Ob CM, in the presence or not of SAHA, GSK1838705A or the combined treatments. Our results indicated that SAHA and GSK1838705A significantly reduced the 3T3L1A Ob CM induced increase in the number of colonies and migrated cells in both LTED (**Figure 11C,D**) and AnaR (**Figure 11G,H**) cells. Importantly, combined treatment resulted in a higher inhibition of 3T3L1A Ob CM effects, underlying that IGF-1/TXNIP axis may be a common player in mediating adipocyte/tumor cell interaction in both Tamoxifen- and AI-resistance.

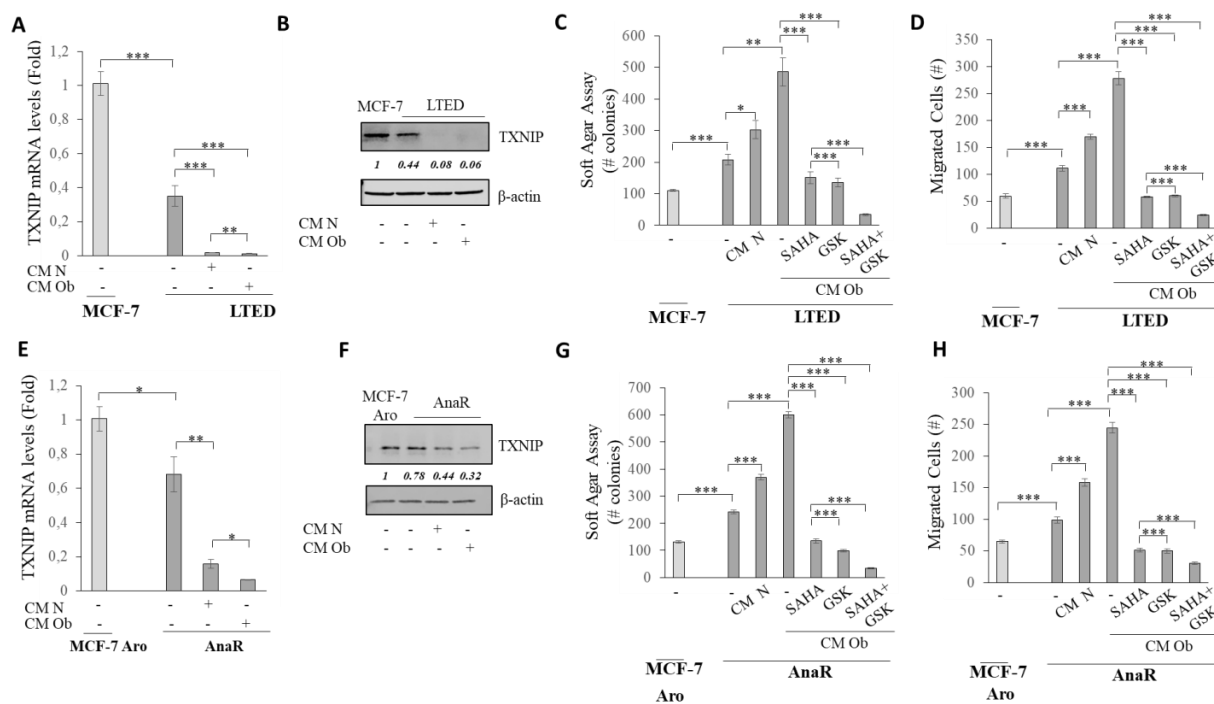


**Figure 11. Targeting IGF-1/TXNIP axis counteracts obesity-induced AI-resistance.** (A) Real-time RT-PCR for TXNIP mRNA levels in MCF-7 and LTED BC cells treated or not (-) for 48h with 3T3L1A L CM and 3T3L1A Ob CM. The histograms represent the means  $\pm$  SEM of three separate experiments. (B) Immunoblotting showing TXNIP protein expression in MCF-7 and MCF-7 LTED cells treated (+) or not (-) with CM L and CM Ob for 48h.  $\beta$ -actin was used as a control for equal loading and transfer. (C) Soft agar growth assays in MCF-7 and LTED cells treated (+) or not (-) with CM L and CM Ob alone or in combination with 5  $\mu$ M SAHA and/or 1  $\mu$ M GSK1838705A. After 14 days of growth, colonies  $\geq$ 50  $\mu$ m were counted. The bar charts represent the mean  $\pm$  SEM of three separate experiments. (D) Boyden chamber transmigration in MCF-7 and LTED cells treated as indicated for 5h. The migrated cells were DAPI-stained, counted, and images were captured at 10 $\times$  magnification. The bar charts represent the mean of the migrated cells  $\pm$  SEM. (E) Real time RT-PCR for TXNIP mRNA levels in MCF-7 Aro and AnaR cells treated or not (-) for 48h with CM L and CM Ob. The histograms represent the means  $\pm$  SEM of three separate experiments. (F) Immunoblotting showing TXNIP protein expression in MCF-7 Aro and MCF-7 AnaR cells treated as indicated for 48 h.  $\beta$ -actin was used as a control for equal loading and transfer. (G) Soft agar growth assays in MCF-7 Aro and MCF-7 AnaR cells treated with CM L and CM Ob alone or in combination with 5  $\mu$ M SAHA and/or 1  $\mu$ M GSK1838705A. After 14 days of growth, colonies  $\geq$ 50  $\mu$ m were counted. The bar charts represent the mean  $\pm$  SEM of three separate experiments. (H) Boyden chamber transmigration in MCF-7 Aro and MCF-7 AnaR cells treated as indicated for 5h. The migrated/invaded cells were DAPI-stained, counted, and images were captured at 10 $\times$  magnification. The bar charts represent the mean of the migrated and invaded cells  $\pm$  SEM. \* $p$ <0.05; \*\* $p$ <0.005; \*\*\* $p$ <0.0005.

### IGF-1/TXNIP axis and Patient-Derived Organoids (PDOs)

Results were then validated by using Patient-Derived Organoids (PDOs) as the 'ex vivo' therapeutic platform to clarify the effectiveness of IGF-1/TXNIP axis inhibition in tumor progression in obese setting. Indeed, it has been demonstrated that PDO-based drug screening has a positive predictive value of 88% and a negative predictive value of 100%, particularly in prediction the therapy response 'in vivo' (Vlachogiannis *et al.*, 2018), owing to the well-maintained characteristics of the original tumors in PDOs, including intratumoral heterogeneity, histological phenotypes, genomic alterations, transcriptome patterns, and different response to antineoplastic drugs (Sachs *et al.*, 2018). Thus, we first collected MBC fluid specimens derived from pleural effusions and ascites fluid of overweight and obese metastatic endocrine-resistant BC patients, who underwent drains for their palliative care, and PDOs (BB329T1N - BMI=25.7; BB381T1N - BMI=25.1, BB388T1N - BMI=39.7) were generated in order to evaluate the different viability and growth rate in the presence or not of SAHA, GSK1838705A and the combined treatments (**Figure 12A**). We found that BB329T1N, BB381T1N, BB388T1N organoid viability was reduced with SAHA or GSK1838705A monotherapy and was further suppressed with the combined treatment (**Figure 12B**). Similarly, organoid growth was significantly inhibited in the presence of SAHA or GSK, and this inhibition was stronger in the presence of combined treatment (**Figure 12C**). Therefore, the role of IGF-1/TXNIP axis in obesity-mediate endocrine resistance was also confirmed in an 'ex vivo' tumor model.

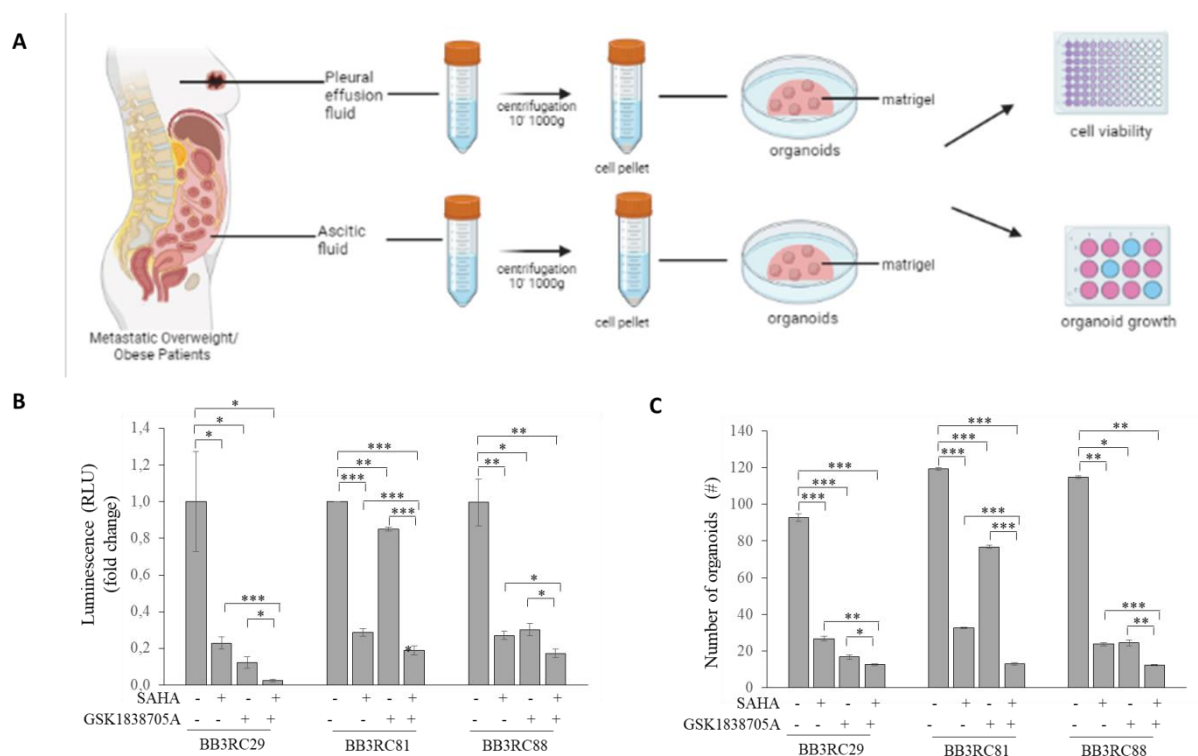


**Figure 12. Targeting IGF-1/TXNIP reduce tumor proliferation in overweight and obese patient-derived organoids (PDOs).** (A) Flowchart of PDOs derived from overweight and obese metastatic BC patients. (B) Relative luminescence of PDOs cells treated (+) or not (-) with of 5  $\mu$ M SAHA and/or 1  $\mu$ M GSK1838705A. Spheroids were cultured for 9 days before their luminescence was measured. (C) Number of organoids treated (+) or not (-) with 5  $\mu$ M SAHA and/or 1  $\mu$ M GSK1838705A. Organoids were counted after 12 days. Data represented as mean  $\pm$  SEM. \* $p$ <0.05; \*\* $p$ <0.005; \*\*\* $p$ <0.0005.

### IGF-1/TXNIP signature and clinical outcomes in BC patients.

To evaluate the clinical significance of IGF-1/TXNIP expression in human breast tumors, we conducted retrospective analyses to investigate whether high IGF-1/low TXNIP co-expression may be associated with BC patient survival. We found that high IGF-1 and low TXNIP signature correlated with a shorter recurrence free survival (RFS) in ER+ BC patients treated with endocrine therapies, with long-rank  $p$  value and hazard ratio (HR) of 0.00054 and 2,55, respectively, in the TGCA dataset (**Figure 13A**). This result was subsequently validated in other two independent datasets with a long-rank  $p$  value 0.0015 and HR 1.46 (GEO dataset, **Figure 13B**) and  $p$  value 0.00034 and HR 1.86 (Metabric dataset, **Figure 13C**). On the basis of these observations, it is evident that the impact of IGF-1 and TXNIP deserve further attention in a large cohort of BC patients, especially in relation to patients' BMI.

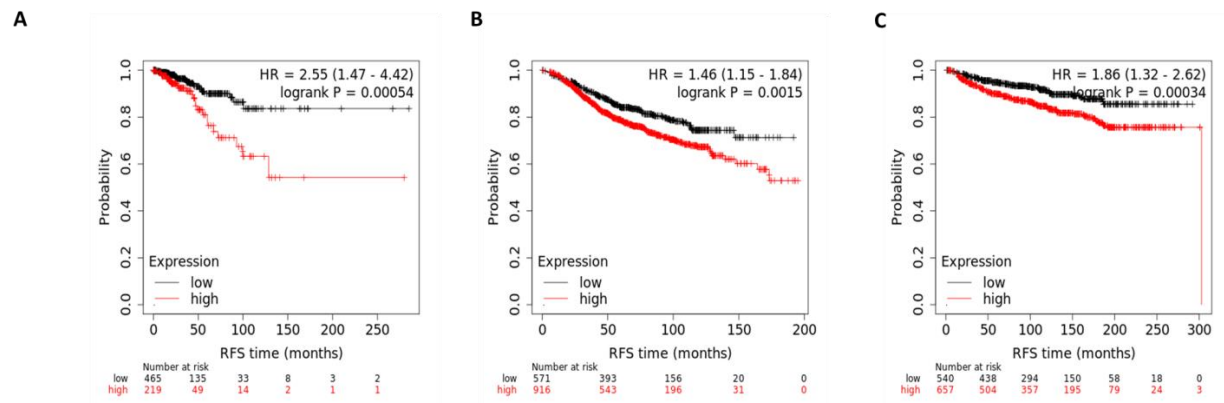


**Figure 13. High IGF-1/low TXNIP expression and clinical outcomes in BC patients treated with endocrine therapy.** Kaplan–Meier survival analysis relating levels and recurrence free survival (RFS) in TGCA (A), GEO (B), and Metabric (C) datasets, involving endocrine therapy-treated ER+ BC patients.

## Discussion

Endocrine therapy (e.g Tamoxifen, Anastrozole, Letrozole) is the most effective and widely used therapy in patients with ER+ BC. However, the major concern is that resistance to therapy eventually occurs in a large number of patients. Among the intrinsic factors leading to this acquisition of endocrine resistance activating point mutations that clustered in ligand binding domain (LBD) of ESR1 gene harboring mainly at the residues D538G, Y537S, Y537N elicit ligand-independent constitutive activation of ER contribute to resistance to aromatase inhibitors and relative resistance to Tamoxifen and Fulvestrant. In the present study we focused our attention on the most recurrent ESR1m, Y537S (YS1), associated with well documented endocrine resistance, and the interaction with one of the major component of TME, such as fibroblasts (**Aim 1**).

Our data, by using co-culture experiments, demonstrated how ESR1m secretome may induce a higher proliferative and migratory effects in normal fibroblasts (NFs) and cancer associated fibroblasts (CAFs). Interestingly, CAFs displayed higher levels of CAF marker after exposure of ESR1m secretome. On the other hands, CAFs and NFs secretome showed to induce an increase proliferation and migration in MCF-7 CRISPR P and MCF-7 CRISPR YS1, but in higher extent in mutant cells. Transcriptome analysis between MCF-7 CRISPR P and MCF-7 CRISPR YS1 unraveled a molecular signature of different cellular pathway, highlighting IGF-1R as the highly expressed gene in mutant cells. It's worth to mention how mutant BC cells overexpressing IGF-1/IGF-1R signaling, secrete IGF-1 in a significantly higher amount with the respect of parental one. Thus, it's reasonable to speculate how the enhanced growth rate of mutant cells with the respect to parental one may be sustained by the short autocrine loop IGF-1/IGF-1R. However, IGF-1 is also secreted by fibroblasts. Interestingly, CAFs display a higher constitutive activation of IGF-1R signalling compared to NFs. Thus, IGF-1 play autocrine effect on both mutant as well as in CAFs, and at the same time is the shuttle molecule sustaining in paracrine and bidirectional way mutant cells and CAFs growth.

It's worth to remark that the use of IGF-1/IGF-1R inhibitor such as GSK1838705A is able to drastically reverse the stimulatory effect induced on mutant cells proliferation and motility by the exposure CAFs. At the same time, the stimulatory effect induced by mutant cells on CAFs proliferation and motility has no longer noticeable. Thus, the inhibitory drug of IGF-

1/IGF-1R signalling, such as GSK1838705A, appear to be promising in disconnecting functional interaction between mutant tumor cell and the TME.

Obesity represents a heavyweight player being a complex physiologic state associated with multiple molecular changes capable of modulating the behaviour of BC cells as well as its surrounding TME. Excess of body weight has been linked with poor prognosis in women diagnosed with early stage of BC. Obesity indicate chronic inflammation promoted by adipose tissue dysfunction induced by an increase in free radicals generation and subsequently promotes oxidative stress, thus preparing a microenvironment favourable to the tumor preferred in obese individuals. Interestingly, hypertrophic and hyperplastic adipocyte in an obese setting, has been correlated with resistance to therapy in BC [57]. In the second part of the present study we investigated how Tamoxifen resistance in BC may interact with another abundant component of the tumor stroma, the adipocytes (**Aim 2**).

It address how adipocyte secretoma work against Tamoxifen resistance responsiveness as demonstrated by the effect of adipocyte-derived conditioned medium (CM) in reducing BC cells sensitivity to tamoxifen in proliferation, motility and invasiveness. Interestingly, the growth, motility and invasiveness in tamoxifen resistant BC cells (MCF-7 TR) were dramatically increased after the exposure to adipocyte secretome. When we compared a transcriptome analysis performed in MCF-7 and MCF-7 TR BC cells both treated with adipocyte-derived CM, we identified a downregulation of TXNIP, but it appears drastically reduced in terms of protein content in MCF-7 TR. TXNIP is a 50-kDa protein that plays an important role in metabolic reprogramming, oxidative stress, cell proliferation and apoptosis through inhibition of the TRX (thioredoxin) system and its reduced expression has been associated with a worse prognosis in several types of tumors, including BC [83]. Particularly, TXNIP inhibits the antioxidative function of TRX, a thiol oxido-reductase which is the major regulator of cellular redox and protects from oxidative stress. This protein inhibits the antioxidant function of thioredoxin resulting in the accumulation of reactive oxygen species and cellular stress. Interestingly, restoring TXNIP expression by lentiviral and pharmacological (i.e. SAHA) approaches reversed the stimulatory effects of the adipocyte secretoma on cell growth and motility. Next, considering the role of IGF-1 in mediating the adverse effects of obesity in BC and its ability to down-regulate TXNIP protein expression in a different experimental model [87], we evaluated the involvement of IGF-1/TXNIP axis in mediating the cross-talk between adipocytes and BC cells in the context of endocrine

resistance. Particularly, we noticed how the inhibition of IGF-1R pathway by using specific inhibitors (i.e. GSK1838705A, Everolimus) counteracts the TXNIP reduction mediated by adipocyte secretome. This effect was particularly marked in MCF-7 TR cell line compared to the MCF-7 one. Based on these findings, we wondered whether obesity could reasonably place more emphasis on the role of adipocytes on endocrine therapy-resistant BC cells. In this regard, an “in vitro” model of obese adipocytes (Ob) was also assessed. Our results showed that TXNIP down-regulation, proliferation and motility were amplified upon treatment with Ob CM in MCF-7 TR cells and combined treatment with an IGF-1 inhibitor and SAHA abrogated Ob CM-mediated effects. These latter events were also shown in cells resistant to aromatase inhibitors aiming a common mechanism of obesity-mediated endocrine resistance. In order to clarify the efficacy of the inhibition of the IGF-1/TXNIP axis in tumor progression in obesity, we employed patient-derived organoids (PDOs) as an “ex vivo” experimental model. Samples derived from pleural effusions and ascites fluid from overweight and obese patients with metastatic BC undergoing drains for their palliative care were used and treated with SAHA, GSK1838705A and the combined treatments. PDO viability and growth assays showed a significant reduction in growth and vitality with SAHA or GSK1838705A monotherapy, further suppressed with combined treatments. Finally, Kaplan-Meier retrospective analyzes showed a lower recurrence-free survival (RFS) in patients with ER+ BC treated with endocrine therapy, which display a higher expression of IGF-1 and reduced TXNIP levels in three independent datasets. These data shed new light on adipocytes and mammary cancer cell crosstalk during Tamoxifen therapy, suggesting the possibility to target IGF-1/TXNIP axis to block this harmful connection, especially in endocrine-resistant settings.

## **Conclusion**

Our study highlights the functional importance of tumor-host cross-talk in impacting malignant cell behavior. A better understanding of the molecular mechanism underlying TME/BC cells crosstalk might offer novel biomarkers and potential targets (e.g. IGF-1R inhibitors, inhibitor of histone deacetylases) to be implemented in the adjuvant therapy for improving clinical care and reducing mortality from BC.

**References:**

1. Sung, H.; Ferlay, J.; Siegel, R.L.; Laversanne, M.; Soerjomataram, I.; Jemal, A.; Bray, F. Global Cancer Statistics 2020: GLOBOCAN Estimates of Incidence and Mortality Worldwide for 36 Cancers in 185 Countries. *CA Cancer J Clin* **2021**, *71*, 209-249, doi:10.3322/caac.21660.
2. Goldhirsch, A.; Winer, E.P.; Coates, A.S.; Gelber, R.D.; Piccart-Gebhart, M.; Thurlimann, B.; Senn, H.J.; Panel, m. Personalizing the treatment of women with early breast cancer: highlights of the St Gallen International Expert Consensus on the Primary Therapy of Early Breast Cancer 2013. *Ann Oncol* **2013**, *24*, 2206-2223, doi:10.1093/annonc/mdt303.
3. Hashmi, A.A.; Aijaz, S.; Khan, S.M.; Mahboob, R.; Irfan, M.; Zafar, N.I.; Nisar, M.; Siddiqui, M.; Edhi, M.M.; Faridi, N.; et al. Prognostic parameters of luminal A and luminal B intrinsic breast cancer subtypes of Pakistani patients. *World J Surg Oncol* **2018**, *16*, 1, doi:10.1186/s12957-017-1299-9.
4. Kennecke, H.; Yerushalmi, R.; Woods, R.; Cheang, M.C.; Voduc, D.; Speers, C.H.; Nielsen, T.O.; Gelmon, K. Metastatic behavior of breast cancer subtypes. *J Clin Oncol* **2010**, *28*, 3271-3277, doi:10.1200/JCO.2009.25.9820.
5. Guarneri, V.; Piacentini, F.; Ficarra, G.; Frassoldati, A.; D'Amico, R.; Giovannelli, S.; Maiorana, A.; Jovic, G.; Conte, P. A prognostic model based on nodal status and Ki-67 predicts the risk of recurrence and death in breast cancer patients with residual disease after preoperative chemotherapy. *Ann Oncol* **2009**, *20*, 1193-1198, doi:10.1093/annonc/mdn761.
6. Feng, Y.; Spezia, M.; Huang, S.; Yuan, C.; Zeng, Z.; Zhang, L.; Ji, X.; Liu, W.; Huang, B.; Luo, W.; et al. Breast cancer development and progression: Risk factors, cancer stem cells, signaling pathways, genomics, and molecular pathogenesis. *Genes Dis* **2018**, *5*, 77-106, doi:10.1016/j.gendis.2018.05.001.
7. Gabos, Z.; Sinha, R.; Hanson, J.; Chauhan, N.; Hugh, J.; Mackey, J.R.; Abdulkarim, B. Prognostic significance of human epidermal growth factor receptor positivity for the

- development of brain metastasis after newly diagnosed breast cancer. *J Clin Oncol* **2006**, *24*, 5658-5663, doi:10.1200/JCO.2006.07.0250.
8. Kumar, P.; Kuscü, C.; Dutta, A. Biogenesis and Function of Transfer RNA-Related Fragments (tRFs). *Trends Biochem Sci* **2016**, *41*, 679-689, doi:10.1016/j.tibs.2016.05.004.
  9. Waks, A.G.; Winer, E.P. Breast Cancer Treatment: A Review. *JAMA* **2019**, *321*, 288-300, doi:10.1001/jama.2018.19323.
  10. Pellegrino, B.; Hlavata, Z.; Migali, C.; De Silva, P.; Aiello, M.; Willard-Gallo, K.; Musolino, A.; Solinas, C. Luminal Breast Cancer: Risk of Recurrence and Tumor-Associated Immune Suppression. *Mol Diagn Ther* **2021**, *25*, 409-424, doi:10.1007/s40291-021-00525-7.
  11. Aggelis, V.; Johnston, S.R.D. Advances in Endocrine-Based Therapies for Estrogen Receptor-Positive Metastatic Breast Cancer. *Drugs* **2019**, *79*, 1849-1866, doi:10.1007/s40265-019-01208-8.
  12. Johnston, S.R.; Yeo, B. The optimal duration of adjuvant endocrine therapy for early stage breast cancer--with what drugs and for how long? *Curr Oncol Rep* **2014**, *16*, 358, doi:10.1007/s11912-013-0358-9.
  13. Patel, H.K.; Bihani, T. Selective estrogen receptor modulators (SERMs) and selective estrogen receptor degraders (SERDs) in cancer treatment. *Pharmacol Ther* **2018**, *186*, 1-24, doi:10.1016/j.pharmthera.2017.12.012.
  14. Cardoso, F.; Costa, A.; Senkus, E.; Aapro, M.; Andre, F.; Barrios, C.H.; Bergh, J.; Bhattacharyya, G.; Biganzoli, L.; Cardoso, M.J.; et al. 3rd ESO-ESMO International Consensus Guidelines for Advanced Breast Cancer (ABC 3). *Ann Oncol* **2017**, *28*, 3111, doi:10.1093/annonc/mdx036.
  15. Murphy, C.G.; Dickler, M.N. Endocrine resistance in hormone-responsive breast cancer: mechanisms and therapeutic strategies. *Endocr Relat Cancer* **2016**, *23*, R337-352, doi:10.1530/ERC-16-0121.
  16. Ghosh, M.; Naik, R.; Lingaraju, S.M.; Susheela, S.P.; Patil, S.; Srinivasachar, G.K.; Thungappa, S.C.; Murugan, K.; Jayappa, S.B.; Bhattacharjee, S.; et al. Landscape of clinically actionable mutations in breast cancer 'A cohort study'. *Transl Oncol* **2021**, *14*, 100877, doi:10.1016/j.tranon.2020.100877.

17. Brett, J.O.; Spring, L.M.; Bardia, A.; Wander, S.A. ESR1 mutation as an emerging clinical biomarker in metastatic hormone receptor-positive breast cancer. *Breast Cancer Res* **2021**, *23*, 85, doi:10.1186/s13058-021-01462-3.
18. Chandarlapaty, S.; Chen, D.; He, W.; Sung, P.; Samoila, A.; You, D.; Bhatt, T.; Patel, P.; Voi, M.; Gnant, M.; et al. Prevalence of ESR1 Mutations in Cell-Free DNA and Outcomes in Metastatic Breast Cancer: A Secondary Analysis of the BOLERO-2 Clinical Trial. *JAMA Oncol* **2016**, *2*, 1310-1315, doi:10.1001/jamaoncol.2016.1279.
19. Zhang, Q.X.; Borg, A.; Wolf, D.M.; Oesterreich, S.; Fuqua, S.A. An estrogen receptor mutant with strong hormone-independent activity from a metastatic breast cancer. *Cancer Res* **1997**, *57*, 1244-1249.
20. Dustin, D.; Gu, G.; Fuqua, S.A.W. ESR1 mutations in breast cancer. *Cancer* **2019**, *125*, 3714-3728, doi:10.1002/cncr.32345.
21. Barone, I.; Cui, Y.; Herynk, M.H.; Corona-Rodriguez, A.; Giordano, C.; Selever, J.; Beyer, A.; Ando, S.; Fuqua, S.A. Expression of the K303R estrogen receptor-alpha breast cancer mutation induces resistance to an aromatase inhibitor via addiction to the PI3K/Akt kinase pathway. *Cancer Res* **2009**, *69*, 4724-4732, doi:10.1158/0008-5472.CAN-08-4194.
22. Gelsomino, L.; Gu, G.; Rechoum, Y.; Beyer, A.R.; Pejerrey, S.M.; Tsimelzon, A.; Wang, T.; Huffman, K.; Ludlow, A.; Ando, S.; et al. ESR1 mutations affect anti-proliferative responses to tamoxifen through enhanced cross-talk with IGF signaling. *Breast Cancer Res Treat* **2016**, *157*, 253-265, doi:10.1007/s10549-016-3829-5.
23. Gelsomino, L.; Gu, G.; Rechoum, Y.; Beyer, A.R.; Pejerrey, S.M.; Tsimelzon, A.; Wang, T.; Huffman, K.; Ludlow, A.; Ando, S.; et al. Erratum to: ESR1 mutations affect anti-proliferative responses to tamoxifen through enhanced cross-talk with IGF signaling. *Breast Cancer Res Treat* **2017**, *163*, 639-640, doi:10.1007/s10549-017-4250-4.
24. Giordano, C.; Cui, Y.; Barone, I.; Ando, S.; Mancini, M.A.; Berno, V.; Fuqua, S.A. Growth factor-induced resistance to tamoxifen is associated with a mutation of estrogen receptor alpha and its phosphorylation at serine 305. *Breast Cancer Res Treat* **2010**, *119*, 71-85, doi:10.1007/s10549-009-0334-0.
25. Gates, L.A.; Gu, G.; Chen, Y.; Rohira, A.D.; Lei, J.T.; Hamilton, R.A.; Yu, Y.; Lonard, D.M.; Wang, J.; Wang, S.P.; et al. Proteomic profiling identifies key coactivators

- utilized by mutant ERalpha proteins as potential new therapeutic targets. *Oncogene* **2018**, *37*, 4581-4598, doi:10.1038/s41388-018-0284-2.
26. Toy, W.; Shen, Y.; Won, H.; Green, B.; Sakr, R.A.; Will, M.; Li, Z.; Gala, K.; Fanning, S.; King, T.A.; et al. ESR1 ligand-binding domain mutations in hormone-resistant breast cancer. *Nat Genet* **2013**, *45*, 1439-1445, doi:10.1038/ng.2822.
27. Li, Z.; Levine, K.M.; Bahreini, A.; Wang, P.; Chu, D.; Park, B.H.; Oesterreich, S.; Lee, A.V. Upregulation of IRS1 Enhances IGF1 Response in Y537S and D538G ESR1 Mutant Breast Cancer Cells. *Endocrinology* **2018**, *159*, 285-296, doi:10.1210/en.2017-00693.
28. O'Leary, B.; Cutts, R.J.; Liu, Y.; Hrebien, S.; Huang, X.; Fenwick, K.; Andre, F.; Loibl, S.; Loi, S.; Garcia-Murillas, I.; et al. The Genetic Landscape and Clonal Evolution of Breast Cancer Resistance to Palbociclib plus Fulvestrant in the PALOMA-3 Trial. *Cancer Discov* **2018**, *8*, 1390-1403, doi:10.1158/2159-8290.CD-18-0264.
29. Kalluri, R. The biology and function of fibroblasts in cancer. *Nat Rev Cancer* **2016**, *16*, 582-598, doi:10.1038/nrc.2016.73.
30. Ohlund, D.; Elyada, E.; Tuveson, D. Fibroblast heterogeneity in the cancer wound. *J Exp Med* **2014**, *211*, 1503-1523, doi:10.1084/jem.20140692.
31. Sahai, E.; Astsaturov, I.; Cukierman, E.; DeNardo, D.G.; Egeblad, M.; Evans, R.M.; Fearon, D.; Greten, F.R.; Hingorani, S.R.; Hunter, T.; et al. A framework for advancing our understanding of cancer-associated fibroblasts. *Nat Rev Cancer* **2020**, *20*, 174-186, doi:10.1038/s41568-019-0238-1.
32. Bartoschek, M.; Oskolkov, N.; Bocci, M.; Lovrot, J.; Larsson, C.; Sommarin, M.; Madsen, C.D.; Lindgren, D.; Pekar, G.; Karlsson, G.; et al. Spatially and functionally distinct subclasses of breast cancer-associated fibroblasts revealed by single cell RNA sequencing. *Nat Commun* **2018**, *9*, 5150, doi:10.1038/s41467-018-07582-3.
33. Bernard, V.; Semaan, A.; Huang, J.; San Lucas, F.A.; Mulu, F.C.; Stephens, B.M.; Guerrero, P.A.; Huang, Y.; Zhao, J.; Kamyabi, N.; et al. Single-Cell Transcriptomics of Pancreatic Cancer Precursors Demonstrates Epithelial and Microenvironmental Heterogeneity as an Early Event in Neoplastic Progression. *Clin Cancer Res* **2019**, *25*, 2194-2205, doi:10.1158/1078-0432.CCR-18-1955.
34. Friedman, G.; Levi-Galibov, O.; David, E.; Bornstein, C.; Giladi, A.; Dadiani, M.; Mayo, A.; Halperin, C.; Pevsner-Fischer, M.; Lavon, H.; et al. Cancer-associated

- fibroblast compositions change with breast cancer progression linking the ratio of S100A4(+) and PDPN(+) CAFs to clinical outcome. *Nat Cancer* **2020**, *1*, 692-708, doi:10.1038/s43018-020-0082-y.
35. Li, H.; Courtois, E.T.; Sengupta, D.; Tan, Y.; Chen, K.H.; Goh, J.J.L.; Kong, S.L.; Chua, C.; Hon, L.K.; Tan, W.S.; et al. Reference component analysis of single-cell transcriptomes elucidates cellular heterogeneity in human colorectal tumors. *Nat Genet* **2017**, *49*, 708-718, doi:10.1038/ng.3818.
  36. Puram, S.V.; Tirosh, I.; Parikh, A.S.; Patel, A.P.; Yizhak, K.; Gillespie, S.; Rodman, C.; Luo, C.L.; Mroz, E.A.; Emerick, K.S.; et al. Single-Cell Transcriptomic Analysis of Primary and Metastatic Tumor Ecosystems in Head and Neck Cancer. *Cell* **2017**, *171*, 1611-1624 e1624, doi:10.1016/j.cell.2017.10.044.
  37. Costa, A.; Kieffer, Y.; Scholer-Dahirel, A.; Pelon, F.; Bourachot, B.; Cardon, M.; Sirven, P.; Magagna, I.; Fuhrmann, L.; Bernard, C.; et al. Fibroblast Heterogeneity and Immunosuppressive Environment in Human Breast Cancer. *Cancer Cell* **2018**, *33*, 463-479 e410, doi:10.1016/j.ccell.2018.01.011.
  38. Cortot, A.B.; Repellin, C.E.; Shimamura, T.; Capelletti, M.; Zejnullahu, K.; Ercan, D.; Christensen, J.G.; Wong, K.K.; Gray, N.S.; Janne, P.A. Resistance to irreversible EGF receptor tyrosine kinase inhibitors through a multistep mechanism involving the IGF1R pathway. *Cancer Res* **2013**, *73*, 834-843, doi:10.1158/0008-5472.CAN-12-2066.
  39. Orimo, A.; Gupta, P.B.; Sgroi, D.C.; Arenzana-Seisdedos, F.; Delaunay, T.; Naeem, R.; Carey, V.J.; Richardson, A.L.; Weinberg, R.A. Stromal fibroblasts present in invasive human breast carcinomas promote tumor growth and angiogenesis through elevated SDF-1/CXCL12 secretion. *Cell* **2005**, *121*, 335-348, doi:10.1016/j.cell.2005.02.034.
  40. Fridlender, Z.G.; Sun, J.; Kim, S.; Kapoor, V.; Cheng, G.; Ling, L.; Worthen, G.S.; Albelda, S.M. Polarization of tumor-associated neutrophil phenotype by TGF-beta: "N1" versus "N2" TAN. *Cancer Cell* **2009**, *16*, 183-194, doi:10.1016/j.ccr.2009.06.017.
  41. Mariathasan, S.; Turley, S.J.; Nickles, D.; Castiglioni, A.; Yuen, K.; Wang, Y.; Kadel, E.E., III; Koeppen, H.; Astarita, J.L.; Cubas, R.; et al. TGFbeta attenuates tumour response to PD-L1 blockade by contributing to exclusion of T cells. *Nature* **2018**, *554*, 544-548, doi:10.1038/nature25501.

42. Thomas, D.A.; Massague, J. TGF-beta directly targets cytotoxic T cell functions during tumor evasion of immune surveillance. *Cancer Cell* **2005**, *8*, 369-380, doi:10.1016/j.ccr.2005.10.012.
43. Pontiggia, O.; Sampayo, R.; Raffo, D.; Motter, A.; Xu, R.; Bissell, M.J.; Joffe, E.B.; Simian, M. The tumor microenvironment modulates tamoxifen resistance in breast cancer: a role for soluble stromal factors and fibronectin through beta1 integrin. *Breast Cancer Res Treat* **2012**, *133*, 459-471, doi:10.1007/s10549-011-1766-x.
44. Martinez-Outschoorn, U.E.; Goldberg, A.; Lin, Z.; Ko, Y.H.; Flomenberg, N.; Wang, C.; Pavlides, S.; Pestell, R.G.; Howell, A.; Sotgia, F.; et al. Anti-estrogen resistance in breast cancer is induced by the tumor microenvironment and can be overcome by inhibiting mitochondrial function in epithelial cancer cells. *Cancer Biol Ther* **2011**, *12*, 924-938, doi:10.4161/cbt.12.10.17780.
45. Chen, Y.; McAndrews, K.M.; Kalluri, R. Clinical and therapeutic relevance of cancer-associated fibroblasts. *Nat Rev Clin Oncol* **2021**, *18*, 792-804, doi:10.1038/s41571-021-00546-5.
46. Zhao, X.; Qu, J.; Sun, Y.; Wang, J.; Liu, X.; Wang, F.; Zhang, H.; Wang, W.; Ma, X.; Gao, X.; et al. Prognostic significance of tumor-associated macrophages in breast cancer: a meta-analysis of the literature. *Oncotarget* **2017**, *8*, 30576-30586, doi:10.18632/oncotarget.15736.
47. Mantovani, A.; Allavena, P.; Marchesi, F.; Garlanda, C. Macrophages as tools and targets in cancer therapy. *Nat Rev Drug Discov* **2022**, *21*, 799-820, doi:10.1038/s41573-022-00520-5.
48. Qiu, S.Q.; Waaijer, S.J.H.; Zwager, M.C.; de Vries, E.G.E.; van der Vegt, B.; Schroder, C.P. Tumor-associated macrophages in breast cancer: Innocent bystander or important player? *Cancer Treat Rev* **2018**, *70*, 178-189, doi:10.1016/j.ctrv.2018.08.010.
49. Azizi, E.; Carr, A.J.; Plitas, G.; Cornish, A.E.; Konopacki, C.; Prabhakaran, S.; Nainys, J.; Wu, K.; Kisieliovas, V.; Setty, M.; et al. Single-Cell Map of Diverse Immune Phenotypes in the Breast Tumor Microenvironment. *Cell* **2018**, *174*, 1293-1308 e1236, doi:10.1016/j.cell.2018.05.060.
50. Leek, R.D.; Hunt, N.C.; Landers, R.J.; Lewis, C.E.; Royds, J.A.; Harris, A.L. Macrophage infiltration is associated with VEGF and EGFR expression in breast

- cancer. *J Pathol* **2000**, *190*, 430-436, doi:10.1002/(SICI)1096-9896(200003)190:4<430::AID-PATH538>3.0.CO;2-6.
51. Castellaro, A.M.; Rodriguez-Baili, M.C.; Di Tada, C.E.; Gil, G.A. Tumor-Associated Macrophages Induce Endocrine Therapy Resistance in ER+ Breast Cancer Cells. *Cancers (Basel)* **2019**, *11*, doi:10.3390/cancers11020189.
  52. Li, D.; Ji, H.; Niu, X.; Yin, L.; Wang, Y.; Gu, Y.; Wang, J.; Zhou, X.; Zhang, H.; Zhang, Q. Tumor-associated macrophages secrete CC-chemokine ligand 2 and induce tamoxifen resistance by activating PI3K/Akt/mTOR in breast cancer. *Cancer Sci* **2020**, *111*, 47-58, doi:10.1111/cas.14230.
  53. Cozzo, A.J.; Fuller, A.M.; Makowski, L. Contribution of Adipose Tissue to Development of Cancer. *Compr Physiol* **2017**, *8*, 237-282, doi:10.1002/cphy.c170008.
  54. Zhang, Z.; Scherer, P.E. Adipose tissue: The dysfunctional adipocyte - a cancer cell's best friend. *Nat Rev Endocrinol* **2018**, *14*, 132-134, doi:10.1038/nrendo.2017.174.
  55. Sheng, X.; Parmentier, J.H.; Tucci, J.; Pei, H.; Cortez-Toledo, O.; Dieli-Conwright, C.M.; Oberley, M.J.; Neely, M.; Orgel, E.; Louie, S.G.; et al. Adipocytes Sequester and Metabolize the Chemotherapeutic Daunorubicin. *Mol Cancer Res* **2017**, *15*, 1704-1713, doi:10.1158/1541-7786.MCR-17-0338.
  56. Sun, X.; Casbas-Hernandez, P.; Bigelow, C.; Makowski, L.; Joseph Jerry, D.; Smith Schneider, S.; Troester, M.A. Normal breast tissue of obese women is enriched for macrophage markers and macrophage-associated gene expression. *Breast Cancer Res Treat* **2012**, *131*, 1003-1012, doi:10.1007/s10549-011-1789-3.
  57. Barone, I.; Caruso, A.; Gelsomino, L.; Giordano, C.; Bonofiglio, D.; Catalano, S.; Ando, S. Obesity and endocrine therapy resistance in breast cancer: Mechanistic insights and perspectives. *Obes Rev* **2022**, *23*, e13358, doi:10.1111/obr.13358.
  58. Gershuni, V.; Li, Y.R.; Williams, A.D.; So, A.; Steel, L.; Carrigan, E.; Tchou, J. Breast cancer subtype distribution is different in normal weight, overweight, and obese women. *Breast Cancer Res Treat* **2017**, *163*, 375-381, doi:10.1007/s10549-017-4192-x.
  59. Ando, S.; Gelsomino, L.; Panza, S.; Giordano, C.; Bonofiglio, D.; Barone, I.; Catalano, S. Obesity, Leptin and Breast Cancer: Epidemiological Evidence and Proposed Mechanisms. *Cancers (Basel)* **2019**, *11*, doi:10.3390/cancers11010062.

60. Barone, I.; Giordano, C.; Bonofiglio, D.; Ando, S.; Catalano, S. The weight of obesity in breast cancer progression and metastasis: Clinical and molecular perspectives. *Semin Cancer Biol* **2020**, *60*, 274-284, doi:10.1016/j.semcancer.2019.09.001.
61. Alarcon Rojas, C.A.; Alvarez-Banuelos, M.T.; Morales-Romero, J.; Suarez-Diaz, H.; Hernandez-Fonseca, J.C.; Contreras-Alarcon, G. Breast Cancer: Metastasis, Molecular Subtypes, and Overweight and Obesity in Veracruz, Mexico. *Clin Breast Cancer* **2019**, *19*, e166-e171, doi:10.1016/j.clbc.2018.08.003.
62. Blair, C.K.; Wiggins, C.L.; Nibbe, A.M.; Storlie, C.B.; Prossnitz, E.R.; Royce, M.; Lomo, L.C.; Hill, D.A. Obesity and survival among a cohort of breast cancer patients is partially mediated by tumor characteristics. *NPJ Breast Cancer* **2019**, *5*, 33, doi:10.1038/s41523-019-0128-4.
63. Copson, E.R.; Cutress, R.I.; Maishman, T.; Eccles, B.K.; Gerty, S.; Stanton, L.; Altman, D.G.; Durcan, L.; Wong, C.; Simmonds, P.D.; et al. Obesity and the outcome of young breast cancer patients in the UK: the POSH study. *Ann Oncol* **2015**, *26*, 101-112, doi:10.1093/annonc/mdu509.
64. Majed, B.; Senouci, K.; Asselain, B. Shortened survival and more metastasis recurrences among overweight breast cancer patients. *Breast J* **2009**, *15*, 557-559, doi:10.1111/j.1524-4741.2009.00785.x.
65. Osman, M.A.; Hennessy, B.T. Obesity Correlation With Metastases Development and Response to First-Line Metastatic Chemotherapy in Breast Cancer. *Clin Med Insights Oncol* **2015**, *9*, 105-112, doi:10.4137/CMO.S32812.
66. Chan, D.S.M.; Vieira, A.R.; Aune, D.; Bandera, E.V.; Greenwood, D.C.; McTiernan, A.; Navarro Rosenblatt, D.; Thune, I.; Vieira, R.; Norat, T. Body mass index and survival in women with breast cancer-systematic literature review and meta-analysis of 82 follow-up studies. *Ann Oncol* **2014**, *25*, 1901-1914, doi:10.1093/annonc/mdu042.
67. Jiralerspong, S.; Goodwin, P.J. Obesity and Breast Cancer Prognosis: Evidence, Challenges, and Opportunities. *J Clin Oncol* **2016**, *34*, 4203-4216, doi:10.1200/JCO.2016.68.4480.
68. Protani, M.; Coory, M.; Martin, J.H. Effect of obesity on survival of women with breast cancer: systematic review and meta-analysis. *Breast Cancer Res Treat* **2010**, *123*, 627-635, doi:10.1007/s10549-010-0990-0.

69. Ewertz, M.; Jensen, M.B.; Gunnarsdottir, K.A.; Hojris, I.; Jakobsen, E.H.; Nielsen, D.; Stenbygaard, L.E.; Tange, U.B.; Cold, S. Effect of obesity on prognosis after early-stage breast cancer. *J Clin Oncol* **2011**, *29*, 25-31, doi:10.1200/JCO.2010.29.7614.
70. Wisse, A.; Tryggvadottir, H.; Simonsson, M.; Isaksson, K.; Rose, C.; Ingvar, C.; Jernstrom, H. Increasing preoperative body size in breast cancer patients between 2002 and 2016: implications for prognosis. *Cancer Causes Control* **2018**, *29*, 643-656, doi:10.1007/s10552-018-1042-z.
71. Pellegrino, M.; Rizza, P.; Dona, A.; Nigro, A.; Ricci, E.; Fiorillo, M.; Perrotta, I.; Lanzino, M.; Giordano, C.; Bonofiglio, D.; et al. FoxO3a as a Positive Prognostic Marker and a Therapeutic Target in Tamoxifen-Resistant Breast Cancer. *Cancers (Basel)* **2019**, *11*, doi:10.3390/cancers11121858.
72. Rovito, D.; Gionfriddo, G.; Barone, I.; Giordano, C.; Grande, F.; De Amicis, F.; Lanzino, M.; Catalano, S.; Ando, S.; Bonofiglio, D. Ligand-activated PPARgamma downregulates CXCR4 gene expression through a novel identified PPAR response element and inhibits breast cancer progression. *Oncotarget* **2016**, *7*, 65109-65124, doi:10.18632/oncotarget.11371.
73. Gu, G.; Tian, L.; Herzog, S.K.; Rechoum, Y.; Gelsomino, L.; Gao, M.; Du, L.; Kim, J.A.; Dustin, D.; Lo, H.C.; et al. Hormonal modulation of ESR1 mutant metastasis. *Oncogene* **2021**, *40*, 997-1011, doi:10.1038/s41388-020-01563-x.
74. Giordano, C.; Gelsomino, L.; Barone, I.; Panza, S.; Augimeri, G.; Bonofiglio, D.; Rovito, D.; Naimo, G.D.; Leggio, A.; Catalano, S.; et al. Leptin Modulates Exosome Biogenesis in Breast Cancer Cells: An Additional Mechanism in Cell-to-Cell Communication. *J Clin Med* **2019**, *8*, doi:10.3390/jcm8071027.
75. Gionfriddo, G.; Plastina, P.; Augimeri, G.; Catalano, S.; Giordano, C.; Barone, I.; Morelli, C.; Giordano, F.; Gelsomino, L.; Sisci, D.; et al. Modulating Tumor-Associated Macrophage Polarization by Synthetic and Natural PPARgamma Ligands as a Potential Target in Breast Cancer. *Cells* **2020**, *9*, doi:10.3390/cells9010174.
76. Vantaggiato, L.; Shaba, E.; Carleo, A.; Bezzini, D.; Pannuzzo, G.; Luddi, A.; Piomboni, P.; Bini, L.; Bianchi, L. Neurodegenerative Disorder Risk in Krabbe Disease Carriers. *Int J Mol Sci* **2022**, *23*, doi:10.3390/ijms232113537.
77. Bianchi, L.; Altera, A.; Barone, V.; Bonente, D.; Bacci, T.; De Benedetto, E.; Bini, L.; Tosi, G.M.; Galvagni, F.; Bertelli, E. Untangling the Extracellular Matrix of Idiopathic

- Epiretinal Membrane: A Path Winding among Structure, Interactomics and Translational Medicine. *Cells* **2022**, *11*, doi:10.3390/cells11162531.
78. Bianchi, L.; Carnemolla, C.; Viviani, V.; Landi, C.; Pavone, V.; Luddi, A.; Piomboni, P.; Bini, L. Soluble protein fraction of human seminal plasma. *J Proteomics* **2018**, *174*, 85-100, doi:10.1016/j.jprot.2017.12.015.
79. Gagliardi, A.; Besio, R.; Carnemolla, C.; Landi, C.; Armini, A.; Aglan, M.; Otaify, G.; Temtamy, S.A.; Forlino, A.; Bini, L.; et al. Cytoskeleton and nuclear lamina affection in recessive osteogenesis imperfecta: A functional proteomics perspective. *J Proteomics* **2017**, *167*, 46-59, doi:10.1016/j.jprot.2017.08.007.
80. Lanczky, A.; Gyorffy, B. Web-Based Survival Analysis Tool Tailored for Medical Research (KMplot): Development and Implementation. *J Med Internet Res* **2021**, *23*, e27633, doi:10.2196/27633.
81. Liao, Y.; Smyth, G.K.; Shi, W. featureCounts: an efficient general purpose program for assigning sequence reads to genomic features. *Bioinformatics* **2014**, *30*, 923-930, doi:10.1093/bioinformatics/btt656.
82. Love, M.I.; Huber, W.; Anders, S. Moderated estimation of fold change and dispersion for RNA-seq data with DESeq2. *Genome Biol* **2014**, *15*, 550, doi:10.1186/s13059-014-0550-8.
83. Chen, Y.; Ning, J.; Cao, W.; Wang, S.; Du, T.; Jiang, J.; Feng, X.; Zhang, B. Research Progress of TXNIP as a Tumor Suppressor Gene Participating in the Metabolic Reprogramming and Oxidative Stress of Cancer Cells in Various Cancers. *Front Oncol* **2020**, *10*, 568574, doi:10.3389/fonc.2020.568574.
84. Kaimul, A.M.; Nakamura, H.; Masutani, H.; Yodoi, J. Thioredoxin and thioredoxin-binding protein-2 in cancer and metabolic syndrome. *Free Radic Biol Med* **2007**, *43*, 861-868, doi:10.1016/j.freeradbiomed.2007.05.032.
85. Lerner, A.G.; Upton, J.P.; Praveen, P.V.; Ghosh, R.; Nakagawa, Y.; Igarria, A.; Shen, S.; Nguyen, V.; Backes, B.J.; Heiman, M.; et al. IRE1alpha induces thioredoxin-interacting protein to activate the NLRP3 inflammasome and promote programmed cell death under irremediable ER stress. *Cell Metab* **2012**, *16*, 250-264, doi:10.1016/j.cmet.2012.07.007.
86. Osowski, C.M.; Hara, T.; O'Sullivan-Murphy, B.; Kanekura, K.; Lu, S.; Hara, M.; Ishigaki, S.; Zhu, L.J.; Hayashi, E.; Hui, S.T.; et al. Thioredoxin-interacting protein

- mediates ER stress-induced beta cell death through initiation of the inflammasome. *Cell Metab* **2012**, *16*, 265-273, doi:10.1016/j.cmet.2012.07.005.
87. Nagaraj, K.; Lapkina-Gendler, L.; Sarfstein, R.; Gurwitz, D.; Pasmanik-Chor, M.; Laron, Z.; Yakar, S.; Werner, H. Identification of thioredoxin-interacting protein (TXNIP) as a downstream target for IGF1 action. *Proc Natl Acad Sci U S A* **2018**, *115*, 1045-1050, doi:10.1073/pnas.1715930115.